2D MATERIALS AND THEIR HETERO BILAYER SYSTEMS FOR OPTOELECTRONIC APPLICATIONS

Master of Science Thesis

Yahaya SHEHU

Eskişehir 2019

2D MATERIALS AND THEIR HETERO BILAYER SYSTEMS FOR OPTOELECTRONIC APPLICATIONS

Yahaya SHEHU

MATER OF SCIENCE THESIS

Electronics Engineering/Department of Electrical Electronics Engineering

Supervisor: Assoc. Prof. Dr. Nihan KOSKU PERKGÖZ

Eskişehir

Anadolu University

Graduate School of Science

December 2019

FINAL APPROVAL FOR THESIS

This thesis titled "**2D Materials and Their Hetero Bilayer Systems for Optoelectronic Applications**" has been prepared and submitted by Yahaya SHEHU in partial fulfillment of the requirements in "Anadolu University Directive on Graduate Education and Examination" for the Degree of Master of Science in Electrical and Electronics Engineering Department and has been examined and approved on 27/12/2019.

	Committee Members	**Signature**
Member (Supervisor)	: Assoc. Prof. Dr. Nihan KOSKU PERKGÖZ	……..……
Member	: Prof. Dr. Feridun AY	.....
Member	: Assoc. Prof. Dr. Faruk DİRİSAĞLIK	.....

.....

Director,
Graduate School of Science

ÖZET

OPTOELEKTRONIK UYDULAMALAR IÇIN 2B MALZEMELER VE BUNLARIN HETERO 2-KATMANLI SYSTEMLERI

Yahaya SHEHU
Elektrik ve Elektronik Mühendisliği Anabilim Dalı
Elektronik Bilim Dalı

Anadolu Üniversitesi, Fen Bilimler Enstitüsü, Aralık, 2019
Danışman: Doç. Dr. Nıhan KOSKU PEKGÖZ

Gelecekteki optoelektronik uygulamalarında meydana gelebilecek değişimlerle uyumlu malzeme sistemleri çalışmalar devam ederken, bu konuda iki boyutlu malzemelerin potansiyelini araştırmak için büyük çaba harcanmaktadır. Bu sebeple, bu tezde iki boyutlu geçiş metali dikalgonitleri ve bunların hetero yapılı çift katmanlı sistemlerinin optoelektronik uygulamalar için kapsamlı bir çalışması sunulmaktadır. Bu çalışma için tek katmanlı MoS_2 ve $MoSe_2$ materyalleri, dikalgonitler Kükürt ve Selenyum olarak değişirken geçiş metali Molibden aynı tutulmuştur. Böylece, yapısal ve optik karakterizasyonları sayesinde, etkileşimlerini inceleyebiliriz. Tek katmanlı MoS_2 ve $MoSe_2$ sırasıyla ~ 1.82 eV ve ~ 1.55 eV doğrusal bant aralıklarına sahiptir. Tek katmanlı MoS_2, hem SiO_2/Si alttaşlar üzerinde ALD yöntemi destekli CVD yöntemi hem de cam bir alttaş üzerinde geleneksel CVD yöntemi kullanılarak büyütülebilir. $MoSe_2$ içinse, CVD sisteminde kullanılan NaCl çözeltisi ile kaplanmış SiO_2/Si alttaşlar tercih edilebilir. Büyüme parametreleri optimize edilirken ürünün yüksek oranda alttaş yüzeyini kaplaması, yüksek kaliteli olması koşullarına dikkat edilmiştir. $MoS_2/MoSe_2$ iki tabakalı heteroyapı sistemi Polimetil Metakrilat (PMMA) destekli ıslak transfer yöntemi kullanılarak transfer edilir. Transfer edilen tek katmanlı geçiş metali dikalgonitleri ve bunların iki tabakalı heteroyapıları sistematik olarak Raman, Fotolüminesans ve Atomik Kuvvet Mikroskobu spektroskopileri kullanılarak karakterize edilir. Ayrıca iki katmanlı bu heteroyapı sıcaklığın 83-483 Kelvin sıcaklık değerleri arasında değiştilerek, sıcaklığa bağlı mikro Raman spektroskopisi ile karakterize edilir. Burada malzemelerin her birindeki sıcaklığa göre Raman modunun pik pozisyonundaki değişim ve maksimum yarısı tam genişlik (MYTG) analiz edilmiştir. Sıcaklık artışı bizim MoS_2 ve $MoSe_2$ Raman modlarının karakteristik yumuşamasını gözlemlememizi sağladı. Malzemelerin sıcaklık katsayısı, iki katmanlı heteroyapılarda izole bölgeye göre daha büyüktür.

Anahtar Sözcükler: 2B malzemeler, MoS_2, $MoSe_2$, ALD, CVD, Optoelektronic

ABSTRACT

2D MATERIALS AND THEIR HETERO BILAYER SYSTEMS FOR OPTOELECTRONIC APPLICATIONS

Yahaya SHEHU

Department of Electrical and Electronics Engineering

Programme in Electronics Engineering

Anadolu University, Graduate School of Science, December 2019

Supervisor: Assoc. Prof. Dr. Nihan KOSKU PERKGÖZ

In the pursuit of the materials systems compatible with the paradigm shift in the future optoelectronics, immense effort is devoted to exploring the potential of 2D materials. Motivated by this, a comprehensive study of 2D TMD and their hetero bilayer systems for optoelectronic applications is presented in this thesis. Monolayer MoS_2 and $MoSe_2$ have been chosen by keeping the transition metal (Mo) the same while changing the dichalcogenides from S to Se, so we could investigate their interaction by structural and optical characterizations. Single layer MoS_2 and $MoSe_2$ have direct bandgaps of ~ 1.82 eV and ~ 1.55 eV, respectively. Monolayer MoS_2 is grown both by using the ALD-assisted CVD method on SiO_2/Si substrates and conventional CVD method on glass substrates. For $MoSe_2$, SiO_2/Si substrates coated with NaCl solution as are used in the conventional CVD system. The growth parameters are carefully optimized for high coverage of high-quality and large area monolayers. Subsequently, $MoS_2/MoSe_2$ hetero bilayer system is formed by PMMA-assisted wet transfer method. The Monolayer TMDs and their hetero bilayer system are systematically characterized by Raman, PL, and AFM spectroscopies. The hetero bilayer system is further characterized by temperature dependent μRaman spectroscopy by varying the temperature between 83 K and 483K. Change in the Raman mode's peak position and FWHM with respect to temperature in each of the materials has been analyzed. We observed characteristic softening of the MoS_2 and $MoSe_2$ Raman modes with an increase in temperature, and the temperature coefficient of the materials is larger in the hetero bilayer system than in the isolated region.

Keywords: 2D materials, TMD, MoO_3, MoS_2, $MoSe_2$, ALD, CVD, Optoelectronic

ACKNOWLEDGEMENT

All thanks be to Almighty God for sparing my life. My sincere gratitude goes to my supervisor, Assoc. Prof. Dr. Nihan Kosku PERKGÖZ for her profound support both academic and otherwise. I also express my gratitude to Prof. Dr. Feridun AY for his immense contributions to my studies. My acknowledgment goes to the Turkiye Burslari (YTB) for funding my M.Sc. education. I thank the entire MIDAS research group members for their kind support during my studies. I especially want to acknowledge Mustafa DEMİRTAŞ, Hussayin ŞAR, Merve OPER, and Mehmet BAY for their support during my laboratory experiments. I also want to acknowledge the Carbon-based Materials Research Group of under the leadership of *Assoc. Prof. Dr. Yasemin ÇELIK* for letting me use some of their laboratory facilities in the course of my studies. I thank every individual and body that contributed directly or indirectly to the successful completion of my M.Sc. study.

Yahaya SHEHU

December 2019

27/12/2019

STATEMENT OF COMPLIANCE WITH ETHICAL PRINCIPLES AND RULES

I hereby truthfully declare that this thesis is an original work prepared by me; that I have behaved in accordance with the scientific ethical principles and rules throughout the stages of preparation, data collection, analysis and presentation of my work; that I have cited the sources of all the data and information that could be obtained within the scope of this study, and included these sources in the references section; and that this study has been scanned for plagiarism with "scientific plagiarism detection program" used by Anadolu University, and that "it does not have any plagiarism" whatsoever. I also declare that, if a case contrary to my declaration is detected in my work at any time, I hereby express my consent to all the ethical and legal consequences that are involved.

.....

Yahaya SHEHU

TABLE OF CONTENTS

LIST OF FIGURES

LIST OF TABLES

INDEX OF ABBREVIATIONS AND SYMBOLS

0D	: Zero dimensional
1D	: One dimensional
2D	: Two dimensional
3D	: Three dimensional
AFM	: Atomic force microscopy/microscope
ALD	: Atomic layer deposition
APD	: Avalanche photodiode
ATR	: Attenuated total reflection
CBM	: Conduction band minimum
CCD	: Charge couple device
CNT	: Carbon nanotube
CVD	: Chemical vapor deposition
CVT	: Chemical vapor transport
DI	: De-ionized
EBL	: Electron beam lithography
EBR	: Edge bread removal
EHP	: Electron hole pair
E-k	: Energy - wavenumber
ELR	: Extrapolation in the linear region
EQE	: External quantum efficiency
FET	: Field effect transistor
FTIRS	: Fourier transform infrared spectroscopy/spectroscope
GPC	: Growth per cycle
HER	: Hydrogen evolution reduction
HF	: High force
IC	: Integrated circuit
IQE	: Internal quantum efficiency
I-V	: Current-voltage
Laser	: Light amplification by stimulated emission of radiation
LED	: Light emission diode
LF	: Low force

MBE : Molecular beam epitaxy
MFC : Mass flow controller
MSE : Mean square error
NA : Numerical aperture
NIR : Near infrared
NOE : Nonlinear optical element
ORAM : Optical random access memory
PEALD : Plasma Enhanced ALD
PL : Photoluminescence
PPM : Parts per million
PV : Photovoltaic
PVD : Physical vapor deposition
QCM : Quartz crystal microbalance
QW : Quantum well
rpm : rotation per minute
SCCM : Standard cubic centimeter per minute
SCTD : Surface charge transfer doping
SE : Spectroscopic ellipsometry/ellipsometer
SEM : Scanning electron microscopy/microscope
SESAM : Semiconductor saturable absorber mirror
SMU : Simple measure unit
SWCNT : Single-walled carbon nanotube
TEM : Transmission electron microscopy/microscope
TI : Topological insulator
TMD : Transition metal dichalcogenides
TVD : Thermal vapor deposition
TVS : Thermal vapor sulfurization
VASE : Variable Angle Spectroscopic ellipsometry/ellipsometer
VBM : Valence band maximum
vdW : van der Waals
λ : Wavelength
α : Absorption coefficient

ω	: Photon vibrational frequency
χ	: Temperature coefficient
∂	: Partial differential
γ	: Volume of thermal coefficient
Γ	: Background contribution

1. INTRODUCTION

1.1 Introduction

Optoelectronic devices are among the essential components of modern-day technology. Millions of optoelectronic devices have been produced since the first discovery of laser in the early 1960s. The use of these devices pervades our daily lives in lighting, medicine, computing, entertainment, communications, security, transportation, to mention but a few. Perhaps, the greatest impact of the optoelectronic devices on humankind is their application in optical fiber communication which enable inexpensive and high-quality data and voice transmission across the globe. In contrast to the majority of electronic devices which are made using silicon, optoelectronic devices are predominantly based on III-IV semiconductor materials such as GaSb, GaAs, InP, GaN and their alloys [1, 2]. These materials are strategically prioritized due to their direct band gap which gives them more favorable optoelectronic device performance. Despite their interesting properties and the remarkable achievements that using them brought about, III-IV semiconductors have some peculiar shortcomings which have been profiled by researchers across the world [3, 4]. In addition, the recent trend in device miniaturization necessitate the pursuit for new materials as alternatives to III-V semiconductor.

The consequence of this endeavor is the discovery of two dimensional (2D) materials. The success recorded in the isolation of a layer of graphite (called graphene) in 2004 marked the era of 2D materials [5]. High expectations from graphene increased after the observation of its high carrier mobility (100,000 $cm^2\ V^{-1}\ s^{-1}$) and have been considered as the successor of the current semiconductor materials. Even though Nobel prized, graphene did not meet the expectations in optoelectronic applications due its zero band gap. It nonetheless demonstrated promising performance when applied in heat sink, sensing, radio frequency (RF), plasmonic, energy storage, etc. [6-10] and also pioneered and inspired the research for other 2D materials.

A new momentum for 2D materials increased after the discovery of superior field-effect mobility of up to 200 $cm^{-1}V^{-1}S^{-1}$ and room temperature on/off ratio of up to 10^8 by Radisavljevic *et al.* [11] as well as the photoresponsivity reaching up to 7.5 mA/W by Yin *et al.* [12] for single layer MoS_2 as a member of transition metals dichalcogenides (TMDs). Since then, the family of 2D materials (that include insulators, metals, and semiconductors) have been expanding due to their novel physical phenomena unveiled

by the fist principle calculations and future applications [13, 14]. Interest in the 2D materials has witnessed an exponential growth in research output since 2011. The data obtained from the Web of Science shows that the number of publications per year on 2D material research have been increasing significantly (1325 publication/year in 2011 to 6114 publication/year in 2019) [15]. This massive increase in research productivity has revealed the possibility of stacking different layers of different 2D materials to form what is called "heterostructure" and as a result, novel optoelectronic devices that cannot be achieved otherwise are produced [14, 16, 17].

1.2 Motivation of the Study

In the nearest future, optoelectronic devices are anticipated to be wearable, transparent, flexible and ultrathin. As the industry is experiencing a paradigm shift, 2DTMDs (such as MoS_2, $MoSe_2$, WS_2, and WSe_2) have receive massive attention by researchers across the globe due to their interesting properties such as their direct band gap when confined to a single layer. More of this interest arose after discovering the functionality of 2D TMDs heterostructure and their possible novel optoelectronic applications. The application of 2D TMD heterostructures for optoelectronic devices is influenced mainly by factors that include (a) higher light absorption [18] (b) preservation of the direct band gap of the 2D TMDs in the heterostructure [19-21]. Consequently, 2D TMDs and their heterostructure have been considered promising candidates for future optoelectronic devices [14, 16]. To meet this fundamental goal, 2D TMDs need to be grown with high quality and in large area, so that commercial scale production of their optoelectronic devices can be possible. Also, since the heterostructure based on 2D TMDs is rather newly discovered, understanding the properties of the structure, such as its durability under extreme temperature condition, will be of great importance for the development of novel optoelectronic devices.

1.3 Scope and Objectives of the Study

In this studies, atomic layer deposition (ALD) method is used to grow MoO_3 films while chemical vapor deposition (CVD) methods are used to grow 2D MoS_2 and 2D $MoSe_2$. Characterization of the materials is carried out using μRaman, photoluminescence (PL), atomic force microscopy (AFM), spectroscopic ellipsometry (SE), and Fourier transform infrared spectroscopy (FTIR). The objectives of the study are centered around the following objectives:

1. To control the layer and size distribution of 2D MoS_2 by ALD-assisted CVD method
2. To grow high quality and large area MoS_2 and $MoSe_2$ on glass substrates by CVD method
3. To fabricate and characterize a high-quality $MoS_2/MoSe_2$ hetero bilayer system
4. To carryout temperature-dependent μRaman spectroscopy of the $MoS_2/MoSe_2$ hetero bilayer system, with the with the aim of characterizing its thermal properties under extreme temperature

1.4 Organization of the Study

To meet the objectives of this study, this report has been organized into seven chapters. In ***chapter 1***, the author introduces the chapter with the general perspectives of the use of 2D materials for optoelectronic applications and motivation of the study. The author presents further the scope and objectives of the study, organization of the study, and concludes with the challenges faced in the course of the study. In ***chapter 2***, the author presents a brief literature review about the thesis topic. In ***chapter 3***, the author presents the experimental methodologies and the parameters used in the study. In ***chapter 4***, the author presents layer and size distribution control of 2D MoS_2 by the ALD-assisted CVD method. The author splits this chapter into two subsections namely ALD growth and characterization of MoO_3 films and CVD growth of 2D MoS_2 using ALD grown MoO_3 films.

In ***chapter 5,*** the author presents the CVD growth and characterization of 2D MoS_2 and $MoSe_2$ by changing various parameters. In ***chapter 6,*** the author presents formation and various characterization of the $MoS_2/MoSe_2$ hetero bilayer. This chapter includes the temperature dependent μRaman spectroscopy of the hetero bilayer and comparative analysis of the result with that of the monolayer MoS_2 and $MoSe_2$. In ***chapter 7***, the author makes the concluding remarks drawn from each chapter and finalized the thesis with some recommendations for future work.

1.5 Challenges of the Study

In the course of the study, the author faces the following challenges:

1. *Uniform and large scale atomically thin TMDS:* TMD materials' growth by CVD or ALD can be very challenging. The use of suitable parameters to ensure uniform and large area growth is time consuming and requires lots of patience. The machines used

to grow TMDs stops functioning easily and even when they are fully functional the experiments can be unsuccessful due to some environmental factors.

2. *CVD Growth of $MoSe_2$:* Several experiments to grow 2D $MoSe_2$ on glass substrate were performed, however the results were a $MoSe_{(2-x)}S_{(x)}$ alloy due to sulfur contamination of the CVD system and or the sulfur compounds present in the glass substrate. With little success achieved using glass substrates, research attention was diverted to NaCl-assisted CVD growth of $MoSe_2$ on SiO_2/Si substrate.
3. *Formation of MoS_2/$MoSe_2$ HB:* formation of the HB was very challenging as well. The PMMA assisted wet transfer method adopted in this study required the separation of the MoS_2 flakes from the glass substrate by the DI water. The films were delicate and had to be handled painstakingly.
4. *Locating same flake for characterization:* It is required that the same flake on a sample be characterized by optical microscope, AFM, Raman, PL, etc. This can be very easy for say mechanically exfoliated flake where there is only one or a few flakes. In CVD methods thousands of the identical flakes are grown with a non-regular distribution. Locating one flake to be used for various characterization was very challenging.

2. LITERATURE REVIEW

2.1 Overview of 2D Materials

2.1.1 Introduction

Progress in science and technology has paved the way for humankind to developed techniques for manipulating matter, manufacturing of materials, and fabrication of devices on an atomic or molecular scale. These techniques are encompassed in a new discipline called "Nanotechnology". Nanotechnology is multi-disciplinary and is applied in Electronics to develop a new area called Nanoelectronics. Materials used in the Nanoelectronics are categorized by their dimension into three-dimensional (3D, bulk), two-dimensional (monolayer or single layer), one-dimensional (1D, nanowire), and zero-dimensional (0D, quantum dot) [22]. This categorization is based on the fact that properties of materials, such as electronic and optical, change as a function of their dimensionality [23]. In particular, quantum confinement is a dimension dependent phenomenon [24]. 2D materials are monolayer of their bulk having a thickness in the range of 0.3 nm and 10 nm [23, 25-31]. 2D materials possess superior properties over their bulk counterpart and have the potential of becoming the candidate materials for the future electronics and optoelectronics.

2.1.2 Brief history of 2D materials

The history of 2D materials can be traced back to more than a half century ago when Richard P. Feyman in his lecture titled "*There is Plenty of Room at the Bottom*" inspired the scientist of the generation especially when he asked the questions "What could we do with layered structures with just the right layers? What would the properties of materials be if we could really arrange the atoms the way we want them [32]? Since then, Frindt *et al.* was able to exfoliate few-layer MoS_2 by scotch tape method [33, 34] and interaction of Li ions between MoS_2 layers [35]. In the end, Novoselov, Geim and his colleagues demonstrated that it is possible to isolate a monolayer of a material from its bulk. In 2004, they exfoliated an sp^2-hybridized carbon sheet from graphite, later known as Graphene, using mechanical exfoliation by scotch tape method [5]. The following year, the same group reported the isolation of monolayer of other materials [36]. In 2010, Novoselov and Geim received a Nobel Award in Physics for their work.

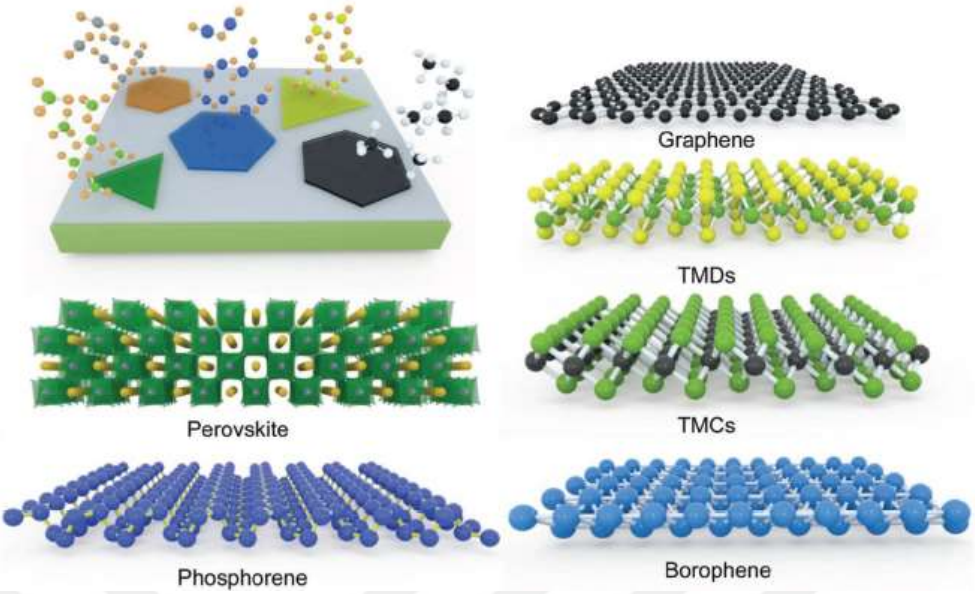

Figure 2.1. *Overview of layer structure of 2D materials (Geng et al., 2018)*

Thanks to Novoselov and Geim, scientists around the world have discovered nearly 2000 other materials that have strong in-plane and weak van der Waals out-of-plane bonds and can easily be exfoliated into monolayer [37]. Figure 2.2 shows the categorization of 2D materials into different families in accordance with materials' constituent elements and atomic/molecular shape pattern. As shown in the table, 2D materials exhibit different stability depending on the environmental conditions [13].

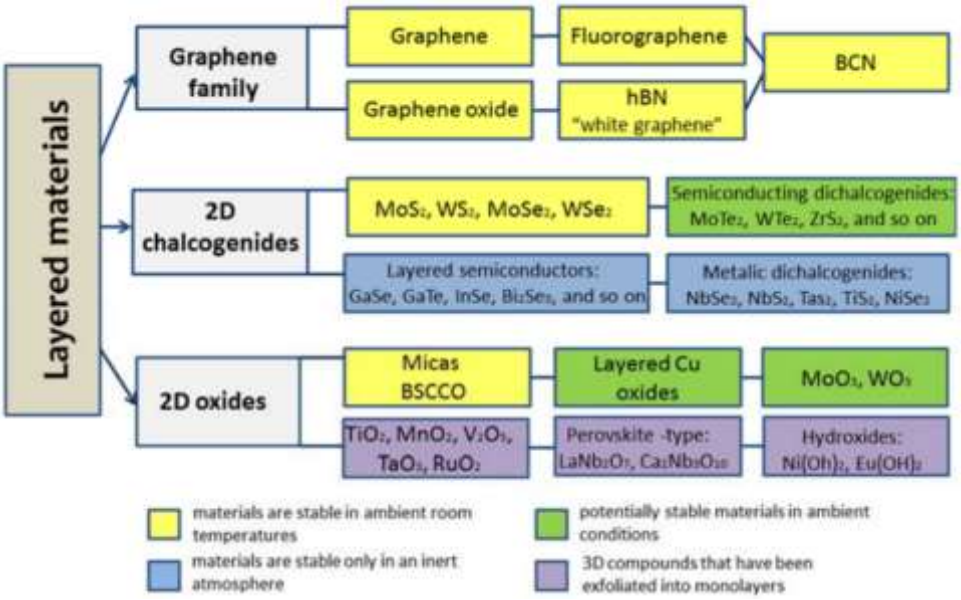

Figure 2.2. *Family of 2D materials that have been confirmed experimentally (Shavanova et al., 2016)*

2.2 Production Techniques of 2D Materials

2D materials production techniques are broadly categorized into two namely, top-bottom and bottom-top. Top-bottom approach involves the preparation of 2D materials from their bulk counterpart either mechanically or chemically. This approach includes methods such as liquid exfoliation and mechanical exfoliation. On the other hand, bottom-top approach encompasses the growth of 2D materials by reaction of the constituent element(s) of such materials. This approach includes several sophisticated methods such as CVD, ALD, and molecular beam epitaxy (MBE). In many of these techniques, 2D materials are grown in a reaction chamber, and the use of the appropriate parameters is critical for successful growth of the 2D material of interest. 2D materials produced by the top-bottom methods are of higher quality, yet the bottom-top methods is more scalable for commercial optoelectronic applications [38].

2.2.1 Mechanical exfoliation

This method involves the peeling of a monolayer of a material from its bulk counterpart. After the isolation of graphene from its bulk form using scotch tape [5], this method is later called mechanical exfoliation. Subsequently, Geim and Noveselov *et al.* later use this method to exfoliate other 2D materials such as MoS_2, $NbSe_2$, BN, and $Bi_2Sr_2CaCu_2O_x$ [5, 36, 39]. 2D materials produced by this method are of high quality. However, the flakes size produced by this method is in the order of 20 μm [38]. Even though this method is not scalable, it is commonly used to prepare flakes of 2D TMDs and study their properties [11, 12, 40, 41]. Other drawbacks of this method are the production of 2D materials flakes with some defects, random sizes and a number of layers [42, 43].

2.2.2 Liquid exfoliation

This method, also known as chemical exfoliation, is more scalable than the mechanical exfoliation method. In this method, 2D materials are produced by spreading the powder of a bulk material on water and applying physical force such as ultrasonication. A solution processing step is then applied to obtain flakes of 2D materials. To increase the yield of monolayer flakes, the use of a proper solution with high surface energy is critical to break the van der Waals forces between the crystal layers. Another method used to break the van der Waals force is by including lithium ion in the solution to intercalate the layers of a crystal material [44]. This method is mostly used to

prepare samples of 2D MoS_2 for use as cathodes in a setup of electrochemical exfoliation [35, 45, 46]. Liquid exfoliation is more promising for 2D materials sample preparation for flexible optoelectronics.

2.2.3 Chemical vapor deposition (CVD)

This is one of the bottom-top approaches to grow 2D materials. In CVD, 2D materials are grown by the reaction of the vapor phase of the material's constituent(s) which can be solid or gaseous precursors. It can be commented that CVD overcomes the limitations and drawbacks of the top-down approaches to the production of 2D materials by providing repeatable production of large area and low cost 2D materials. Details about 2D materials growth methods by CVD are presented in the relevant sections of this report. Flake size, distribution, and morphology of 2D materials grown by CVD depend on several parameters such as the pressure, carrier gas flow, temperature, precursor ratio, substrate, and use of coregents [16, 30]. These parameters affect the growth of each 2D material differently. In the following section, related literature review of 2D MoS_2 and 2D $MoSe_2$ grown by CVD method is presented.

2.2.3.1 CVD Growth of 2D TMDs: MoS_2 and $MoSe_2$

Unlike graphene and other carbon based 2D materials, CVD growth of 2D TMDs can be achieved by using solid precursors. The use of these solid precursors presents many challenges to uniform and large area growth of 2D TMDs. Some of these challenges include absence of self-limiting growth mechanism, non-uniform carrier gas and precursor vapor pressure in the growth tube, melting point difference of the solid precursors, sensitivity of the growth to the environment, to mention but a few. Therefore, researcher have done tremendous efforts to overcome these challenges. Such research efforts can be categorized into thermal vapor deposition (TVD), thermal vapor sulfurization (TVS), and other innovative methods.

In the TVD method, 2D materials are realized by the reaction of vapor precursors, such as MoO_3, S (for MoS_2), and Se (for $MoSe_2$). The vaporized precursors are carried to the substrates by the carrier gas for adsorption mechanism. Details of the CVD growth by TVD method are presented in section 3.1.2. The challenges mentioned above are peculiar to this method, and the efforts made by the researcher to overcome these challenges and grow large area and uniform 2D MoS_2 and $MoSe_2$ are summarized in high index review articles [16, 30, 47].

TVS technique, on the other hand, involves the annealing of transition metal precursor, deposited on the substrate, under chalcogen ambient (S or Se). The metal precursor deposition on the substrate has been achieved in several methods that include coating of $(NH4)_2MoS_2$ by spin and dip [48-50], and thermal evaporation of MoO_2 [51] or MoO_3 [52]. Similarly, TVS growth of $MoSe_2$ using MoO_3 film deposited by atomic layer deposition has been reported even though the recipe has to grow monolayer $MoSe_2$ has not been fully optimized [53]. Compared to the TVD this method has some merits and demerits: surface coverage with 2D materials is limited only by the size of the substrate on which the metal precursor is deposited; meanwhile, the 2D material grown by this method has small grain size and low crystallinity. To overcome these, post-deposition treatments, such as sintering, have been proposed [52]. Despite this, the film is reported to be polycrystalline, and the intrinsic properties of the film are affected by heat treatment.

2.2.4 Atomic layer deposition (ALD)

Atomic layer deposition is a modified version of CVD in which thin films are grown by introducing the vapor phase of the precursors to the reaction chamber stepwise. It can be said that ALD can overcome some of the drawbacks of the CVD method (outline in the previous section) by providing a self-limiting growth mechanism. Details about ALD can be found in section 3.1.2 of this report. TMDs are the common 2D materials that are reported to be grown by ALD. For instance, ALD growth of 2D MoS_2 and $MoSe_2$ are reported using metal precursors such as $Mo(CO)_6$ [54-56], $MoCl_5$ [56-59], and $Mo(thd_2)$ [60] and chalcogen precursors such as H_2S [55, 57-59] or $(CH_3)_2S_2$ [54] for MoS_2 and $((CH_3)_3Si)_2Se$ [56] for $MoSe_2$. Despite the successes recorded by using ALD, it has some drawbacks: the TMDs film grown by ALD is either amorphous or low crystalline, hence post deposition annealing under H_2S or S (for MoS_2) or Se ambient is necessary. Even after thermal annealing, the TMD flakes grown are by far smaller than those reported through CVD method (2.2 mm) [25].

2.2.5 Molecular beam epitaxy

MBE is also one of the top-bottom approach to the production of 2D materials. In this technique, film's deposition is achieved in an atomic layer by atomic layer manner by the reaction of atomic or molecular beams with a heated substrate. The deposition chamber needs to be under an ultra-high vacuum (UHV) to provide the atomic or

molecular beams with a mean free path (MFP) to the heated substrate [61]. By the sublimation of subtle materials residing in ultra-pure crucibles, the beams are produced. This, in addition to the lack of need for the carrier gas results in the deposition of film with ultra-high purity. Inspired by these, MBE have been used to grow a wide variety of 2D materials since the last four years; these include borophene, graphene, silicene, and stanene [62]. Among the 2D TMDs, $MoSe_2$ is grown by this method, and due so many factors that include the low sticking coefficient of the selenium atoms, the $MoSe_2$ flakes are reported to contain Se-vacancy [63]. Substrate dependence deposition is the major drawbacks of using MBE to grow 2D materials [64].

2.3 Characterization Techniques of 2D Materials

Characterization is the process of probing and measuring material's properties. After the production of a 2D material, it must be properly characterized to ascertain its properties such as its chemical signature and thickness. Some of the characterization methods of 2D material include optical microscopy, Raman spectroscopy, photoluminescence (PL) spectroscopy, Fourier transform infrared spectroscopy (FTIR), atomic force microscope (AFM), and spectroscopic ellipsometer (SE), scanning electron microscopy (SEM), transmission electron microscopy (TEM), x-ray photoelectron spectroscopy (XPS), x-ray diffraction (XRD), Hall effect measurement, etc. The use of these characterization techniques revolves around probing the materials properties such as physical, chemical, optical, electrical, magnetic and thermal. The most common characterization methods of 2D MoS_2 and 2D $MoSe_2$ are μRaman and PL spectroscopies. The working principles and necessary parameters for characterizing 2D TMDs using μRaman and PL spectroscopies are discussed in detail in section 3.4.3. In many cases, these characterization methods can be used to ascertain the number of layers in 2D TMDs as there exist literature works that can be used as a benchmark. The table below summarizes the peaks of the Raman vibrational modes and PL of 2D MoS_2 and 2D $MoSe_2$ as reported by several studies.

Table 2.1. *Optical bandgap, PL peak, work function, and Raman peaks of MoS_2 and $MoSe_2$.*

	PL Peak (eV)	Ref.	Raman Peak (cm^{-1})				Ref.
			E_{1g}	A_{1g}	E^1_{2g}	$\Delta\omega$	
MoS_2	1.82	[65-67]	-	404.0	383.0	21.0	[28]
	1.88	[29, 68]		406.2	385.7	20.5	[29]
	1.85	[27]		405.0	388.0	17.0	[69]
	1.83	[69]		403.4	384.6	18.8	[27]
	-	-		400.0	384.0	16.0	[12]
$MoSe_2$	1.57	[69-71]	-	238.5	284.2	-	[25]
	1.55	[72]	-	239.4	287.0	-	[70, 73]
	1.56	[25]	-	241.2	287.0	-	[72]
	1.48	[74]	-	239.0	301.0	-	[74]
	1.53	[73, 75]	-	-	289.0	-	[69]
	-	-	-	240.8	287.6	-	[71]
	-	-	145.7	240.4	286.8	-	[75]

2.4 Properties 2D Materials and Their Hetero Bilayer

What makes 2D materials more interesting and promising is the diversity of their properties. While some of the 2D materials are insulators, others are metals or semi-metal such as graphene and semiconductors such as TMDs. As a result of these different properties, they are strategically used for electronics and optoelectronics. Herein, a brief literature review about the fundamental properties electronic and optoelectronic properties of 2D materials (graphene and TMDs) is presented.

2.4.1 Graphene

Among the 2D materials, graphene is the most widely studied due to its exceptional properties that include mechanical strength of 130 GP [76], light absorption of 2.3% [77], thermal conductivity of 300 W mK^{-1} [78], and carrier mobility of 2.5 x 10^5 $cm^2V^{-1}S^{-1}$ [79] and this can go up to 10^6 $cm^2\ V^{-1}\ s^{-1}$ at low temperature [13]. Its chemical structure comprises of sp2-hybridized carbon atoms which are connected to each other by strong covalent bond forming hexagonal shape pattern with a unit cell parked in a honeycomb structure. Detail description of the electronic and optoelectronic properties of graphene are presented in these review articles [6, 80, 81]. Due to the unique properties of graphene, it is used for various applications, as outlined in the previous sections. Nevertheless, graphene has found limited application in electronics and optoelectronics due to the lack of band gap. Among other 2D materials found to have bandgap within visible and near infrared (NIR) are phosphorene, borophene, and TMDs [31].

2.4.2 Transition metal dichalcogenides (TMDs)

Due to the zero-band gap of graphene, interest in the study of the TMDs materials continue to gather momentum. TMDs are represented with the formula, MX_2 where M is a transition metal element from group 4 – 10 and X is a chalcogen element which can be either selenium (Se), Sulfur (S), or Tellurium (Te). Figure 2.4a shows the possible element combination, from transition metal as well as chalcogen, that results in TMDs. TMDs of transition metal elements from group 4 – 7 have layered structure, and about 40 of them exist. In the Figure 2.4a, partially highlighted elements from the transition metals in group 9 – 10 form layered structure with not all the chalcogen atoms. For instance, $NiTe_2$ and NiS_2 were found to have layered structure and a pyrite structure respectively [82]. In a unit cell of 1L TMD, there are 3 atoms which participate in a strong in-plane covalent bonding. In this bonding, the transition metal atom donates 4 electrons to the chalcogen atom, and consequently, the metal and chalcogen atoms end up having +4 and -2 oxidation states respectively [83]. Depending on the size of the chalcogen and transition metal ions, the bonding length of M – X atoms is between 0.315 nm and 0.403 nm [47, 83]. As a result, layered TMDs form a hexagonal pack of metal atoms sandwiched between two layers of chalcogen atoms, as shown in Figure 2.4b.

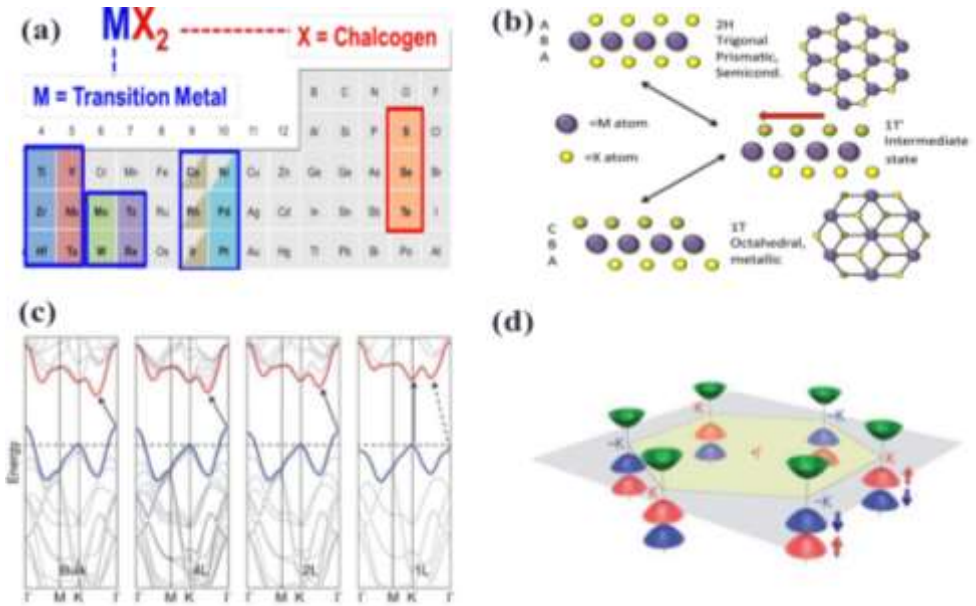

Figure 2.3. *(a) TMDs constituent elements in the periodic table (Han et al., 2015) (b) atomic structure of different phases of TMDs (Friedman et al., 2017) (c) E-k diagram of different layers of MoS_2 (Duan et al., 2015) (d) TMDs hexagonal Brillion zone (Wong et al., 2016)*

The most studied TMDs are MoS_2, $MoSe_2$, WS_2, and WSe_2. Each of these materials have two phases which have different electronic properties. These phases are octahedral metallic phase (1T) and trigonal prismatic semiconducting phase (2H). The major difference between these two phases is the coordination of chalcogen atoms with the transition metal atom as shown in figure 2.4b. ABA and ABC labeling are used to represent sequence of atomic transition metal (B) and chalcogen atomic (A and C) in 2H- and 1T-phase respectively [82, 84]. There exist an intermediate non-stable 1T'-phase which emerges due to lattice strain. This strain in TMDs is a result of excess charge supplied by surface dopants [84]. 2H-phase can be grown using either top-bottom [14, 70] or bottom-top [26, 47, 65, 66, 85, 86] approaches. 1T-phase is not the naturally default phase of the available TMDs, and it can be prepared by liquid exfoliation methods such as by oxidation of potassium thiomolybdate and lithium ion intercalation [87, 88]. In many cases, after the preparation process, 1T-2H mixed phase is observed [84, 89-91]. Studies also show the 1T-phase is meta stable and can transit to 2H-phase easily after aging or heating [46, 92].

In an ideal case, the surface of 2D TMDs is expected have no dangling bonds due to chalcogen atom termination [82, 93]. Therefore, a robust surface that is free from any defect or impurity, induced by the environment, is anticipated for the TMDs. These properties are essential for optoelectronic devices that are intended to be used for high performance because the number of trap-states is reduced [83]. Unfortunately, the dangling bonds are reported to be present in exfoliated or CVD grown TMDs flakes, in the form of S-vacancy. They emanate from processing during preparation or growth [94].

2H-TMDs are the most promising in optoelectronics because of their band gap. Interestingly, the band gap can transit from indirect to direct optical bandgap as a function of decrease in number of layers. In solid state Physics, E-k diagram, where E (eV) is energy and k (m^{-1}) is wavenumber, is used to illustrate the relationship between momentum and energy of the electrons and holes quantum states in a material. Difference between conduction band minimum (CBM) and valence band maximum (VBM) is called the band gap (E_g). Curvature of these bands is used to determine effective mass of the electrons and hole. The curve equally shows electrons and holes states in k space. Figure 2.4c shows the E-k diagram of bulk, 4-layer (4L), bi-layer (2L), and monolayer (1L)

MoS_2. Solid blue lines show the VBs while solid red lines show CBs. The horizontal solid dash lines show the energy of VBM at K point. Solid arrows show the lowest energy transition. Bulk – 2L MoS_2 have indirect optical bandgap with VBM at Γ point and CMB at K point. However, 1L MoS_2 has direct (vertical solid arrow) optical bandgap with CBM and VBM coinciding at K point. This phenomenon can be extended to $MoSe_2$.

The indirect to direct band gap transition from bulk to monolayer is as a result of quantum confinement effect [82] that originates from the strong spin orbital coupling and inversion symmetry breaking in the monolayer TMDs at K point of the Brillion zone [68] as depicted in figure 2.4d. These effects are an important area of study in the emerging field of Valleytronics in which 2D TMD valleys and spins are manipulated to process and encode information [95]. Besides, after the indirect-direct bandgap transition, optical bandgap energy of these materials increases due to quantum confinement effect. For instance, the indirect optical bandgap energy of bulk MoS_2 is ~ 1.2 eV and direct optical bandgap energy of 1L MoS_2 is ~1.8 eV [47]. This increase in bandgap energy is manifested in a strong PL emission intensity in monolayer compared to its bulk counterpart. In addition to their direct bandgap, 2D TMDs have a high absorption coefficient (α). For instance, the α value of 2D MoS_2 reaches up to ~10^6 cm^{-1}, and this is higher than those of Si, Perovskite, and GaAs [68, 96].

2.4.3 Hetero bilayer system based on 2D TMDs

Following the remarkable achievements in the growth of 2D materials, research advancement has made possible the formation of heterostructures of different materials with different number of layers. The resulting heterostructure will have tailored properties that cannot be achieved otherwise. The simplest form of heterostructure is the hetero bilayer just as the one fabricated in this study. Hetero bilayer can be formed by epitaxial growth or transfer on the second layer to first layer. To achieve functional hero bilayer, the lattices of the layered materials must be aligned. Interestingly, for the hetero bilayer based on 2D TMDs, the alignment of the lattices is not a requirement [14, 17].

Hetero bilayer based on 2D TMDs can be formed in two ways, i.e. vertically or laterally. While the lateral hetero bilayer can be formed only by one-step or two-step CVD, the vertical hetero bilayer can be formed by mechanical exfoliation, CVD (one- or two-step), or transfer methods [13, 14, 16, 17, 20, 21, 71, 97-108]. Clean interface of the vertical hetero bilayer is a determinant factor of its quality. As a result, the CVD method

produces the highest quality structures. Nevertheless, hetero bilayer with high-quality can be produced by using either mechanical exfoliation or transfer methods, depending on cleanliness of the environment and post-treatment parameters used. The purpose of the heterostructure formation is to take advantage of the individual layer properties some of which add up. For instance, report shows that the light absorption of MoS_2 and $MoSe_2$ adds up in the hetero bilayer [18]. Moreover, it is possible for monolayer materials that participate in the hetero bilayer to retain their direct band gaps with the optimum interlayer distance [20].

TMDs hetero bilayer forms a staggered type-II band alignment due to the difference in their bandgaps, as will be seen in the subsequent chapters. Also, because of the difference in the work function and Fermi levels in these materials, charge transfer occurs between the layers [18, 20, 21, 105, 107, 108]. For instance, in $MoS_2/MoSe_2$ hetero bilayer, electrons at the CBM of the low work function material ($MoSe_2$) flow to the CBM of the high work function material (MoS_2). Conversely, holes at the VBM of a MoS_2 flow to the VBM of $MoSe_2$. As a result, there will be net positive charge in the $MoSe_2$ and net negative charges MoS_2. This effect is manifested by a strong PL quenching of the hetero bilayer relative to that of the individual layers as a result of indirect recombination of the EHPs [20]. This is true only in the case of hetero bilayer formed by one- or two-step CVD method. Hetero bilayer formed by transfer method needs to be annealed to reduce the interlayer distance to an optimum condition, thereby achieving some interlayer coupling. It shall be noted that even in the hetero bilayer formed by one- or two-step CVD method, there exist 0.1 nm exists interlayer distance [99]. Detail about the hetero bilayer formation and properties are presented in the relevant sections of this report.

2.3 Optoelectronic Applications of 2D Materials and Their Hetero Bilayer

Optoelectronics is a field of study, considered as a branch of photonics, that focuses on the theory, design, production, and operation of devices and systems that detect, source, or control light. In this perspective, light consists of any radiation that has a wavelength within the visible, infrared, ultraviolet, X-rays, and gamma rays. Optoelectronic devices either generate electric charge to produce light, like lasers and light emitting diodes (LED), or utilize light to produce electric charge, like photodetectors, phototransistors, photovoltaic, and optical random access memory (ORAM). Depending on the physical process responsible for the charge or photon

generation, an optoelectronic device working principle can be divided into photoconductivity, photoelectric effect, radiative recombination, stimulated emission, and photoemission [109].

Optoelectronic device development began in 1960s, and then, attention is on the LED and laser applications. The semiconductor materials used are the III-V such as GaAs, InP, GaSb, GaN and their alloys, owing to their direct bandgap which make them suitable as light source [2]. However, these materials – especially GaAs – are expensive due to their scarcity. The natural abundance of silicon has been the motivation for its exploitation in optoelectronics, especially solar cells. Meanwhile, on a general note, silicon has seen limited optoelectronics applications (especially, in photo-emission applications) due to its indirect ban gap.

Recently, 2D TMDs has attracted tremendous research interest due to their interesting properties that include a direct band gap ranging between 1 eV and 2.3 eV, within the visible and near infrared (NIR) spectrum, and their absorption coefficient of 10^6 cm^{-1}. Inspired by this, researcher across the globe have reported different success stories about 2D TMDs device performance especially in the area of photo-detection and photoemission. Reported herein is a brief literature review on the 2D materials (with emphasis on 2D TMDs and their hetero bilayer systems) as applied in photodetector, phototransistor, LED, and laser.

2.3.1 Photodetectors/phototransistors

For the fast 20 years, the research in semiconductor optoelectronics has focused on the optical communications, imaging, and spectroscopy. Optical communication market especially have seen a high demands in the ability to sense low optical signals, during a high data rate transmission (>40 Gbit/s) [1]. In this context, photodetectors and phototransistors are the relevant optoelectronic devices used, and their prerequisites figures of merits include high responsivity, sensitivity, fast response time, and low dark current. The operation of these devices is based on the principle of photoconductivity effect, i.e. EHPs generation by an incident photon leading to the transition of an electron from the valence band to the conduction band in a semiconductor material. Quantum efficiency is the ultimate figure of merit that is used to determine the number of electrons per incident photon. The working principles of the photodetector and phototransistor are the same, except that the phototransistor uses a gate voltage to modulate the flow of the

charge carriers from source to drain of the circuit. Detailed information about the working principles of the photodetectors and phototransistors can be found in review articles [110, 111].

In recent years, 2D TMDs have attracted attention to fill a niche in optoelectronic applications due to their interesting electrical and optical properties outlined in the previous sections, and $MoSe_2$, MoS_2, and WS_2 are the TMDs members that are at the forefront. The first photodetector based on monolayer MoS_2 prepared by mechanical exfoliation exhibits a significant photoresponsivity of up to 7.5 mAW^{-1} at 670 nm [12]. Later, a significant improvement in the photoresponsivity of monolayer MoS_2 to 880 AW^{-1} at 561 nm is reported by Lopez-Sanchez *et al.* [112]. $MoSe_2$ also shows an promising photoresponsivity of 238 AW^{-1} by an excitation laser within the near-infrared spectrum [113].

To date, various innovative designs, aimed at improving the quantum efficiency of the photodetector, are proposed in various studies. Some of the problems the researchers endeavor to address in this area include improving the spectral absorption (limited by the band gaps), the overall absorptions (owing to the low thickness of 2D material), and faster photocurrent separation and transport. To mitigate these problems, photodetectors based on heterostructure of different materials, like graphene or TMDs, are fabricated. Yu *et al.* reports a highly efficient phototransistor based on graphene/MoS_2 (16 nm)/graphene, and the device shows an internal quantum efficiency (IQE) of 85% and external quantum efficiency of 55% [114]. Also, Xue *et al.* reports a scalable fabrication of photodetector array based on few layer MoS_2/WS_2 heterostructure [115]. The research in this area is a work in progress as researchers try to fix the major drawbacks of the of photodetectors based on heterostructure that include the limitation of the device performance due to photoresponsive area (the metal-2D material contact region) and defects within the hetero interface [116]. A more detailed information about the progress made so far are reported in various review articles [38, 116-118].

2.3.2 Solar cells/photovoltaic devices

Photovoltaic cell or solar device is an optoelectronic device that detects and converts light directly into electricity by photovoltaic effect. Solar cell is a form of photoelectric device whose voltage, current, and resistance change upon illumination with light. To form a solar panel, otherwise known as solar module, individual solar cells are

ensembled. Three attributes are required for the operation of solar cell: (a) light absorption to generate EHPs (b) separation of charge carriers and (c) transportation of the charge carriers to the external circuit. Semiconductor devices such as Si, Ge, and GaAs are used as active materials in solar cell. The use of Si dominates the solar cell industry due to its natural abundance. The recent paradigm shift in the electronic and optoelectronic industry necessitates the pursuit for the next generation materials that are suitable for ultrathin and flexible yet cost effective solar cells. This results in the dedication of endeavors to explore the potential of 2D materials in the solar cells applications [119].

The work in the area of photovoltaic cells based on 2D materials is still at an infant stage [120, 121]. There are few attempts to use TMD materials for photovoltaic device, and the results are promising. Perhaps the use of the TMD materials in solar cells application is inspired by their absorption within visible and near infrared bands of the solar spectrum [18]. In addition to their relatively high absorption coefficient (~10^6 cm^{-1}), monolayer TMD material can absorb up to ~ 10 % of solar irradiance; and this can be scaled up by absorption engineering [68]. For the first time, Kis *et all*. report the MoS_2/p-silicon heterojunction [122]. The device exhibits light harvesting and facilitates separation of photocurrent EHPs due to the built-in electric field, and the device shows an EQE of 4 % [123]. Later, further improvement in the solar cell's EQE of 5.25 % is reported by Jr-Hau He *et al.* [67].

The performance of solar cells can be improved by (a) growing a large-area material with layer and size control, (b) careful control of the doping levels of silicon and TMDs (to reduce the series resistance of the device) [124-126], forming a heterostructure with another 2D material of different band gap to compensate for the absorption spectral range each other. Therefore, Mueller *et al.* reports a p-n junction of WSe_2 that is electrostatically doped to exhibit photovoltaic characteristics with a power conversion efficiency (PCE) of ~0.5% [124]. Later, Duan *et al.* reports a sharp and atomically thin photovoltaic device, using WSe_2 and few layer n-type MoS_2, with an EQE of up to 12% [127]. Sun et al. reports an ultrathin solar cell, by incorporating PTB7:$PC_{71}BM$ with MoS_2 nanosheets (prepared by liquid exfoliation technique), to exhibit a PCE of up to 8.11% [128]. A 100% improvement to this is reported by Chen *et al.* via incorporating a layer of graphene with silicon and using an interfacial layer of MoS_2 [129]. This achievement is due the type II band alignment formed between the MoS_2 and n-silicon, which facilitate the carrier

transportation between the two materials. With an increase in the thickness of MoS_2, they observe a steady rise in a solar cell's PCE, which saturates with 2 nm thick MoS_2. A more promising solar absorption of up to 90% is observed by using MoS_2/graphene/hBN heterostructure rolled up in a spiral structure [130]. More information about the progress and challenges of using 2D materials for solar cell/photovoltaic application are presented in a recent review article [96].

2.3.3 Light emitting diode (LED)

In a direct band gap semiconductor, light emission or luminescence can occur spontaneously. Electrons at the conduction band (with an energy E_2) recombine with the holes at the valence band (with an energy E_1) to release photons with the energy, $E_2 - E_1$. In this process, photons are randomly emitted in any polarization and direction. The probability of spontaneous emission is directly dependent on the density of holes (*p*) in the valence band and electrons (*n*) at the conduction band [1]. Due to their direct bandgap, 2D TMDs have seen applications in the area of LED. To fabricate LED using TMDs, a p-n junction is a perquisite for recombination of the EHPs [122, 124, 125, 127, 131, 132]. As a result, two propositions are made (a) forming a vertical heterostructure with distinct semiconducting type and (b) applying an adequate source-drain voltage locally to invert the channel's potential with respect to the gate [131]. Therefore, Steiner et al., inspired by carbon nanotube (CNT), shows luminescence at 1.8 eV in a monolayer MoS_2 FET device by electrostatic excitation [127]. Later, Morpurgo *et al.* demonstrates LEDs based on monolayer and bilayer of WSe_2 by introducing an electrolyte gating [133, 134]; the electrolyte's anions and cations migrate to the semiconductor surface and the gate electron respectively when the gate voltage is applied, forming large capacitance electric double layer [134].

For light emission in the ambipolar regime of the TMDs based FET, electron and hole charges are accumulated in the channel to create a tunable p-n depletion region for the recombination of the charge carriers. By this method, Zhang *et al.* reports that to break the inversion symmetry in a multilayer TMDs, effective gate bias is enough [135]. By forming a vertical heterostructure that consists of various layers of TMDs, graphene, and hBN, recently, Noveselov *et al.* reports a 2D quantum well (QW) that shows an EQE of up to 10% with tunable emission over a broad range of wavelength [132]. By increasing the number of layers of the 2D active materials to enhance electronic quality of the

heterostructure, the work by Noveselov *et al*. can have more functionality. In this regard, the future research endeavor will be devoted to the design of a suitable landscape for electrons life the heterojunction of different 2D crystals by band alignment engineering [132]. Also, the fabrication of the heterostructures on transparent and flexible substrates is another area of research interest.

2.3.4 Lasers

Lasers are among the light emitting optoelectronic devices that is based on the stimulated emission of photons in a semiconductor material. Light emission, in lasers, occur when a photon (with an energy, $E_2 - E_1$) induces a recombination of an electron, in a conduction band, with a hole, in valence band, leading to a generation of a photon having identical wavelength, momentum, and phase with the incident photon. Unlike the spontaneous emission, the chances of a stimulated emission occurring further depend on the photon density [1]. A candidate semiconductor material for laser (especially pulse laser) application shall therefore be such that have nonlinear optical properties. Of all the types of laser, ultrafast laser is the most promising for variety of applications such as in materials processing, telecommunications, medicine, high-speed optical communication, etc. [128, 136]. In the majority of ultrafast laser, a mode-locking technique is used, in which a saturable absorber (as a nonlinear optical element (NOE)) changes a wavelength that is continuous into a pulse train. The NOE can achieve the mode-locking either in an active or passive way. In the former, the NOE serves as a modulator, providing a frequency or amplitude modulation; while in the latter NOE is added into the cavity that provides the modulation to generate the pulses train [116].

Therefore, the following properties are required for a candidate NOE: (a) strong nonlinearity, (b) fast response time, (c) low optical loss, (d) broad range of wavelength, low cost and power consumption, (d) handling high power and (e) ability to be integrated into an optical system easily [137]. Single-walled CNT and semiconductor mirrors are the conventional materials used as saturable absorbers. The drawbacks of using the semiconductor saturable absorber mirror (SESAM) include complex fabrication and packaging processes. On the other hand, SWCNT saturable absorber is easy to fabricate to obtain a wavelength with variable resonance by simply playing with the chirality and diameter of the CNT; however, one of the major drawbacks of SWCNT is the extreme optical loss beyond its wavelength [137-141]. Even though graphene exhibits various

saturable absorber properties, it undergoes non-saturable losses [142, 143]. The best option for saturable absorption turns out to be the topological insulators (TIs) 2D materials analogs of graphene such as Bi_2Se_3, Bi_2Te_3, and Sb_2Te_3, etc. The bulk counterpart of these material behaves as a narrow band gap insulator, with a surface area that is conductive [143-146]. The surface of these materials exhibits a linear band dispersion that is Dirac-like, similar to graphene [140, 147]. Due to the Pauli blocking, upon excitation of the TIs with light that have an energy greater than their insulating band gap, they display ultrabroadband saturable absorption [138, 140]. An in depth information on the progress made in this area is presented in a review article [116].

3. EXPERIMENTAL PROCEDURE

3.1 Material Growth

Each material used for this study is grown either on SiO_2/Si or glass substrates. A Si substrate has a thickness of 525 ± 25 μm with 300 nm SiO_2 coating and variable dimensions. Glass substrate has a thickness of 0.13 – 0.17 mm and dimension of 2 x 2 cm^2. 3-solvent cleaning procedure is applied in cleaning each substrate. This involved cleaning using acetone, isopropanol and DI water for 5 minutes each in ultrasonic bath at 53 Hz. Subsequently, each substrate is dried by purging with N_2 (99.99%) followed by 5 minutes annealing on a hot plate at 70°C.

3.1.1 Atomic Layer Deposition

ALD is a modified CVD system in which vapor phase deposition technique is used to deposit films of various materials. It is based on self-limiting growth mechanism, and this means there will not be additional chemical bonding once the reaction sites are fully covered. ALD provides 3D conformal deposition on a high aspect ratio structure. Unlike CVD, gas phase reaction is avoided in ALD by introducing precursors vapor into the chamber separately and deposited in cycles. Each ALD cycle comprises of at least four steps: (1) pulsing of the first precursor (2) followed by purging (3) pulsing of the second precursor and (2) followed by purging. In practice, growth rate in ALD is ~ 1 Å/cycle [148]. Film thickness can be controlled in ALD by changing the precursor pulse time. Theoretically, each pulse results in one atomic layer; however, sometimes the result is a sub-monolayer due to steric hindrance in which a large molecule of a precursor occupies space making it impossible for another precursor molecule to come close and for surface atoms to react with it.

Unlike CVD, ALD operates at lower temperature, usually ≤ 500 °C. Additionally, plasma gas can be used in plasma enhanced-ALD (PEALD) to break precursor's atomic bonds, thus reducing the heat energy requirement of the process, as used in this study. Operating parameters in ALD include deposition and precursor temperature, deposition pressure, carrier gas flow rate, plasma power (for PEALD), number of cycles, precursors pulse and purge time. A very critical parameter in ALD growth is the deposition temperature window. For instance, MoO_3 has a temperature window of 150°C - 172°C outside which there will be low reactivity (<150°C) or thermal decomposition of $Mo(CO)_6$ precursor (>172°C) [149]. Real time monitoring of the deposition process can

be possible by integrating either SE or quartz crystal microbalance (QCM) with the ALD tool. Our ALD tool is shown in figure 3.1b. Beneq TFS 200 ALD reactor, has deposition temperature range of 25°C – 500°C, plasma option with up to 300W, 4 liquid precursor source (5°C – ambient), 3 hot source (2x ambient – 300 °C and ambient to 500 °C).

In this study, Beneq TFS 200 ALD reactor is used to grow MoO_3 with different number of cycles. The parameters used for the deposition process are mentioned in the relevant sections of this report. The deposition and precursor temperature are monitored by two thermocouples which measure the sample holder and chamber ambient. The reactor base pressure is ≤ 1 mbar before deposition and 5-7 mbar when the deposition is in progress. Each of the MoO_3 deposition parameter is kept constant except the number of cycles which is varied between 1 to 600 in order to have MoO_3 films with different thickness.

3.1.2 CVD growth of monolayer MoS_2 and $MoSe_2$

CVD is one of the most powerful and widely used vapor phase deposition techniques for 2D materials growth. CVD reaction is determined by choice of reactor. CVD reactors can be categorized by architecture (such as tube reactor) or growth process (such as hot wall or cold wall). In a typical tube reactor hot wall CVD system, key parameters for film growth are temperature, precursors ratio, distance between precursors and substrate (d_2), pressure, and carrier gas flow. The choice of these parameters affects the material crystal morphology, phase, orientation, doping, number of layer, and quality [16, 150]. A typical growth process of 2D materials in CVD is as follows: precursors and substrates arranged on a quartz glass and then inserted into tube reactor. A program, which includes temperature and time, is set. A pressure is set, and carrier gas(es) in sccm is(are) introduced.

As soon as the program is started, temperature ramps up to reach the growth temperature, and this is maintained for a time duration as set in the recipe. It is during this time that material growth occurs. In CVD growth of 2D TMDs for instance, there are two important steps namely nucleation and growth [150]. Nucleation begins at ~700 °C when metal oxide (i.e. MoO_3) begins to vaporize and deposit onto the substrate surface, creating nucleation centers. Growth occurs at the growth temperature when the chalcogen (S or Se) vapor, carried by carrier gas, reduces the metal oxides to form a volatile suboxide (MoO_{3-x}); and subsequently, the S or Se reacts with the MoO_{3-x} leading to the growth of

either MoS_2 or $MoSe_2$ and some bi-products [85]. 2D TMDs growth starts at the nucleation centers and laterally increases in dimension to form a crystal morphology determined by growth experimental parameters [151]. The glass that is used to grow 2D TMDs in this study contains NaO_2 compound, and report show that during the growth, an intermediate Na-containing compound is formed after the reduction of the MoO_3 by sulfur vapor [103].

In this study, a home-built CVD system (PROTHERM furnace) is used to grow monolayer MoS_2 and $MoSe_2$ flakes. The system comprises of 140 cm long quartz tube with 7 cm (used for ALD assisted CVD experiments) or 8 cm in diameter (used for the conventional CVD experiments), two controllable heat zones, carrier gas mass flow controller (MFC), stainless flanges, vacuum pump, chiller and pressure gauge. Before each experiment, the tube is cleaned at 1000°C with 500 sccm N_2 flow under vacuum, and the furnace furnace is allowed to cool down naturally. Except for the ALD assisted CVD experiment, point to point growth configuration is adopted as shown in the subsequent sections. S/Se precursor is kept upstream outside the movable heatzones so as to avoid its early evaporation which may result in an unsuccessful experiment. Upon reaching growth temperature, the furnace is pulled upstream in order to bring the S/Se precursor into the heatzones for sufficient mass flux of the precursor's vapor. After each experiment, the furnace is turned off; the upper part is open and allowed to cool naturally. Details about the growth configuration and parameters used for the growth of monolayer MoS_2 and $MoSe_2$ are presented in the relevant sections of this report.

3.2 PMMA Assisted Transfer

2D materials are bonded to a substrate by a weak van der Walls (vdW) force. Using a proper approach, they can be removed easily and transferred to another substrate. PMMA assisted wet transfer is one of such approach. Poly(methyl methacrylate), PMMA, is a transparent thermoplastic polymer which is in liquid form and solidifies after being heated. It is used in this study to transfer materials from glass substrate to a target substrate either SiO_2/Si or $MoSe_2/SiO_2$/Si (for hetero bilayer case). First, each sample is spin coated with PMMA at a spin speed, acceleration, and spin time of 750 rpm, 500 rpm/s, and 40 s respectively. The sample is annealed on a hot plate at 130°C for 2 minutes. The PMMA on the edges of the annealed sample is gently removed using a sharp knife. In order to separate PMMA from substrate, the sample is slowly inserted into a beaker full of DI

water at an angle of ~45°. This causes the PMMA to delaminate from the glass substrate due to its hydrophilicity. The PMMA/TMDs, floating on water, is then fished out using a target substrate and baked at 70°C until it completely adheres to the substrate. The PMMA is dissolved in an acetone bath at 65°C for ~30 minutes. Schematic illustration of this method is shown below in figure 3.3.

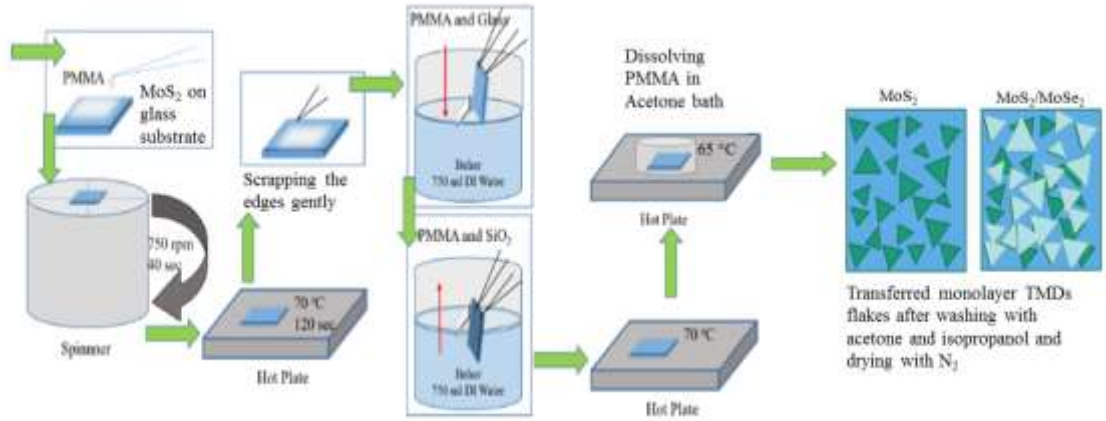

Figure 3.1. *Schematic illustration of PMMA-assisted wet transfer of MoS_2 flakes from glass substrate to SiO_2/Si or $MoSe_2$/SiO_2/Si to form heterostructure of MoS_2/$MoSe_2$*

3.3 Annealing

In this study, we perform annealing process using two different methods. Firstly, the as-deposited MoO_3 (a-MoO_3) films are annealed under atmospheric ambient at a temperature varied between 200 °C and 600 °C and time varied between 6 and 10 minutes. This annealing procedure is adopted to significantly minimize the rate of MoO_3 crystal vaporization in the course by avoiding any carrier gas flow and maintaining atmospheric ambient. Secondly, the MoS_2/$MoSe_2$ hetero bilayer system and transferred MoS_2 are at 200 °C for 2 hours with 100 sccm Ar flow and at 200 torr. The recipe used in this annealing experiment is an optimized recipe that is reported to get rid PMMA residues introduced during the transfer and fabrication process, and improve the flakes-substrate and metal contact-flake adherence (to reduce the contact resistance) [86].

3.4 Material Characterization Methods

3.4.1 Spectrometric ellipsometry

Variable angle spectroscopic ellipsometer (VASE) is a powerful and precise tool for characterizing the thickness and refractive index of thin film using polarized light. In this study, J. A. Woollam Co., Inc. WVASE Spectroscopic Ellipsometer is used to characterize the a-MoO_3 films. The VASE is equipped with rotation analyzer which ensures maximum data accuracy near Brewster's condition. Likewise, it enables measurement at a wide spectral range between 240 nm and 1200 nm. During the measurement, the polarized light interacts with the a-MoO_3 thin film at an angle near Brewster's angle. Polarization change of this light is detected by the polarization analyzer and presented in a graph of psi and delta against wavelength. To find the thickness, this data is fitted using a model of the film existing in the library. By careful optimization of the model, a match with the measured data, with the least mean square error (MSE), is determined. Using this data, refractive index of the a-MoO_3 film is obtained at 632 nm wavelength.

3.4.2 Atomic force microscopy (AFM)

AFM is used to measure surface topography of a material by scanning a sample with a nanometer scale cantilever. Basically, an image is produced in AFM by measuring forces between sample surface and a cantilever tip (probe). Nanomagnetics Instrument azAFM tool is used to take the measurements. The tool has a maximum scan range of 40 x 40 x 4 μm and a sample of size up to 10 x 10 x 5 mm can be scanned. In this study, tapping mode is used to obtain each AFM image. In tapping mode, the cantilever tip oscillates near its resonance frequency very close to the sample surface. As the ZY motor moves the cantilever across the sample surface, the oscillation amplitude and resonance frequency change due to the change in forces between the probe and sample surface. A feedback loop is used to keep track of these changes and ensure that constant root mean square amplitude is maintained. This mechanism provides surface roughness information of a sample which includes sample thickness that is important in determining material number of layers. In this study, AFM measurements are carried on the MoO_3 films, monolayer MoS_2, monolayer $MoSe_2$ and hetero bilayer $MoS_2/MoSe_2$. In each measurement, the scanned area is 1600 μm^2, and tapping mode is used to avoid damaging the test sample and to keep the material intact.

3.4.3 μRaman and photoluminescence spectroscopy

Raman spectroscopy is one of the most common nondestructive tools for 2D materials' characterization. The method is based on inelastic scattering of monochromatic light from lattices vibrations of a sample. Basically, a sample is illuminated with a laser beam. From the illuminated laser spot, electromagnetic (EM) radiation is passed through a monochromator. The monochromatic light with a wavelength within visible, near infrared, or near ultraviolet (UV) interacts with a molecule in the sample. This interaction makes band electrons to absorb the light and because of inelastic scattering with phonons of certain momentum and energy values, they transit across virtual energy states. Subsequently, deexcitation occurs at the optical bandgaps, other defects or phonon within the crystal.

During the interaction of molecule with light, there are two forms of scattering that take place: elastic and inelastic scattering. The former, also called Rayleigh scattering, is very strong in crystals and has photon energy equal to that of the incident light. The latter is called Raman scattering and has photon energy less (strokes Raman scattering) or more (anti-strokes Raman scattering) than that of the incident light. The shift in energy relative to that of the incident energy is called Raman shift and is directly proportional to the vibrational energy of some phonon modes at the Brillion zone's symmetry points of the material. This phonon mode is unique for every material's compound hence provides chemical fingerprint for a sample. In a typical Raman spectrum of a material, only strokes scattering is shown as a line filters and notch filter are used to separate the very intense Rayleigh and high-energy anti-strokes scatterings from weak Raman (strokes) scattering. Other information obtainable from Raman includes strain and stress state, number of layers, defect, degree of crystallinity, and crystal orientation and symmetry.

PL spectroscopy is also a nondestructive and widely used characterization technique for semiconductor materials. PL occurs when monochromatic light, having an energy that is equal or higher than the material's bandgap, is absorbed by the material. Electrons at the lower energy band/states of the material are excited to higher electronic band/state; the electrons relax to certain energy state and after some time, they fall back to the ground energy state by releasing some photon. The energy or the wavelenght of the PL peak, in a direct bandgap semiconductor is approximately equal to the optical optical bandgap of the material. As a result, PL is considered to be a measure of the material's

bandgap. Excited electrons are binded to their holes by some binding energy in form of electron-hole pair (EHP), and this binding energy is greater than few millielectron volts.

Both Raman scattering and PL can occur when a sample is illuminated with a monochromatic light. However, Raman scattering is many times weaker than PL and involves photon interaction with the phonon. PL depends on band to band transition of electrons. For instance, this transition, in a direct optical bandgap materials such as 2D TMDs, is purely vertical and accounts for only electron energy change excluding momentum change, as shown in figure 3.7c. This results in radiative recombination without any inelastic process. From this process, PL peaks are generated which are dependent on deexcitations of electron-hole pairs of direct optical bandgaps.

In this study, WITec Alfa 300 R – Confocal Raman and PL tool is used. In both the μRaman and PL characterization, 532 nm excitation. 1200 grooves/mm and 600 grooves/mm gratings are used respectively for the μRaman and PL spectroscopy. The choice of the laser wavelength is for spatial resolution and sensitivity of the charge couple device (CCD) camera. Unless otherwise stated, an objective with 100x lens, numerical aperture (NA) = 0.9, is used to provide a laser spot size of $2\lambda/\pi NA = 0.4\,\mu m$. Throughout the study, a laser power of 0.5 mW is used. For the image scan, the number of vertical and horizontal points scanned are at least 5 times the height of the scanned area. The fittings of the μRaman and PL spectra are performed using the inbuilt Lorentz model and Gaussian models respectively in the OriginPro 9.0 to find out the peak and full width half maximum (FWHM) of each material. Raman peaks of MoS_2 and $MoSe_2$ corresponds to either of the vibrational modes shown in figure 3.8.

3.4.4 Fourier transform infrared (FTIR) spectroscopy

While Raman-active vibration occurs when there is change in the polarization, infrared-active vibration occurs when there is change in dipole moment. Molecules of some materials are exhibit infrared-active type of vibration, so their lattice vibrations can be probed using light within mid-IR region of the EM spectrum. Therefore, FTIR spectroscopy, which uses IR light source, is used to probe these materials and determine their molecular fingerprints. Stretching and bonding are the two types of vibrations in molecules probed in the FTIR technique. Stretching vibration (ν) is related to the movement of atoms along its bond with change in distance. Bending vibration (δ) is only observed in poly-atomic bonds, and it involves movement of atoms exhibiting angular

changes of its bonds such as wagging, twisting, scissoring and rocking. These vibrations are a direct consequence of mid-IR light absorption of the molecule and are observed (in a wave number range of approximately 500 – 4000 cm^{-1}) only when the vibrations cause changes in the molecular dipole moment of the test sample. An attenuated total reflectance (ATR) mode can be used together with FTIR. Some of the advantages of ATR-FTIR include the minimal or non-convoluted sample preparation, real-time analysis of processes, simultaneous measurement of a sample [152]. In this study, ART Tracer-130 FTIR with ATR mode is used to characterize both the as-grown and annealed MoO_3 films. The FTIR measurements of the samples are performed as follows:

1. Before placing the sample on the stage, a background signal is collected and later subtracted from the spectra of the measured sample.
2. The sample is placed on the stage, and spectra of the material on the sample are gathered either in absorbance, transmittance, or reflection mode. In this study, absorbance mode is used.
3. The collected spectra are then transferred to a library program where they are compared with the spectra in the library. The measured spectra are confirmed if a best match is found in the library.

4. LAYER AND SIZE DISTRIBUTION CONTROL OF 2D MoS_2 BY ALD-ASSISTED CVD METHOD

4.1 Introduction

As a member of 2D TMDs, MoS_2 is a promising candidate for future optoelectronic applications due to its interesting properties such as direct band gap of 1.82 eV [65] and absorption coefficient of 10^6 cm^{-1} [68]. 2D MoS_2 was first produced by mechanical exfoliation [11] and later on using a more scalable production method such as CVD. Unlike in the mechanical exfoliation method, the growth of 2D MoS_2 by CVD method is more complicated as many parameters (such as the precursor ratio, temperature, carrier gas flow rate, growth time, to mention but a few) need to be under control. The control of these parameters provides a convenient ambient for the S and Mo (usually MoO_3) precursors to react in vapor phase and form monolayer MoS_2 flakes on a substrate. In many cases, this method does not yield large area and uniformly distributed MoS_2 crystals [26, 65, 66, 85]. Consequently, optimization of multiple parameters such as gas flow [28], ramp-rate [153], growth configuration type [65], precursor ratio [65], and use of co-reagents such as O_2 [154], and H_2 [65] become necessary to achieve this goal.

Alternatively, monolayer TMDs can be grown using metal oxide films deposited by ALD. Recently, a different route was followed by Dai et al. to grow few layers of $MoSe_2$ using the sulfurization of MoO_3 film grown by PEALD [53]. However, this method has not yet been optimized for the growth of monolayer $MoSe_2$. Before this report, Song et al. reported the growth of monolayer WS_2 by sulfurization of WO_3 deposited by ALD [155]. By characterization using XPS, μRaman and PL, the monolayer WS_2 was found to have good stoichiometry.

Herein, we report the growth of monolayer MoS_2 on a SiO_2/Si substrate with size and layer control. In this method, instead of the MoO_3 powder used in the conventional CVD method, MoO_3 films that are grown by PEALD are used. We have demonstrated that by using MoO_3 film of different number of cycles, the number of layers and flakes size and distribution can be controlled. The MoO_3 films grown are amorphous as confirmed by the SE, μRaman, AFM, and ATR-FTIR characterizations. The μRaman, PL, and AFM analysis confirms that the 2D MoS_2 flakes are of high quality.

4.2 ALD Growth and Characterization of MoO_3 Films

ALD growth of MoO_3 film can be achieved by using different parameters and precursors, and depending on these, MoO_3 films can be grown at different temperature.

The first growth of MoO_3 film by ALD is achieved using $Mo(CO)_6$ and O_3 as Mo and O precursors respectively at 163 °C as reported by Diskus et al. [156] and at 120 °C by Liu et al. [157]. Mattinen et al. reported the growth of MoO_3 films, but instead of $Mo(CO)_6$, they used $MoO_2(th)_2$ [158]. Unlike the previous reports, they obtain a highly crystalline MoO_3 film, but their growth temperature window is between 200 °C and 275 °C. In their newly developed PEALD method, Macco et al. also reported the deposition of MoO_3 by using a similar O precursor but a different Mo precursor being the $(NtBu)_2(NMe_2)_2Mo$ [159]. They were able to grow the MoO_3 film at a drastically low temperature (50 °C). Dai et al. recently reported the high-k dielectric property of MoO_3 film deposited by ALD using $Mo(CO)_6$ and O_2 at 162 °C [149].

In this study, MoO_3 thin films are deposited on a 1x1 cm Si substrate at 160°C. $Mo(CO)_6$ (99.99%) and O_2 are used as Mo and O precursors respectively. The Mo precursor is heated to 35 °C (~ 0.5 mbar) to produce enough pressure for the process. N_2 is made to flow into the MoO_3 precursor holder, carries and delivers it into the chamber at 300 sccm. O_2, with a pressure of 2 bar first flows through the plasma and is then carried into the reaction chamber by N_2 through the top of the reaction chamber with a pulse time of 3 seconds. 3 seconds purge time is used for each precursor, and N_2 gas with a flow rate of 250 sccm is used throughout the experiment. O_2 plasma is used as an oxidant and is generated using the 100 W RF.

Figure 3.1 shows the thickness of the a-MoO_3 as a function of number cycles for 150-, 300-, and 600-cycles a-MoO_3 films. From the graph a steady increase in the thickness with the increase in the number cycles are observed. After fitting the curve with the linear function, growth per cycle (GPC) of 0.09 ±0.05 nm/cycle is obtained. It can be observed that a considerable number of error margins exist on the calculated GPC, and this suggests that the thickness of 1- and 25-cycle a-MoO3 film is ~ 0.1 and 1 nm respectively. It also shows that the < 50-cycle a-MoO_3 films are not continuous as there is quite a considerable amount of SiO_2/Si surface not coated with the a-MoO_3. Therefore, it can be commented that 50-cycle is the beginning of a continuous a-MoO_3 film deposition. Similar growth mechanism has been observed in the previous reports [160, 161]. Subsequently, at 632 nm the refractive index of the a-MoO_3 is calculated to be 2.086, and this is in good agreement with the refractive index of the amorphous MoO_3 reported in the literature [162].

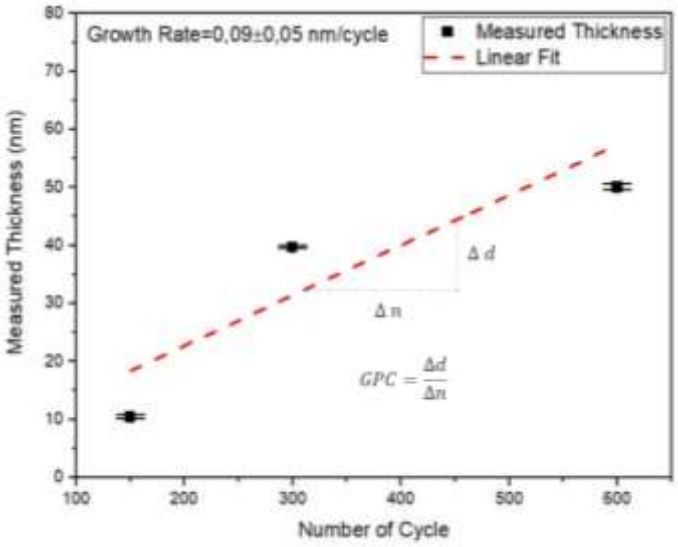

Figure 4.1. *MoO_3 thin film thickness as function of ALD number of cycles*

There are three phases of MoO_3, namely: monoclinic β-MoO_3, orthorhombic α-MoO_3, and hexagonal h-MoO_3. The latter has been obtained only by hydrothermal method [163]. It is mentioned that MoO_3 transition to β-MoO_3 starts at 355 °C and to α-MoO_3 438 °C up until melting point at ~729°C [164]. Therefore, each of the as-deposited MoO_3 (a-MoO_3) samples are annealed at 400 °C and 600 °C to obtain β-MoO_3 and α-MoO_3 respectively. Each of the as deposited and annealed samples is inspected under optical microscope (Nikon Eclipse, LV100NDA). However, each of the optical images (brightfield and darkfield) of the a-MoO_3 samples shows only a single color. Nevertheless, the optical images of the annealed a-MoO_3 (50-cycle and above) reveals readily visible grains as shown in Figure 3.2a-f. On the contrary, the optical images of the annealed a-MoO_3 samples (< 50-cycle) do not reveal any visible grains. This shows that, in addition to the SE revelation that the films are not continuous, and that there is sublimation of some of the nanoparticles of these samples during thermal annealing. The aim of the annealing of the a-MoO_3 is partly to gain insight about the final MoO_3 before sulfurization/CVD of MoS_2, and this final MoO_3 grains structures can be observed after annealing at 600 °C.

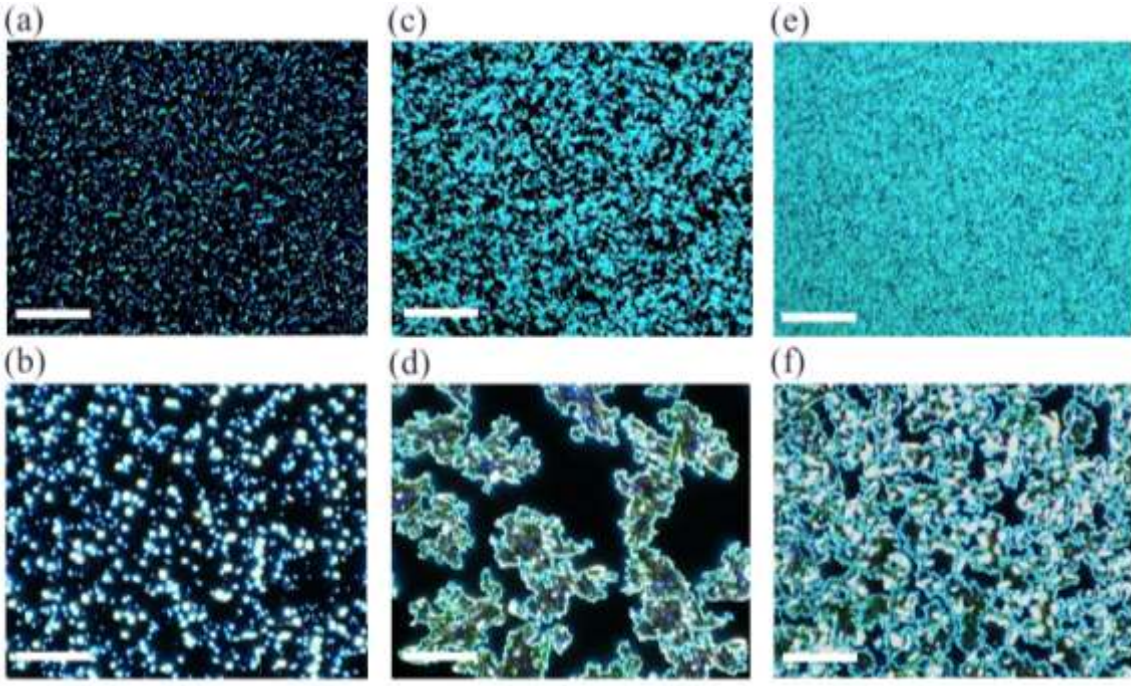

Figure 4.2. *Dark field optical images of the a-MoO_3 annealed at 400 °C and 600 °C respectively (a-b) 150-cycle (c-d) 300-cycle (e-f) 600-cycle. Scale bar 30 µm (Demirtaş et al., 2020)*

To have better understanding of the crystallinity of the a-MoO_3 samples and phase transition in the annealed samples, µRaman spectroscopy is carried out. From all as-grown samples, there is no peak observed except for the strong signals of Si (at 520 cm^{-1}) and SiO_2 (between 940-990 cm^{-1}). This further confirms that the as-grown MoO_3 film is amorphous, in agreement with [149]. However, the Raman signal is observed in the 400 °C annealed samples at 351 cm^{-1}, 775 cm^{-1}, 849 cm^{-1}, and 901 cm^{-1} which are reported to be for β-MoO_3 [163]. Similarly, from samples annealed at 600°C, Raman peaks are observed at 115, 157, 245 cm^{-1}, 285 cm^{-1}, 337 cm^{-1}, 667 cm^{-1}, 818 cm^{-1} and 995 cm^{-1}. Some of these peaks (667 cm^{-1}, , 818 cm^{-1} and 995 cm^{-1}) are reported to be Raman modes of α-MoO_3 [163, 165]. Raman spectra of 600-cycle MoO_3 thin film annealed at 400 and 600 are shown in figure 4.3a, and phonon mode of each peak is summarized in table 4.1.

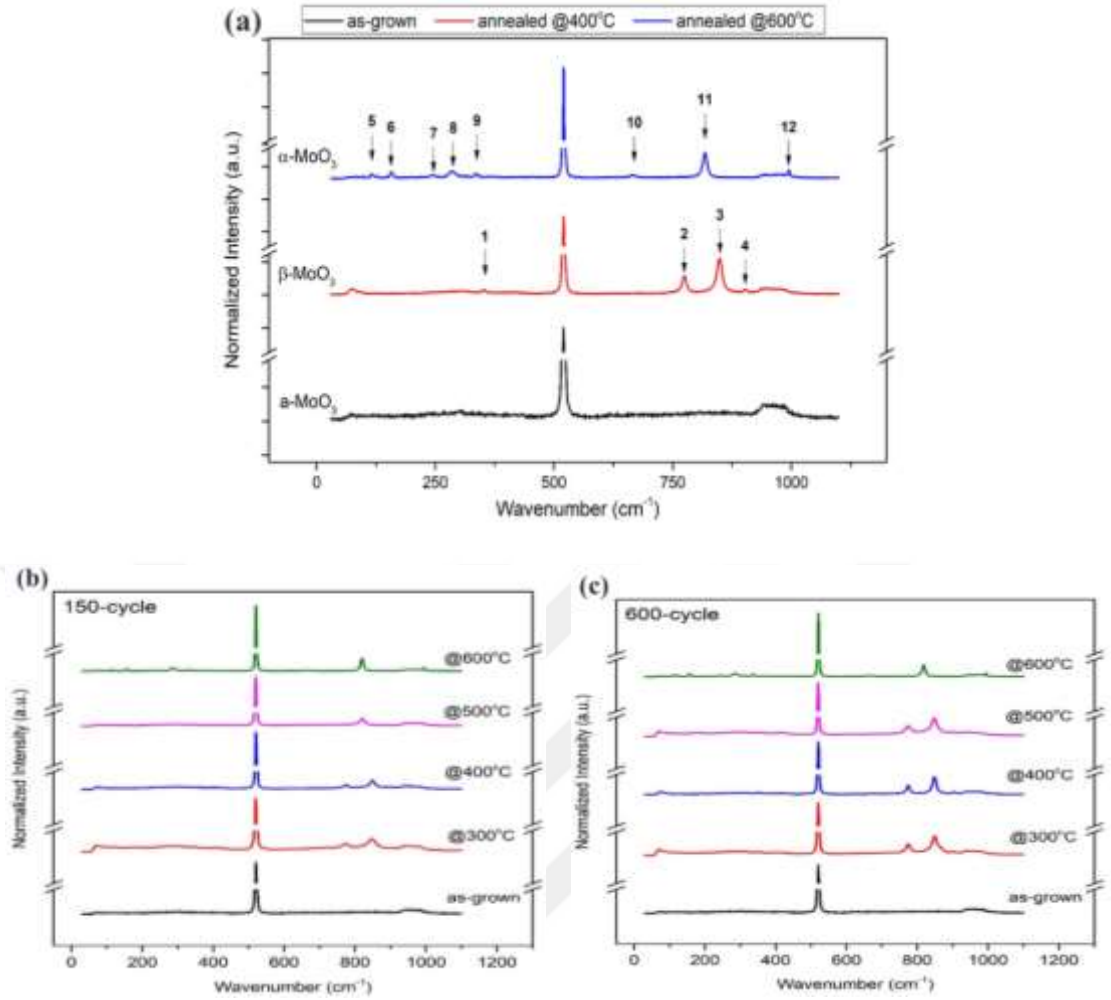

Figure 4.3. *Raman vibrational modes (a) 600-cycle a-MoO_3, β-MoO_3 and α-MoO_3 film (b and c) 150- and 600-cycle MoO_3 phase transition respectively by thermal annealing from 300 °C to 600 °C (Demirtaş et al., 2020)*

To investigate, in detail, the phase transitions of the MoO_3 films, 150- and 600-cycle MoO_3 are annealed each at 300 °C, 400 °C, 500 °C, and 600 °C. The effects of this annealing experiment are captured in the Rama spectra that is shown in Figure 4.3b-c. We realize that for the 150-cycle, transition from a-phase to β-phase starts from 300 °C to 400 °C, and transition from β-phase to α-phase starts from 500 °C to 600 °C. On the other hand, β-phase transition temperature increased to 500 °C in the 600-cycle MoO_3. Therefore, we conclude that the β-phase transition temperature of the MoO_3 film depends on the number of cycles.

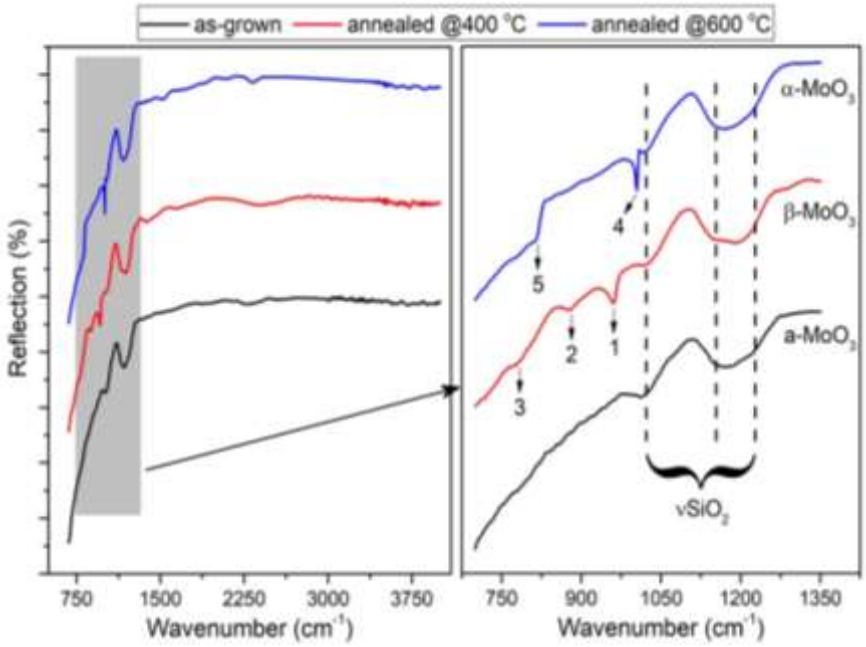

Figure 4.4. *ATR-FTIR spectra of the a-MoO_3, β-MoO_3 and α-MoO_3 film (Demirtaş et al., 2020)*

Since some of the vibrational modes of MoO_3 are infrared-active, the samples are further characterized using FTIR spectroscopy. Attenuated total reflection (ATR) FTIR mode is used because it provides high quality data about the samples' reflection in the mid-IR (650-4000 cm^{-1}). Figure 4.4 shows the IR spectra of the as-grown, β- and α-MoO_3. Signal peaks between 750 cm^{-1} and 1050 cm^{-1} are observed for all the samples. For β-MoO_3, the peaks at 960 cm^{-1} and 875 cm^{-1} are the characteristic peaks of molybdenum-oxygen symmetric stretching (Mo=O) vibrations. The vibrational frequencies between 770 cm^{-1} and 800 cm^{-1} correspond to the Mo-O-Mo asymmetric stretching vibrations. However, for the α-MoO_3, a strong and broaden band appeared at 1004 cm^{-1} and 815 cm^{-1} that are attributed to the terminal oxygen symmetric stretching of Mo=O, and these are the indicators of the layered structure and stretching of oxygen in Mo-O-Mo bonds. When the annealing temperature increased to 600 °C, all the vibrational peaks change remarkably and shifted to higher wavenumbers: The Mo=O is shifted from 960 cm^{-1} to 1004 cm^{-1} and became sharper. The Mo-O-Mo band became clearer and shifted from the 770-800 cm^{-1} to 875 cm^{-1}. Details of the ATR-FTIR vibrational modes are identified and summarized in Table 4.1.

Table 4.1. *μRaman and ATR-FTIR vibrational modes of β- and α-MoO_3 (Demirtaş et al., 2020)*

Method	Phase	Peak	Vibration Mode Detail	Wavenumber (cm^{-1})	Ref.
μRaman	β-MoO_3	1	O-Mo-O symmetric bending	350	[166]
		2	corner-sharing octahedra stretching	775	[167, 168]
		3	Mo-O symmetric stretching	849	[166, 168]
		4	corner-sharing octahedra stretching	901	[166, 168]
	α-MoO_3	5	MoO_4 chain mode	115	[166, 168, 169]
		6	MoO_4 chain mode	157	[167, 168, 170]
		7	O=M=O twisting, scissor	245	[167, 168, 170]
		8	O=M=O wagging	285	[167, 168, 170]
		9	O–M–O bending	337	[167, 168, 170]
		10	Mo-O=Mo stretching	667	[167, 168, 170]
		11	Mo–O–Mo stretching	818	[167, 168, 170]
		12	Mo=O stretching	995	[163, 166, 168, 170]
ATR-FTIR	β-MoO_3	1	Mo-O-Mo stretching	770-800	[171]
		2	Mo=O stretching	875	[169, 172]
		3	Mo=O asymmetric stretching	960	[173]
	α-MoO_3	4	Mo-O-Mo stretching	815	[169, 171]
		5	Mo=O stretching	1004	[169, 171]

To understand the thickness and space between the MoO_3 grains after annealing, AFM measurement of the samples is carried out. On each AFM image of the as-MoO_3 and annealed samples (i.e. < 50-cycle), there is not any visible grain therefore, the grains thickness and inter-grain spacing cannot be determined. Nevertheless, table 4.2 illustrates that the root mean square (RMS) of each of these MoO_3 samples is ~ 1 nm [53], and this can be regarded as an additional indication that the a-MoO_3 film is not continuous and that substantial amount of MoO_3 is sublimated during the thermal annealing. However, the < 50-cycle MoO_3 film and grains can be observed by using SEM or high-resolution AFM.

Table 4.2. *Height and grain size of the 50-, 150-, and 600-cycle MoO_3 film annealed at 400°C and 600°C (Demirtaş et al., 2020)*

No. of Cycle	As-grown	400°C Annealed		600°C Annealed	
	RMS (nm)	RMS (nm)	Grain Size (μm)	RMS (nm)	Grain Size (μm)
1-25	1-1.6	0.9-1	-	0.8-1	-
50	0.52	5.51	0.60 – 2.30	2.39	0.10 – 0.50
150	0.68	14.89	0.20 – 3.20	**21.28**	**1.00 – 6.00**
300	1.25	3.37	0.50 – 3.00	35.09	2.00 – 22.0
600	0.74	1.49	0.32 – 5.50	17.38	8.20 – 52.3

Figure 4.5 shows the AFM images and line profiles of the 150-cycle a-MoO_3 annealed at 400 °C and 600 °C. The line profiles show that the MoO_3 grains are sparsely distributed compared to the 300 and 600 cycled a-MoO_3. The 150-cycle inter-grain distance and height/thickness increases with increase in temperature: grain size 1.70 - 3.50 μm and height (RMS) 14.89 nm - 21.28 nm after annealing from 400 °C to 600 °C respectively. An increase in the grain size and height is observed in the 300- and 600-cycle MoO_3 after annealing from 400 °C to 600 °C as illustrated in the table above. However, by comparing the 150-, 300- and 600-cycle grain size and height, the 150-cycle samples exhibited moderate grain size and height.

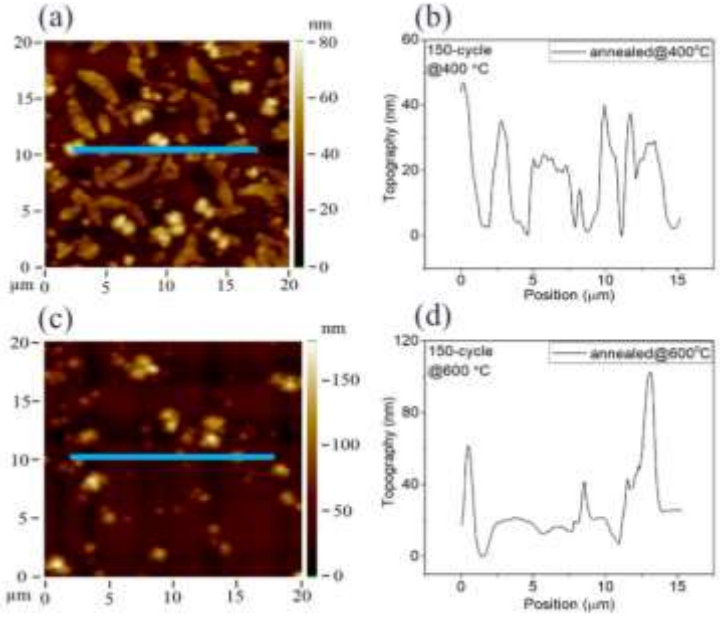

Figure 4.5. *2D AFM images and line profiles of the 150-cycle MoO_3 film annealed at 400°C and 600°C (Demirtaş et al., 2020)*

4.3 Growth and Characterization of 2D MoS_2 by CVD Using MoO_3 Film

4.3.1 Sulfurization/CVD growth procedure

The MoO_3 films, grown by PEALD, are used as the Mo precursor in the to synthesize MoS_2, instead of the MoO_3 powder used in the conventional CVD methods. For the CVD process, 150 mg of Sulfur power (99.95 %) is put in a quartz boat and placed at 1.5 cm with respect to the MoO_3 film as shown in the Figure 4.6. The CVD experiment is performed under 740 torr pressure with 100 sccm N_2 flow. Growth temperature of 690 °C ramped at a rate of 11.5 °C/minute is used. When the growth temperature is reached, the furnace is pulled upstream for a 4 minutes duration in order to bring S into the heat zones. This experiment is repeated by using the same parameters and growth configuration while changing only the MoO_3 film with different number of PEALD cycle.

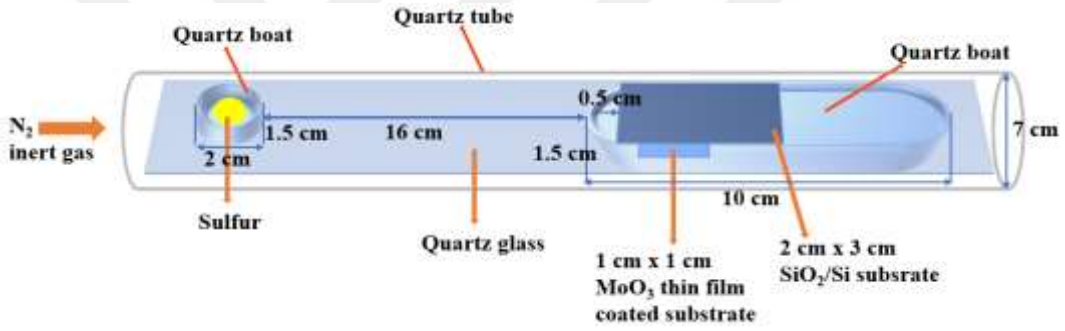

Figure 4.6. *Growth configuration used the CVD experiment of 2D MoS_2 using MoO_3 films grown by PEALD (Demirtaş et al., 2020)*

4.3.2 µRaman, PL and AFM analysis

During the MoS_2 experiment there are two growth processes occurring simultaneously: sulfurization and CVD. The former occurs on the bottom substrate while the latter occurs on the upper substrate. The CVD growth of MoS_2 on the upper substrate is as a result of the reactions of the MoO_x (trapped by the substrate) with the sulfur vapor. After each sulfurization/CVD growth, both the bottom and upper substrates are examined under the optical microscope. On both the top and the bottom substrates, identical MoS_2 flakes or grains size and distribution are observed, and we call this the "mirror effect". Because of this, only the optical images of the MoS_2 that is grown on the upper substrates are shown in Figure 4.6. As shown in the figure, by using 1-cycle > MoO_3 film ≤ 50-cycles, MoS_2 flakes, with edge lengths less than or equal to 1 µm, are observed. In these

experiments, flakes density is found to depend on the number of the MoO_3 cycles. Triangular MoS_2 flakes emerged when the MoO_3 with 150-cycle and above are used, and in each of the experiments mirror effect is observed. However, flake size and distribution are different when compared to those that are obtained using ≤ 50-cycle MoO_3 films, as shown in Figure 4.7. For instance, the MoS_2 flakes that are grown using the 600-cycle MoO_3 film are found to have the highest flakes density and at some areas, the flakes overlap to form discontinuous film. The flakes density reduces when the 300-cycle MoO_3 film is used. Subsequently, MoS_2 flakes with the optimum density and size (maximum edge length of ~40 μm) are grown when the 150-cycle MoO_3 film is used [174]. These results are summarized in the Table 4.3.

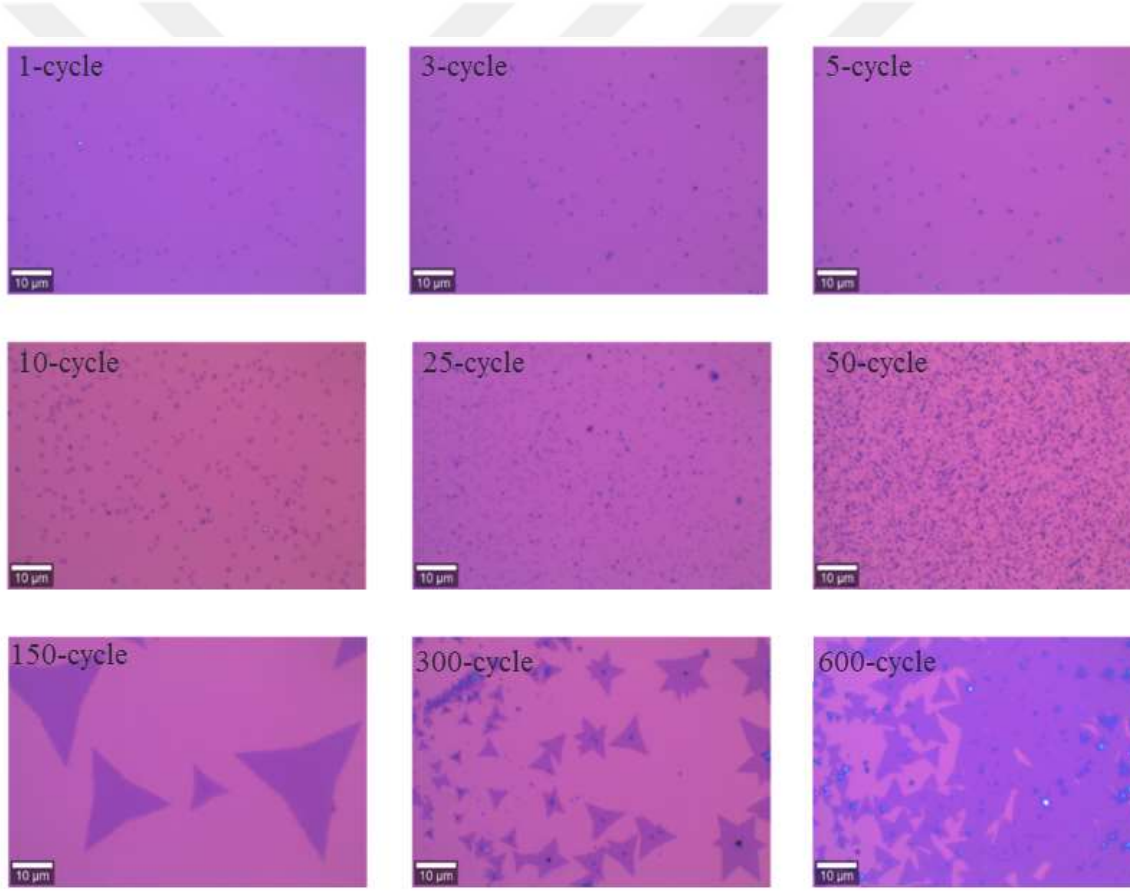

Figure 4.7. *Optical images MoS_2 grown by varying the number of MoO_3 ALD-cycle on the upper substrates*

As reported in literature [101, 151], by varying the amount of the MoO_3 precursor, TMDs flakes density, size, number of layers, and morphology appear differently. By using the optimum amount of MoO_3 film, a moderate nucleation density (which can result

in TMDs flakes with large size and sparse density) can be obtained. In this context, the MoO_3 films that are used in our experiments have different ALD cycles. Since the number of ALD-cycles is proportional to the amount of the MoO_3, the nucleation structure that each MoO_3 exhibits during the MoS_2 growth process will be different. 150-cycle MoO_3 film results in the growth of MoS_2 flakes with the optimum size and density possibly due to the moderate nucleation during the CVD process, as observed in the section 3.2.

Table 4.3. *ALD assisted CVD growth of MoS_2 result summary (Demirtaş et al., 2020)*

PEALD cycle	MoS_2 Structure				Remark
	Layer #		Flake Size (μm)		
	Bottom Substrate	Upper Substrate	Bottom Substrate	Upper Substrate	
1-5	Mostly monolayer		< 1		Dot-like flakes
10-25	Mostly few layer				
50	Mostly monolayer		≤ 1		
150	All monolayer		≤ 40		Triangular flakes
300	Monolayer with few layers spot		≤ 19		Triangular flakes with few layer spot at the center
600	Mostly few layer		≤ 7		Triangular flakes and discontinous film formation

Each of the as-grown MoS_2 on both the upper and lower substrates are characterized by μRaman, AFM and PL. Accordingly, the results are summarized in the Table 4.3. In the Figure 4.8, the AFM image, PL and μRaman spectra of the MoS_2 flakes that are grown using 150-cycle MoO_3 film are presented. The MoS_2 flakes thickness, as confirmed by the AFM (Figure 4.8a-b), is found to be 0.78 nm [175]. After the μRaman characterization (Figure 4.8c), the A_{1g} and E^1_{2g} vibrational modes of the MoS_2 flakes are found to be 404.26 cm^{-1} and 383.95 cm^{-1} respectively, with the difference of 20.31 cm^{-1}. These values are comparable to those reported in the literature as shown in the Table 2.1. Furthermore, the PL spectra of the MoS_2 (Figure 4.8d), as fitted with the Gaussian function, is found to exhibit three PL peaks at 635.76 nm, 679.37 nm and 685.27 nm. These peaks are equivalent to the B-exciton, A-exciton, and Trion (A^-), respectively as reported in the literature [98, 151, 176].

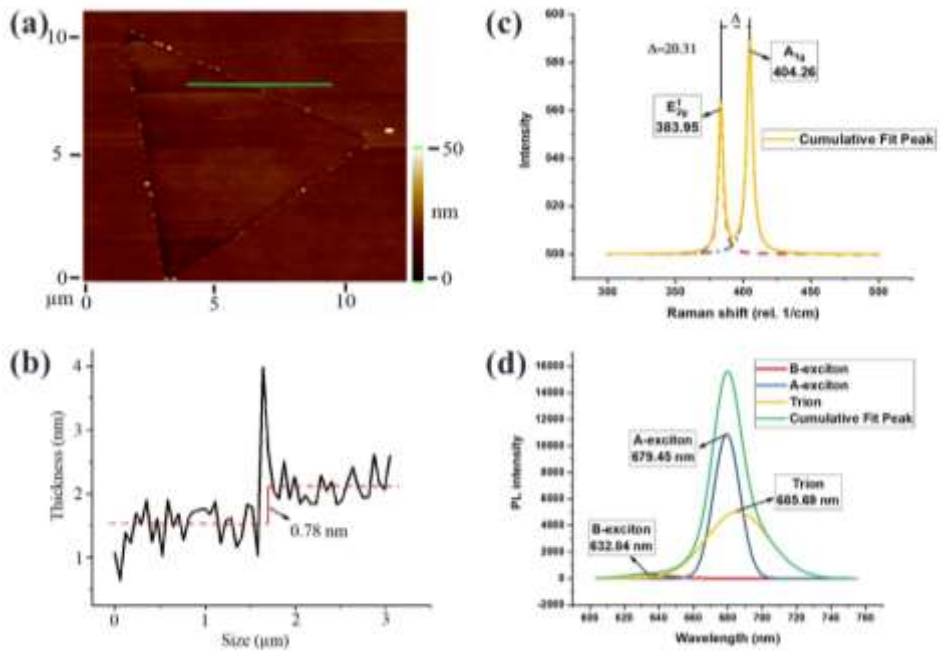

Figure 4.8. *MoS_2 flakes grown using 150-cycle MoO_3 thin film* ***(a)*** *μRaman spectra* ***(b)*** *2D AFM image* ***(c)*** *AFM line profile* ***(d)*** *PL spectra (Demirtaş et al., 2020)*

4.4 Conclusion

In summary, a new route to for the growth of monolayer MoS_2 with layer, size and distribution control is presented. This method combines the use of two most powerful vapor techniques namely, ALD and CVD. Instead of the conventional MoO_3 powder, MoO_3 films grown by ALD with different number of cycles are used. The MoO_3 films have been characterized by Raman, FTIR, AFM, and VASE. An optimized recipe that yields a MoS_2 flakes with lateral size of ~ 40μm is obtained by using the MoO_3 film with 150-cycle. The μRaman, PL and AFM analysis of the MoS_2 film is of high quality. This new route that is described herein provides a pathway to the growth of a high quality 2D MoS_2 with layer and size control with the potential for commercial scale production of optoelectronic devices.

5. CVD GROWTH AND CHARACTERIZATION OF MONOLAYER MoS_2 AND $MoSe_2$

5.1 Introduction

2D TMDs have received to receive immense research attention since 2011 when Radisavljevic *et al*. reported the high carrier mobility of mechanically exfoliated 2D MoS_2 [11]. A year after, the optoelectronic properties of 2D MoS_2 were reported by Yin *et al*. [12]. Due to scalability issues faced by the mechanical exfoliation method, researchers turned their attention to the used of CVD method to grow large area and uniformly distributed 2D TMDs [22, 117, 150]. These research endeavors are aimed at realizing the fundamental goal of the growth of high-quality 2D TMDs in commercial scale for the future electronic and optoelectronic devices. To reach this fundamental goal, one of the most recently proposed methods to achieve the large area and uniform 2D TMDs is by using glass substrates.

Using CVD technique, Chen et al. successfully grew up to 2.2 mm large $MoSe_2$ on the glass substrates [25]. In their report, they indicate that the surface of a solid substrate (such as SiO_2/Si) is rough, and nucleation centers are formed preferably at the rough sites, causing high nucleation density. Therefore, with uniform surface, nucleation density can be suppressed, and this uniformity can be achieved in a molten glass substrate. However, Yang et al. attributed the large-area growth on the catalytic effect of the Na^+ ions that are present in the glass substrate. Glass substrates, except the quartz and borate glass, contain substantial amount of the N^+ ion especially soda lime glass with ~17% composition of Na_2O. Even though there are other compounds in glass, only the Na^+ ion activity has been observed during the CVD growth. Alternatively, the borate or quartz glass can be coated with a NaCl solution for the CVD growth of 2D TMDs to compensate for its Na^+ ion deficiencies [29]. Herein, CVD growth of a large area uniform 2D MoS_2 and $MoSe_2$ on glass substrates are presented. The $MoSe_2$ is grown on SiO2/Si substrates that are coated by the NaCl solution.

5.2 CVD Growth Procedure of MoS_2 and $MoSe_2$

In this section, experimental procedure for the growth of monolayer MoS_2 and $MoSe_2$ is presented. To grow $MoSe_2$, the NaCl-assisted CVD growth method is used as reported in the literature [29]. A 4 x 4 cm^2 SiO_2/Si is coated with a NaCl (99.95%) solution that is prepared using 2 mg of NaCl dissolved in 5ml of DI water. The SiO_2/Si substrate is coated with the NaCl solution with a spin coating recipe that is shown in the Table 5.1.

Before the spin coating, the solution is allowed to rest on the substrate for at least 1 minute to enable the NaCl particles to settle on the substrate. The spin coating recipe comprised of 4 steps which include dispense, spread, edge bread removal (EBR) and drying as outlined in Table 5.1. Subsequently, the substrates are annealed on a hot plate for 2 minutes at 70 °C.

Table 5.1. *Recipe used to coat SiO_2/Si with NaCl solution*

	Dispense	**Spread**	**EBR**	**Dry**
Spin speed (rpm)	5200	10000	500	4000
Spin acceleration (rpm/s)	1000	100	1000	1000
Spin time (s)	50	20	10	20

Figure 5.1 shows the growth configuration adopted to grow monolayer MoS_2 and $MoSe_2$ using MoO_3 (99.95%) and S/Se (99.99) solid precursors. The glass substrates used for the growth of monolayer MoS_2 are the well-known microscope coverslips that have the Na^+ ions concentration of up to 6.4 % [177]. The glasses are arranged and labelled as S1-S4 (where S stands for sample). The precursors are placed in a strategic position that have different temperature. The growth process is controlled by using the split furnace movable heaters. The parameters used for the growth of MoS_2 and $MOSe_2$ are different. Therefore, the recipes used for the growth of each of the materials are summarized in Table 5.1 for comparison. In the table, only the optimized recipe of MoS_2 is shown.

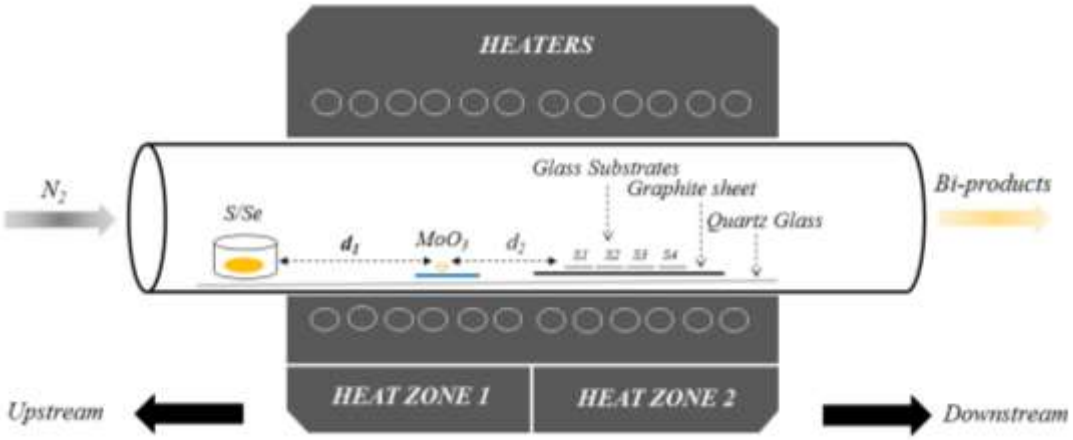

Figure 5.1. *Monolayer MoS_2 and $MoSe_2$ Growth Configuration*

During the CVD growth $MoSe_2$, H_2 is used as a reducing agent of the MoO_3 precursor. The H_2 and Ar gases are introduced at the same time and at the beginning of the experiment. The growth configuration of this experiment is identical to that which is shown in Figure 5.1 except that here only one sample is used.

Table 5.2. *The recipes used for the CVD growth of monolayer MoS_2 and $MoSe_2$*

	MoS_2	**$MoSe_2$**
Substrate	*Glass*	*SiO_2/Si*
Temperature (°C)	750	850
Pressure (torr)	740	750
MoO_3 powder (mg)	0.3	0.1
S/Se powder (mg)	300	500
Carrier Gas (sccm)	N_2 (250)	Ar (80)/H_2 (20)
d_1 (cm)	11	6
d_2 (cm)	3	2
Growth Time (min)	5	15
Ramp Rate (°C/min)	12.5	21.25

5.3 µRaman, PL, and AFM Analysis of Monolayer MoS_2

By using the optimized recipe, MoS_2 with different flakes sizes are grown on the substrates. MoS_2 with the largest flake sizes is obtained on the first substrate as shown in the appendix 1. Figure 5.2a-c shows the bright field and dark field optical images of the MoS_2 flakes on substrate number 4 obtained using the optimized recipe. The size of the MoS_2 flakes is between 30 – 40 µm. Figure 5.2b-c shows the bright field and optical images of the MoS_2 flakes that are transferred to the SiO_2/Si substrate using the procedure stated in the section 3.2 of this report. The dark field optical image reveals very sharp grain boundaries of the MoS_2 triangles and the absence of any seed structure in the middle of the triangles. These are some of the indications of the quality of the MoS_2 flakes and accuracy of transfer procedure.

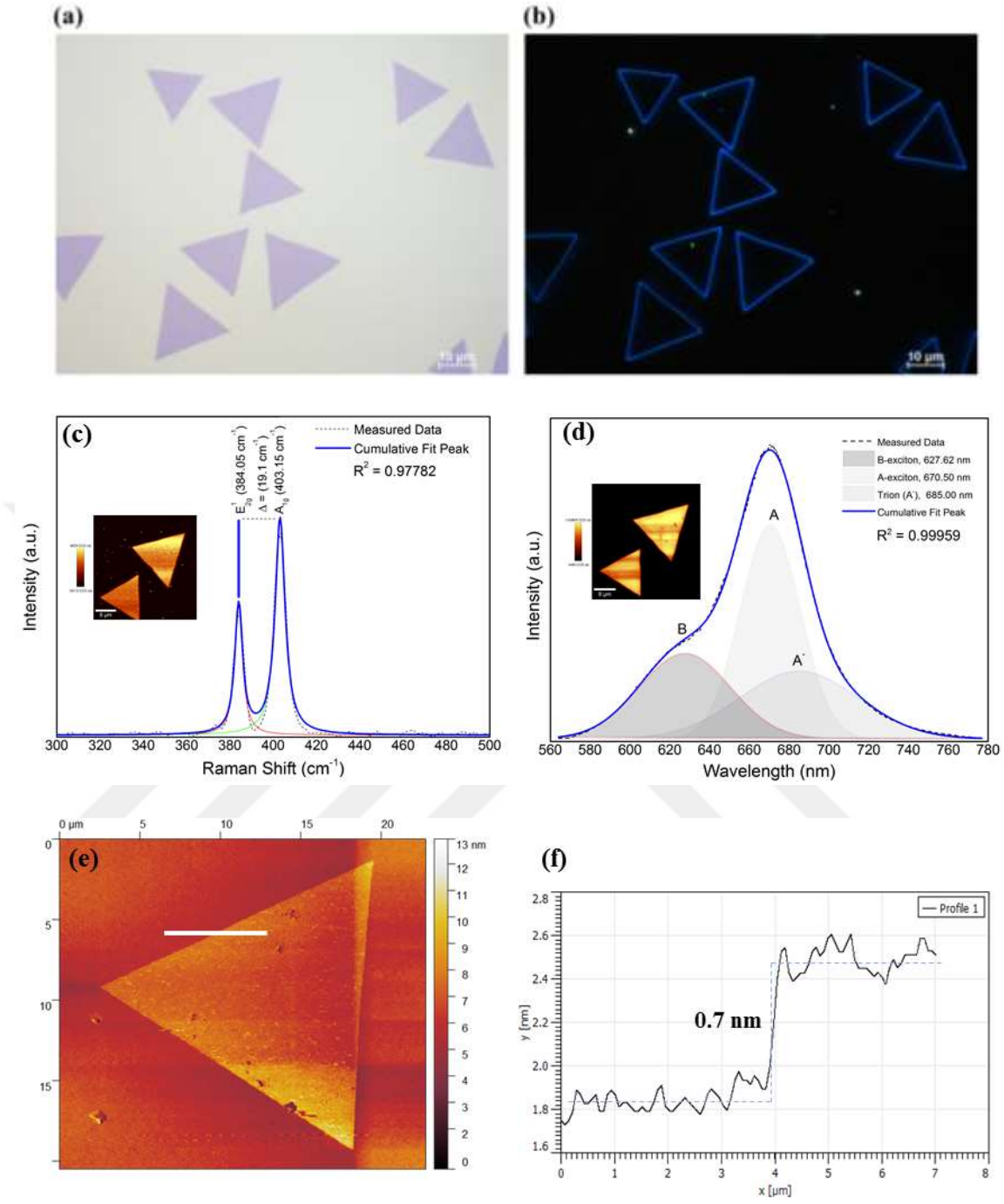

Figure 5.2. *Characterization of the MoS_2 (a-b) bright field and dark field optical images (c) Raman spectra and Raman map in the inset (d) PL spectra and PL map in the inset (e-f) 2D AFM image and its line profile*

Figure 5.2c-f shows the µRaman, PL, and AFM characterization results of the monolayer MoS_2 flakes. For the Raman characterization, image scan of the MoS_2 flakes is taken as shown in the inset of figure 5.2c. After inspection of the scanned area of the flakes, the two vibrational Raman peaks, E^1_{2g} and A_{1g} of the MoS_2, are found to be 384.1 ± 0.5 cm^{-1} and 400.2 ± 0.2 cm^{-1} respectively. The Raman spectrum of Figure 5.3a for a

single point in the scanned area shows that the difference between the two peaks of the MoS_2 is 19.1 cm^{-1} [29]. For the PL measurement of the MoS_2 flakes, image scan is taken over the same area with the Raman as shown in the inset of Figure 5.2d. After inspection of the scanned area, it is observed that the PL peak center varies slightly between 670.0 nm and 677.0 nm respectively and each of these PL peaks agrees with the literature as shown in Table 2.1. Moreover, a single point PL spectrum of the MoS_2 from the scanned area is extracted and fitted with the Gaussian function. After the fitting, the A exciton, B exciton, and Trion (A^-) PL peaks are found to be 670.6 nm, 627.6 nm, and 685.0 nm [65]. The Raman and PL image scans both show the non-uniform intensity of the MoS_2 flakes. This together with the variation in the PL and Raman peaks may be related to the compositional difference that is observed in flakes of a monolayer TMDs [65, 66]. The MoS_2 flakes are characterized further by the AFM. As shown in the Figure 5.2e-f, the thickness of the MoS_2 flake is 0.7 nm.

5.4 μRaman, PL, and AFM analysis of monolayer $MoSe_2$

Figure 5.3a-b shows the optical images of the $MoSe_2$. The size of the $MoSe_2$ flakes is around 5 - 50 μm. The dark field optical image shows a clear grain boundary of the $MoSe_2$ flakes; at the center of some of the flakes, the growth of $MoSe_2$ flakes that have a size within a nanometer range is observed. Also, at the middle of some of the flakes, seed structures are observed, and these are expected to be the origin of the $MoSe_2$ flakes growth. Figure 5.3c-f shows the μRaman, PL and AFM characterization results of the $MoSe_2$ flakes. For the Raman, image scan of the $MoSe_2$ flakes is taken as shown in the inset of Figure 5.3c. After the inspection of the scanned area and fitting each of the spectra with the Lorentz model, the out-of-plane Raman peak (A_{1g}) of the $MoSe_2$ is found to be 240.0 ± 0.7 cm^{-1}. Moreover, the E_{1g} and E^1_{2g} modes of $MoSe_2$ are also found to be 144.4 ± 0.9 cm^{-1} and 285.8 ± 1.1 cm^{-1} respectively agreeing with previous studies [25, 178-180]. For the PL characterization, a single point measurement is taken from four different locations on the $MoSe_2$ flakes (Figure 5.3d). After fitting the spectra with the Gaussian model, the cumulative PL peak of the $MoSe_2$ is found to be centered at 818.4 nm. The A exciton, B exciton, and A^- are also fitted at 722.6 nm, 818.4 nm, and 827.9 nm respectively in close agreement with [19, 69]. The $MoSe_2$ are further characterized by AFM to find the thickness of the flakes as shown in Figure 5.3e-f. The thickness of the $MoSe_2$ flake is found to be 0.98 nm and this is consistent with the literature [25].

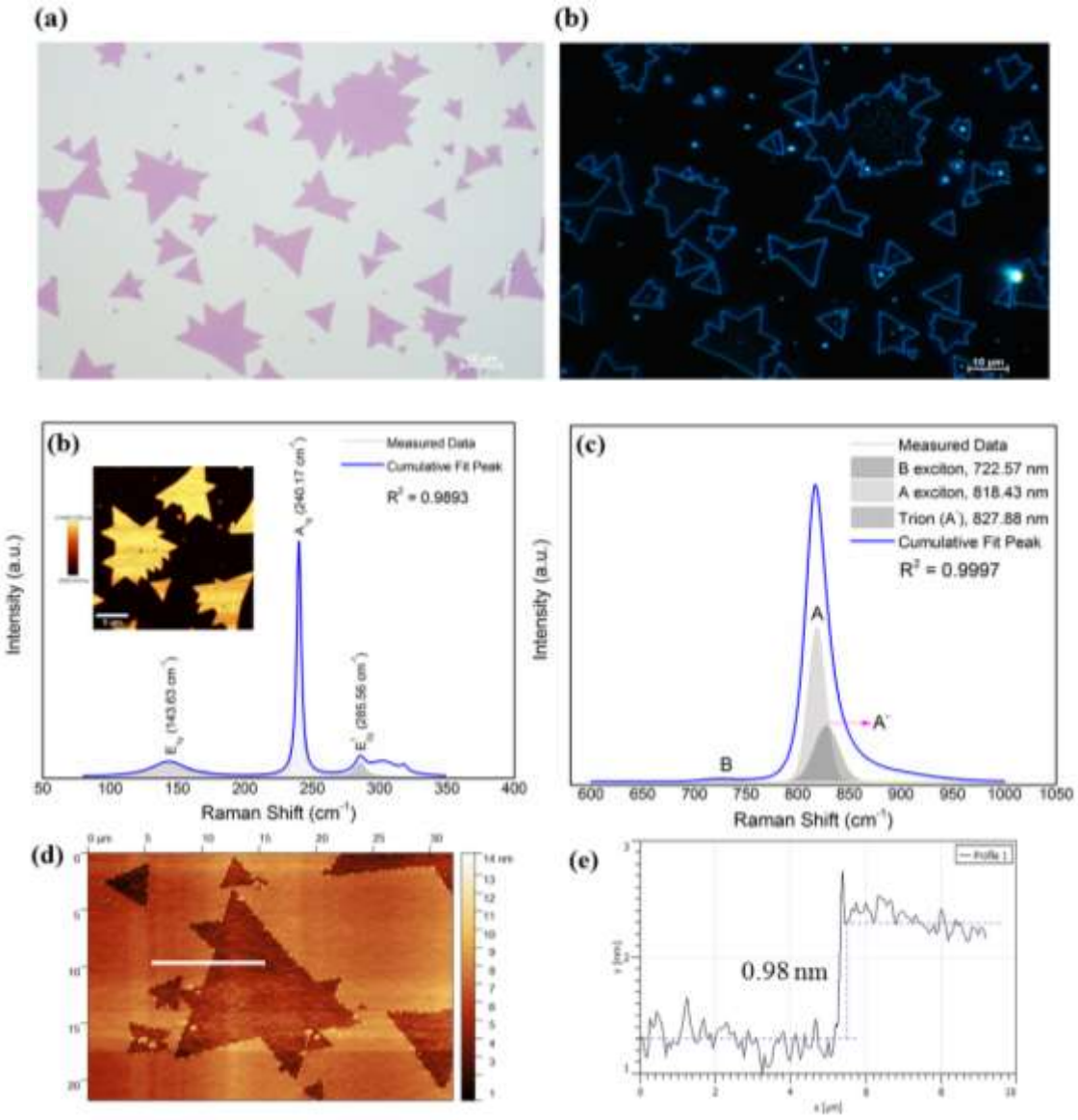

Figure 5.3. *Monolayer $MoSe_2$ grown by NaCl-assisted CVD method (a-b) bright and dark field optical images (c) Raman spectrum with Raman map in the inset (d) PL spectrum (e-f) 2D AFM image and line profile*

5.5 Conclusion

Monolayer MoS_2 is grown on a glass substrate, and due to the presence of the Na^+ ions on the substrate, a MoS_2 with a lateral size of up to 500 μm has been achieved. For practical optoelectronic applications, the MoS_2 grown on the glass substrate can be transferred to any target substrate using etching-free transfer technique. A nonhomogeneous PL and Raman intensity is observed in the MoS_2 flakes and is attributed to the compositional differences in the flakes. Monolayer $MoSe_2$ is grown on SiO_2/Si substrate coated with NaCl solution to harness the catalytic effect of the N^+ ions in the

growth of large area $MoSe_2$. By this method, a $MoSe_2$ fakes with up to 50 μm lateral size are grown. The quality of the monolayer MoS_2 and $MoSe_2$ is ascertained by μRaman, PL, and AFM analysis. These study reveals that CVD technique is rather scalable in growing large area 2D TMD materials to be used in commercial scale production of optoelectronic devices.

6. $MoS_2/MoSe_2$ HETERO BILAYER SYSTEM

6.1 Introduction

2D layered materials have been regarded as promising semiconductors for future electronic and optoelectronic devices. One of the factors that contributes to the growing interest of the 2D systems is the possibility of using them to form heterostructures that enable the fabrication of optoelectronic devices with greater functionalities. The recent progress in the scalable growth of the 2D TMDs by CVD has open the new possibility to envisage the formation of unprecedented solids by way of stacking layers of different 2D materials vertically. Fundamentally, such a stacked heterostructure is different because in the interface, only the weak van der Walls interaction exist. The preparation of the a heterointerface that is of high quality can be easily achieved without necessarily fulfilling the atomic commensurability [20, 21]. It should be noted that the optical properties of 2D materials change with respect to the van der Waals interaction between the layers in the heterostructure. These changes are more pronounced in the heterostructures based on 2D TMDs. For instance, Kim *et al.* reported that the absorption of the $MoSe_2/MoS_2$ hetero bilayer surpass that of the individual monolayers by a factor of two [18]. With an optimum interlayer distance, it is possible to retain the direct band gap of the individual monolayers of the hetero bilayer [18-21]. Herein, $MoS_2/MoSe_2$ hetero bilayer is fabricated. The hetero bilayer system is achieved by transferring the MoS_2 flakes to those of the $MoSe_2$, as illustrated in the section 3.2.

6.2 µRaman, PL, and AFM Analysis of the $MoS_2/MoSe_2$ Hetero Bilayer System

Figure 6.1a-b shows the optical images of the $MoS_2/MoSe_2$ hetero bilayer system. The region of interest is demarcated with a dashed-line rectangle. Even though the transfer procedure adopted in this study is non-deterministic, the chances of the MoS_2 flakes coinciding with that $MoSe_2$ is high since the flakes of both the MoS_2 and $MoSe_2$ are comparable size and distribution. The dark field optical image of the hetero bilayer shows the sharp grain boundaries of the individual 2D system in the hetero bilayer. In the hetero bilayer region, shiny spots are noted, and these may be due to defects or the nanometer scale flakes of the $MoSe_2$ noted in the previous section. Henceforth, isolated MoS_2 or $MoSe_2$ will be used as a nomenclature referring to the 2D MoS_2 and $MoSe_2$ that does not participate in the hetero bilayer system. The hetero bilayer system is first characterized by AFM, after annealing the sample, to find its thickness. The AFM measurement is also aimed at determining the interlayer distance of the hetero bilayer

system. Figure 6.1c-d shows the characterization result by AFM. The line profile of the AFM measurement shows that the thickness of the MoS_2 only part of the hetero bilayer is 0.95 nm. This may account for the interlayer distance which – even in the $MoS_2/MoSe_2$ hetero bilayer system grown by two-step CVD method – is reported by Carozo *et al.* to be around 0.1 nm [99].

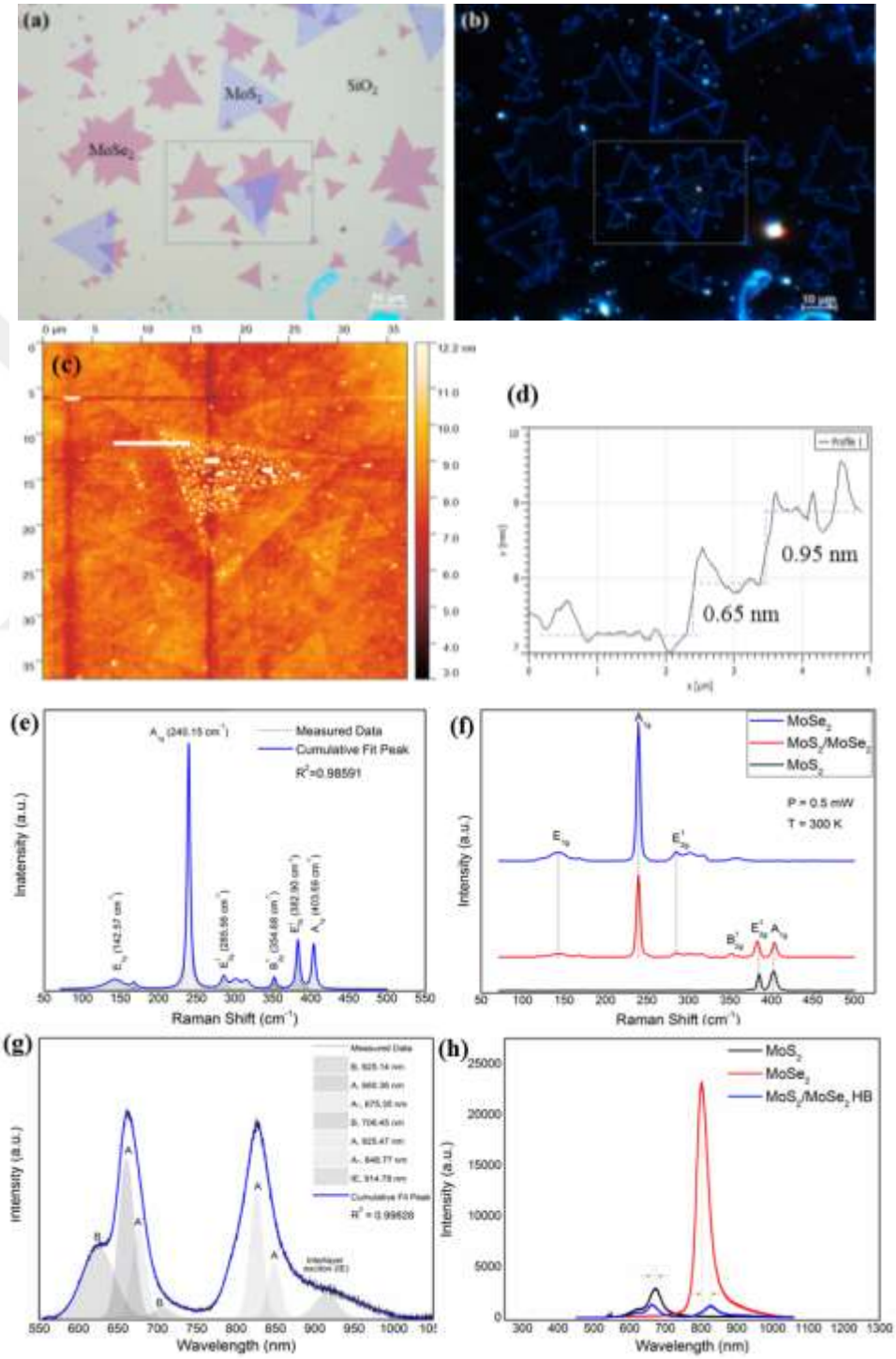

Figure 6.1. *Characterization of the $MoS_2/MoSe_2$ hetero bilayer system (a-b) bright Dark field optical images (c-d) 2D AFM image and line profile (e) fitted Raman spectra (f) Raman spectra of in*

comparison with those of the isolated monolayer components (g) fitted PL spectra (h) PL spectra in comparison with those of the isolated monolayer components

The hetero bilayer system is further characterized using μRaman spectroscopy. The Raman vibrational modes of the isolated monolayer are also probed. Figure 6.1e-f shows the Raman vibrational modes of the hetero bilayer as fitted with the Lorentz model. In addition to the vibrational modes of the 2D MoS_2 and $MoSe_2$, the appearance of a new peak at 354.7 cm^{-1} is noticed both before and after thermal annealing of the hetero bilayer. As per the literature, the peak is the vibrational mode of $MoSe_2$ that is inactive in a monolayer but become active in a bilayer $MoSe_2$ [70] or hetero bilayer [69]. According to Tonndorf *et al,* this peak appears as a result of the breakdown of translation symmetry in a bilayer structure of $MoSe_2$ [70]. The Raman spectra of the hetero bilayer is compared with that of the isolated MoS_2 and $MoSe_2$ as shown in Figure 6.1f. There is not observable difference between the Raman peaks of the $MoSe_2$ in the hetero bilayer and $MoSe_2$ in the isolated regions. However, we observed shifting of the E^1_{2g} and A_{1g} modes of MoS_2 in the hetero bilayer region relative to those of the isolated MoS_2: it is observed that the E^1_{2g} peak red shifts by 1.8 cm^{-1} before annealing and 1.5 cm^{-1} after annealing. On the other hand, the A_{1g} mode blue shifts by 1.5 cm^{-1} before annealing and 1.0 cm^{-1} after annealing. As per the literature, the red shift of the E^1_{2g} peak indicates tensile strain while the blue shift of the A_{1g} peak indicates an enhanced electron-phonon interaction due to increased electron concentration [18].

The $MoS_2/MoSe_2$ is further characterized by PL spectroscopy as shown in Figure 6.1g-h. After fitting the PL spectra of the hetero bilayer system with the Gaussian function, the cumulative PL peaks of MoS_2 and $MoSe_2$ in the hetero bilayer are found to be 662.0 nm and 825.5 nm respectively. In addition, the PL of the hetero bilayer is further fitted with the A exciton, B exciton, and A^- trion. The PL peaks of the MoS_2 in the hetero bilayer that correspond to the B exciton, A exciton and A^- trion are fitted at 625.1 nm, 660.4 nm, and 675.4 nm respectively [65]. On the other hand, the PL peaks of the $MoSe_2$ in the hetero bilayer system are fitted at 706.5 nm, 825.5 nm, and 848.6 nm corresponding to the B exciton, A exciton, and A^- trion [18, 69]. In addition, a new peak is observed in the hetero bilayer system and is fitted at 914.8 nm. This PL emission perfectly agrees with the reported interlayer exciton that is formed due the type II band alignment leading to spatial separation of charge carriers [102].

Table 6.1. *Comparison of the PL peaks of the MoS_2 and $MoSe_2$ in the isolated region and hetero bilayer system. CP stands for cumulative peak and IE stands for interlayer exciton. The PL peaks are in nm unit.*

	MoS_2				**$MoSe_2$**				
	B	**A**	**A-**	**CP**	**B**	**A**	**A-**	**CP**	**IE**
Isolated	627.6	670.6	685.0	670.7	722.6	818.4	827.8	818.4	-
Hetero Bilayer	625.1	660.4	675.4	662.0	706.5	825.5	848.8	825.5	914.8

Figure 6.1h shows the PL spectra of the monolayer MoS_2 and $MoSe_2$ in the isolated region and hetero bilayer region for comparison. It is realized that the PL peak center of the MoS_2 in the hetero bilayer blue shifted by 25 meV and that of the $MoSe_2$ red shifted by 43 meV relative to those of the isolated MoS_2 and $MoSe_2$ respectively. Similar PL shifts are reported by Kin *et al.* and they attributed the shifts to the dielectric screening effect [18]. Furthermore, a strong quenching of the PL peaks of the hetero bilayer, compared to those of the isolated monolayers, is observed [13, 18-21, 69, 99, 100, 181]. This is reported to occur due to the indirect recombination of the electrons and holes in the hetero bilayer region [18, 20, 21, 69]. PL peaks of MoS_2 and $MoSe_2$ in the hetero bilayer and in the isolated region are compared in Table 6.1.

The PL quenching of the monolayer MoS_2 and $MoSe_2$ in the hetero bilayer system can be avoided by using a spacer to insulate the charge transfer between the layers. In the work of *Kim et al.*, it is reported that the charge transfer mechanism is the phenomenon responsible for both the quenching and the shifting of the PL peaks of the MoS_2 and $MoSe_2$ in the hetero bilayer system relative to those of the isolated region. To avoid this, they inserted hexagonal boron nitride (hBN) between the layers (MoS_2 and $MoSe_2$). Their results show that two layers of hBN can suppress the charge transfer mechanism; and this can lead to the retention of the direct bandgap of the monolayer materials and higher absorbance in the hetero bilayer system [18].

6.3 Temperature Dependent μRaman Analysis of $MoS_2/MoSe_2$ Hetero Bilayer System

6.3.1 Introduction

In recent years, heterostructure based on 2D TMD and other 2D system-based devices such as the boron nitride (BN) and graphene have become a hot topic. The 2D TMDs based heterostructure is particularly important because of the fascinating phenomena that include high photoluminescence quantum yield [102], the ultrafast charge transfer [20], strong light-matter interactions [182], excitonic processes [21, 69, 99], high light absorption and direct band gap in the heterostructure [18]. As a result, the 2D TMDs based heterostructures are being used for various optoelectronic devices especially photodetector and solar cells [38, 67, 96, 110, 115, 117, 183, 184]. Having an insight about the interfacial thermal resistance between the adjacent layers and thermal properties of the heterostructure materials is crucial for the operation of a variety of electronics and optoelectronic devices. Currently, heat dissipation is among the major constraints in the production of electronic and optoelectronic integrated circuits. Also, usage of TMD based devices under harsh conditions such as under very high and very low temperature ambient is still under investigation. Hence, for better design and fabrication of the electronic and optoelectronic devices based on TMD, to shed light on the interaction of two heterolayers at different temperatures is imperative.

Raman spectroscopy is a non-destructive technique that is regarded as a rather local, fast, and sensitive method for characterizing materials. Since the discovery of the Raman technique in 1928, it has been commonly used to study electronic and vibrational properties of material [185, 186]. Recently, Raman technique has been used to study the changes in the vibrational modes of TMDs with respect to the doping concentration [187], pressure [188], number of layers [189], and strain [190]. Furthermore, the technique has been used to study the changes in the Raman peaks and full width half maxima (FWHM) of the TMDs as a function of temperature. In most of the related literatures, a linear relationship between the Raman shift and temperature is observed. As a result, the Grüneisen model is commonly used to fit the Raman shifts due to the change in temperature [181, 188, 191-198].

$$\omega(T) = \omega_0 + \chi T \qquad (6.1)$$

where ω_0 is the room temperature vibrational mode, χ is the first order temperature coefficient, and T is the temperature.

Different χ values are reported for MoS_2 that is grown by different methods such as mechanical exfoliation (ME) [192, 194] and CVD [181, 191-193, 195] on different dielectric environment such as SiO_2/Si [181, 191-193, 195] and air (suspended) [194]. Table 6.2 provides a summary of the χ values reported in the literature. By looking at the table, one can observe a lot of disagreements with the reported χ values even for a monolayer MoS_2 grown using the same technique. For instance, while Lanzillo *et al.* reports that for a CVD grown monolayer MoS_2, the χ value of the A_{1g} vibrational mode is higher [191], the opposite is reported by Najmaei *et al.* [192] even though the temperature range they used is comparable. On the other hand, the FWHM broadening as a function of temperature is reported for both the E^1_{2g} and A_{1g} modes of MoS_2 [191]. Compared to MoS_2, changes in the Raman vibrational modes and FWHM of $MoSe_2$ are sparsely reported. As shown in Table 6.3, there is not any report on the χ values of the E^1_{2g} vibrational mode for a monolayer $MoSe_2$. The E^1_{2g} mode's χ value is reported only for a FL $MoSe_2$ that is prepared by chemical exfoliation. Also, throughout our investigation in the literature, we did not come across any report that shows how the FWHM of $MoSe_2$ changes with respect to temperature. To fill these gaps, herein, a comprehensive study of the changes in the peak position and FWHM of the Raman vibrational modes of monolayer MoS_2 and $MoSe_2$ are reported. The study is carried out for the monolayer MoS_2 and $MoSe_2$ both in the isolated and hetero bilayer regions. For each of these, the measurement is carried out before and after thermal annealing.

6.3.2 Experimental procedure

Temperature dependent μRaman spectroscopy is performed with LINKAM T95-PE temperature control system which is integrated with the WITec Alfa 300 Raman system shown in Figure 6.2a-b. The measurement is carried out using a long-working distance lens (NA = 0.55) providing a laser spot size of 0.62 μm. During the measurement, temperature is varied between 83 K and 483 K with a step of 50 K at a ramping rate of 150 °C per minute. Upon elevating from one temperature point to another, the system is allowed for at least 15 minutes of thermal stabilization [199]. Throughout, 0.5 mW laser power is used to avoid local heating of the sample which may cause shift in the Raman

peak [181, 199, 200]. During the measurement, especially at the low temperature, the chamber is frequently purged with N_2 gas to avoid oxidation of the material; also, constant purging of the interface, between the chamber and the objective with N_2, is maintained to avoid condensation of the water vapor which may cause poor Raman signal acquisition. Figure 6.2c shows the optical images of a hetero bilayer sample with the MoS_2 and $MoSe_2$ clearly observable both in the hetero and isolated regions. The optical images are taken at 83 K, 300 K, and 483 K as indicated in figure. The images are distinguishable by their contrast differences.

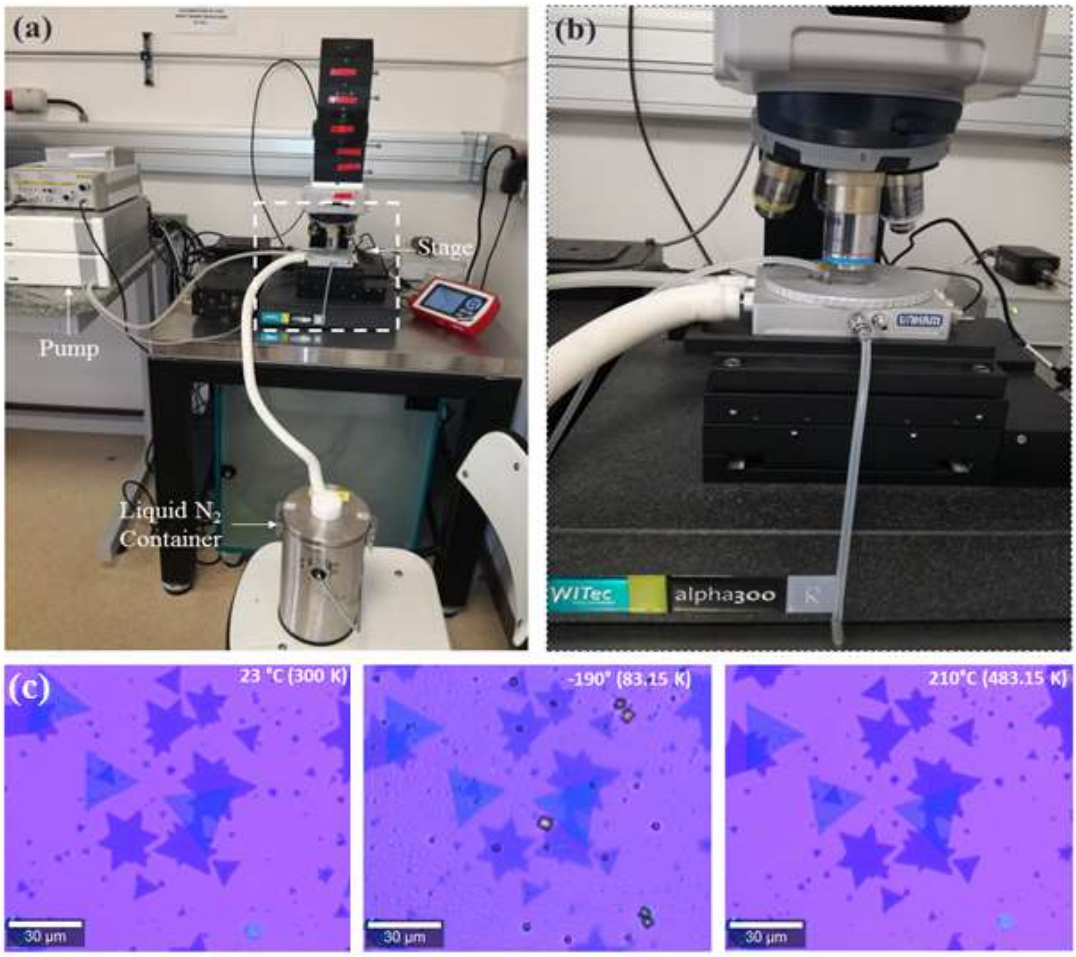

Figure 6.2. *Temperature-dependent Raman measurement (a-b) setup and zoomed in temperature control stage (c) optical images of the isolated hetero bilayer taken at different temperature*

6.3.3 Temperature Dependence of the Raman Modes of Monolayer MoS_2

Irrespective of the region and annealing condition, each of the Raman peaks of the MoS_2 red shifts with increase in temperature. At this point, the differences between

the rate of shifts of the peaks (of MoS_2 in the hetero bilayer and isolated region, before and after annealing) are not observable. Therefore, in Figure 6.3, only the temperature dependent Raman shifts of the isolated MoS_2 is exhibited. After fitting each of the Raman peaks with the Lorentz model, Grüneisen model is used to extract the first order temperature coefficient of each of the peaks.

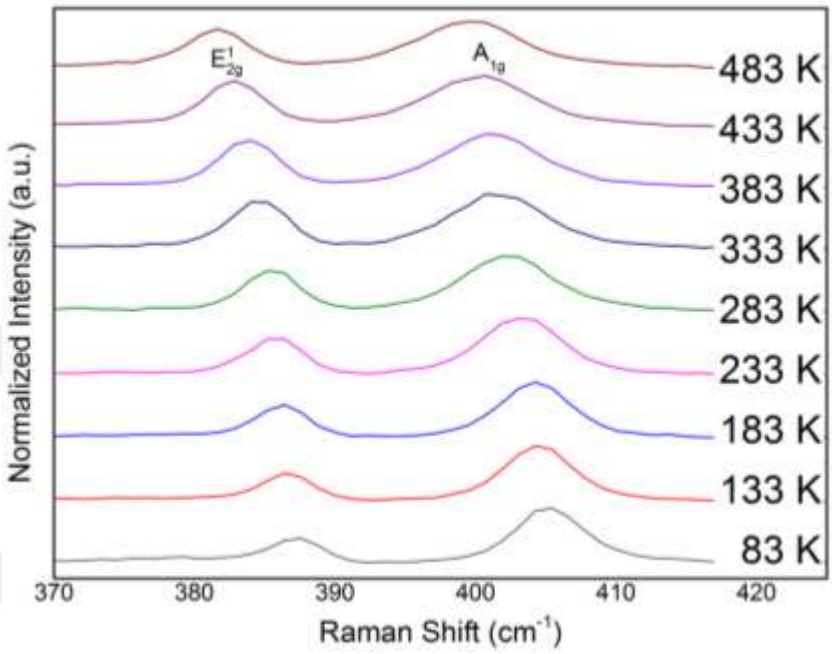

Figure 6.3. *Raman shifts of isolated the MoS_2 with the change in temperature*

Figure 6.4a-c shows the variation of the peak positions and FWHM of the MoS_2 E^1_{2g} and A_{1g} Raman modes with respect to the change in temperature. The χ values for the E^1_{2g} and A_{1g} modes are fitted to be $-12.8 \times 10^{-3} cm^{-1}/K$ and $-11.8 \times 10^{-3} cm^{-1}/K$ before annealing and $-13.5 \times 10^{-3} cm^{-1}/K$ and $-13.5 \times 10^{-3} cm^{-1}/K$ after annealing, respectively. These values are comparable with those reported in the literature as shown in Table 6.2. It is observed that the χ values of the two Raman modes increase before the thermal annealing. On the other hand, the FWHM of the each of the MoS_2 Raman modes, as shown in Figure 6.4b, broadens with increase in temperature both before and after annealing [191]. However, the broadening of the FWHM of the A_{1g} mode is more than that of the E^1_{2g} at every temperature increment. Figure 6.4c shows the A_{1g} and E^1_{2g} peaks difference as a function of temperature. It is observed that at the extreme temperatures, the difference between the two peaks reaches up to 19 cm^{-1}. However, the difference narrows down to ~17 cm^{-1} at room temperature.

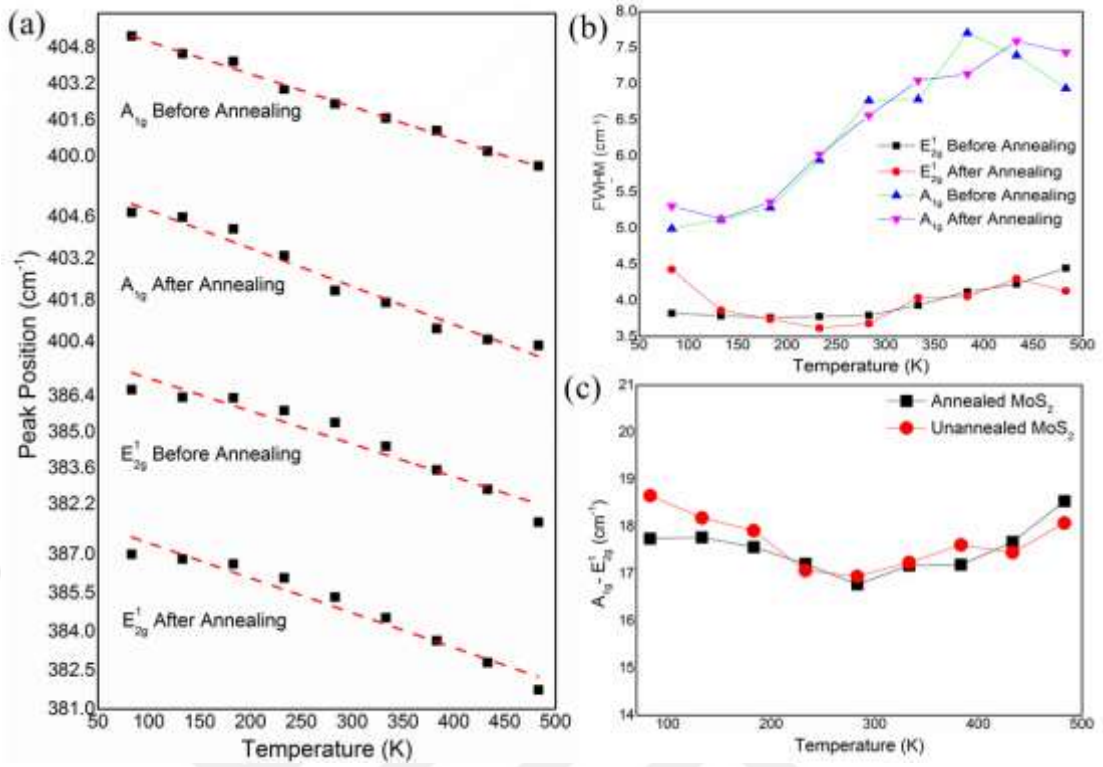

Figure 6.4. *(a) peak position (b) FWHM and (c) peaks difference of the Raman modes of the isolated MoS_2*

Figure 6.5a-b shows the peak positions and FWHM of the Raman vibrational modes of the MoS_2 in the hetero bilayer system. Like in the isolated region, the peak positions of the E^1_{2g} and A_{1g} modes decrease with the increase in the temperature and have the χ value of $-14.8 \times 10^{-3} cm^{-1}/K$ and $-11.8 \times 10^{-3} cm^{-1}/K$ before annealing and $-14.1 \times 10^{-3} cm^{-1}/K$ and $-12.4 \times 10^{-3} cm^{-1}/K$ after annealing, respectively. These χ values are comparable with the χ values reported for the suspended monolayer MoS_2 by Taube *et al.* [194]. This is likely to be influenced by the interlayer distance in the hetero bilayer system. In comparison with the χ values of the isolated MoS_2, the χ values of the MoS_2 in the hetero bilayer system are greater. Moreover, the χ values of the E^1_{2g} mode in the hetero bilayer system are greater than those of the isolated MoS_2. However, the χ values of the A_{1g} mode both in the isolated region and in the hetero bilayer system are comparable. It can be concluded that the E^1_{2g} mode in the hetero bilayer region, is more sensitive to temperature. The discrepancy is brought about by the van der Waals interaction between the layers [181]. By comparing the χ values of the MoS_2 before and after thermal annealing, it is found that these values are comparable. However, irrespective of the annealing condition, the A_{1g} mode show less response to the temperature than the E^1_{2g} mode.

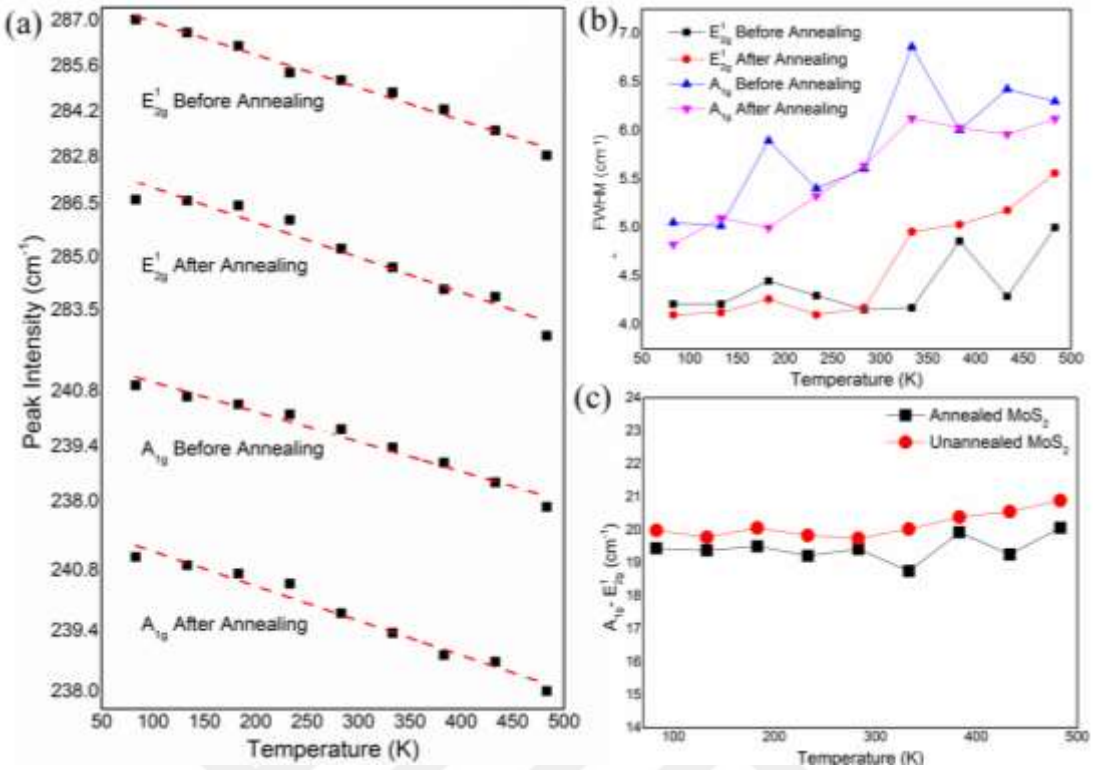

Figure 6.5. *(a) peak position (b) FWHM and (c) peaks difference of the Raman modes of the MoS_2 in the hetero bilayer system*

Figure 6.5b shows the FWHM of the Raman modes of the MoS_2 in the hetero bilayer system. Like the isolated MoS_2, broadening of the FWHM of the Raman modes is observed. However, relative to the MoS_2 in the isolated monolayer region, the broadening rate in the E^1_{2g} mode is higher in the hetero bilayer. Figure 6.5c shows the MoS_2 peaks difference with respect to the change in temperature. It is observed that from 83 K to the room temperature, the peaks difference does not change with the increase in temperature. However, after 280 K the peaks difference starts to increase steadily with increase in temperature. This is entirely a different trend compared to that which is observed in the isolated MoS_2. Also, the peaks difference maximum value reaches 21 cm^{-1} compared to the 19 cm^{-1} in the isolated Monolayer.

Table 6.2. *MoS_2 Raman modes χ values compared to those reported in the literature*

Temperature Range	Growth Technique	Material Description	$\chi(\times 10^{-3})(cm^{-1}/K)$		Ref.
			E^1_{2g}	A_{1g}	
303-448 K	*CVD*	*1L*	-13.0	-16.0	[191]
		FL	-15.0	-13.0	
300-642 K	*CVD*	*In WS_2/MoS_2 HB*	-11.1	-11.2	[181]
300-550 K	*ME*	*1L*	-17.9	-14.3	[192]
	ME	*FL*	-13.7	-18.9	
	CVD	*1L*	-13.8	-11.5	
90-540 K	*CVD*	*1L*	-12.1	-11.6	[193]
		2L	-11.8	-9.41	
83-523 K	*CVD*	*FL*	-13.2	-12.3	[195]
70-350 K	*ME*	*1L, Suspended*	-14.3	-12.4	[194]
83-483 K	*CVD*	*Isolated, before annealing*	-12.8 ± 1.0	-11.8 ± 0.3	This work
		Isolated, after annealing	-13.5 ± 1.0	-13.5 ± 1.0	
		In HB, before annealing	-14.3 ± 1.0	-11.8 ± 0.3	
		In HB, after annealing	-14.1 ± 1.0	-12.4 ± 0.8	

6.3.4 Temperature Dependence of the Raman Modes of Monolayer $MoSe_2$

Figure 6.6 shows the softening of the Raman vibrational modes of the $MoSe_2$ in the isolated region. In the figure, only the A_1 peak is shown because the intensity of the other peaks is very low. Like the MoS_2, all the Raman modes of the $MoSe_2$ soften with increase in temperature. After fitting each of the Raman peaks with the Lorentz model, Grüneisen model is used to extract the first order temperature coefficient of each of the peaks.

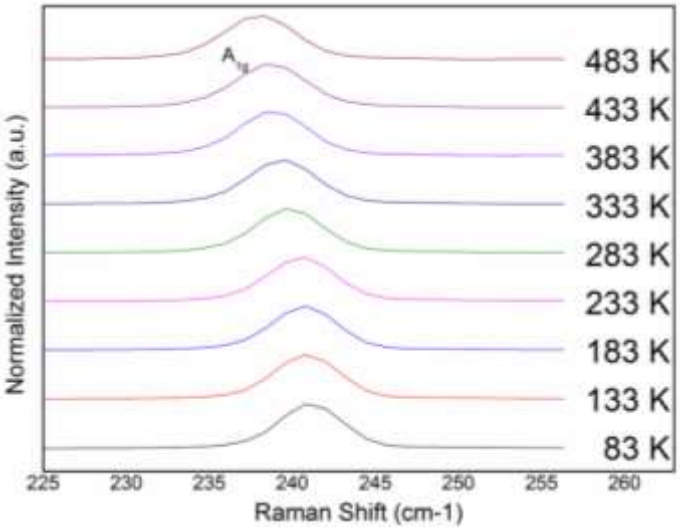

Figure 6.6. *Expanded view of the $MoSe_2$ Raman spectrum measured different temperature*

Figure 6.7a-b shows the peak position and FWHM of the Raman vibrational modes of $MoSe_2$ in the isolated region. The χ value for the E^1_{2g} and A_{1g} modes is calculated to

be $-10.1 \times 10^{-3} m^{-1}/K$ and $-7.6 \times 10^{-3} cm^{-1}/K$ before annealing and $-10.0 \times 10^{-3} cm^{-1}/K$ and $-8.0 \times 10^{-3} cm^{-1}/K$ after annealing, respectively. As shown in Table 6.3, the χ values we obtain for the A_{1g} mode are slightly lower than those reported in the literature for a monolayer $MoSe_2$ grown by ME and chemical exfoliation (CE). Our reported values are also slightly lower than that of the A_{1g} modes of the FL $MoSe_2$ grown by CE. Our χ values for the E^1_{2g} modes are larger by a factor of 3 than that of the FL $MoSe_2$ grown by CE [198]. Hence, these values, in comparison with those of the E^1_{2g} modes of MoS_2, are lower by at least $-2.84 \times 10^{-3} cm^{-1}/K$. It is also noted that the χ values of each vibrational mode increase after the thermal annealing. Moreover, it is noted that before and after the thermal annealing, the χ values of the E^1_{2g} modes are larger than those of the A_{1g}. It is noted that the E^1_{2g} mode's temperature coefficients – in each case – remain the same. This suggests that the thermal annealing does not affect the temperature dependence of the Raman mode. Figure 6.7b shows the FWHM of the of the isolated $MoSe_2$ vibrational modes with respect to the change in temperature. It is noted that the FWHM of the E^1_{2g} mode is broader than that of the A_{1g} at each temperature points. While the FWHM of the former shows somehow a constant broadening trend, the FWHM of the latter show an increasing broadening trend with the increase in temperature. The broadening trend of the FWHM of the A_{1g} mode, irrespective of the annealing condition, is identical.

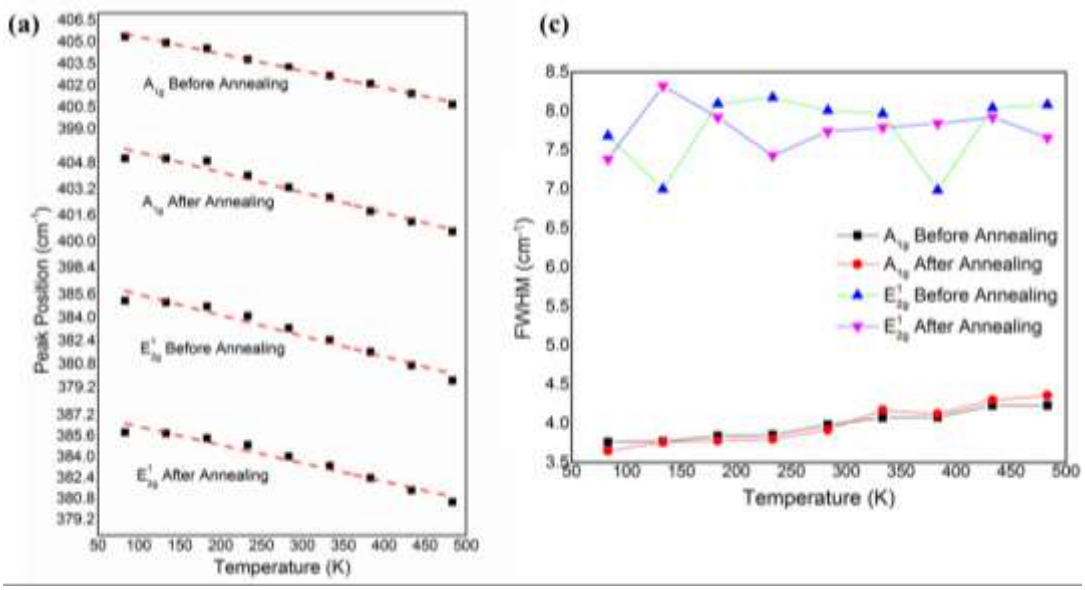

Figure 6.7. *(a) peak position (b) FWHM and (c) peaks difference of the Raman modes of the isolated $MoSe_2$*

The Raman vibrational modes of the $MoSe_2$ in the hetero bilayer system are also analyzed as shown in the shown in Figure 6.8a-c. The χ values for the E^1_{2g} and A_{1g} modes are calculated to be $-10.1 \times 10^{-3} cm^{-1}/K$ and $-9.0 \times 10^{-3} cm^{-1}/K$ before annealing and $-11.1 \times 10^{-3} cm^{-1}/K$ and $-9.0 \times 10^{-3} cm^{-1}/K$ after annealing, respectively. The χ values of the A_{1g} Raman mode are lower compared to those reported in the literature. On the other hand, the χ values of the E^1_{2g} mode are larger than those of the A_{1g} and are comparable to the value reported for FL $MoSe_2$ grown by CE as shown in the Table 6.3. We did not observe much difference between the χ values of the $MoSe_2$ Raman modes in the hetero bilayer and in the isolated counterpart in each case – except in the case of the $MoSe_2$ after thermal annealing whose temperature coefficients show some slight increase.

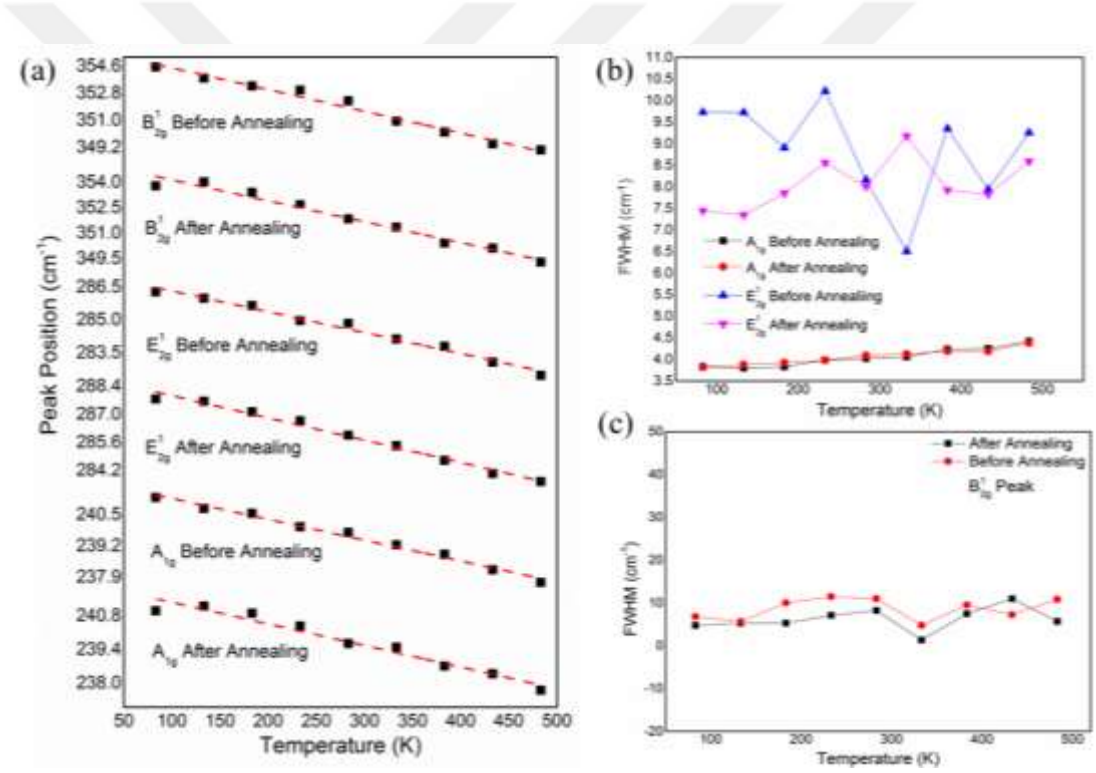

Figure 6.8. *(a) peak position (b) FWHM and (c) peaks difference of the Raman modes of the $MoSe_2$ in the hetero bilayer system*

The B^1_{2g} mode of the $MoSe_2$ that become active in the hetero bilayer system is also analyzed as shown in Figure 6.8a-c. The peak position of this Raman mode also shows linear dependence with temperature. The χ values of this peak are calculated to be $-14.5 \times 10^{-3} cm^{-1}/K$ before annealing and $-12.4 \times 10^{-3} cm^{-1}/K$ after annealing. It is noted that χ values of the peak before annealing are comparable with those of the E^1_{2g} modes of MoS_2 the hetero bilayer system. While after annealing the value reduces and

become comparable with the E^1_{2g} mode of the isolated MoS_2. Relative to the χ values of the other vibrational modes of $MoSe_2$, χ values of the B^1_{2g} mode are larger. These χ values are the largest recorded so far for monolayer $MoSe_2$. Figure 6.11c shows the FWHM of the peak with respect to the change in the temperature. According to the figure, a constant broadening trend in the FWHM of the B^1_{2g} mode is observed, and this trend is identical both before and after annealing.

Table 6.3. *$MoSe_2$ Raman modes' χ values compared to those in the literature*

Temperature Range	Growth Technique	Material Description	$\chi(\times 10^{-3})(cm^{-1}/K)$			Ref.
			E^1_{2g}	A_{1g}	B^1_{2g}	
175-575 K	*ME*	*1L*	-	-12.0	-	[188]
300-500 K	*ME*	*1L*	-	-11.1	-	[196]
		2L		-9.50		
77-400 K	*CE*	*FL*	-	-10.0	-	[197]
80-550 K	*CE*	*FL*	-4.60	-8.20	-16.0	[198]
83-483 K	*CVD*	*Isolated, before annealing*	-10.1 ± 0.4	-8.0 ± 0.5	-	This work
		Isolated, after annealing	-10.0 ± 0.8	-8.0 ± 0.5	-	
		In HB, before annealing	-10.0 ± 0.5	-8.6 ± 0.3	-14.5 ± 0.8	
		In HB, after annealing	-11.1 ± 0.5	-9.9 ± 0.4	-12.4 ± 0.4	

The Raman frequency shifts as a function of temperature that is observed in this study is predominantly due to temperature changes which result in the non-harmonic contribution of the interatomic potential energy due to phonon-phonon interaction and thermal expansion or volume contributions [181, 188, 191-198]. The thermal expansion mismatch between our substrate (SiO_2/Si) and the TMDs flakes may introduce some strain which may induce some shifts in the peak positions of the Raman modes. Nevertheless, over the temperature range that is used in this study, the low thermal expansion of SiO_2/Si ($2.6 \times 10^{-6}/℃$) is believed to induce an insignificant shift in the peak positions of the TMDs flakes [192].

The temperature dependent Raman frequency shifts of the TMDs materials due to the anharmonic process and thermal expansion of material is a complex phenomenon, and it requires the understanding and the symmetry of the material molecules to perform a sophisticated calculation called normal coordinate analysis. To calculate the anhamonic contribution to the phonon mode frequency shifts, Equation (6.2) is used, which expresses frequency of the Raman vibrational mode as a function of volume and temperature [188, 192].

$$\left(\frac{\partial ln\omega}{\partial T}\right)_P = \left(\frac{\partial lnV}{\partial T}\right)_P \left(\frac{\partial ln\omega}{\partial V}\right)_T + \left(\frac{\partial ln\omega}{\partial T}\right)_V$$

$$\left(\frac{\partial ln\omega}{\partial T}\right)_P = -\frac{\gamma}{k}\left(\frac{\partial ln\omega}{\partial P}\right)_T + \left(\frac{\partial ln\omega}{\partial T}\right)_V \quad (6.2)$$

γ represents the volume thermal coefficient and k is the isothermal volume compressibility. The first term from the left of the equation is the temperature contribution at constant volume while the second term from the right of the equation is the volume contribution at a constant temperature. Thus, the inharmonic contribution can be computed from the derivative of the isobaric temperature, isothermal pressure, γ and k of the phonon mode wavenumbers in the materials [197, 201]. On the other hand, the double resonance phenomenon, that is very active in a monolayer and 2L, is used to explain the changes in the intensity, FWHM, and shift in the peak position as a function of temperature. The change in the FWHM of the Raman mode as a function of temperature can be attributed to "the many body theoretical calculations and phonon dispersion". The decay of zone center optical phonon into one acoustic and one optical phonon and the selection of these two phonons in TMDs phonon density of states contribute to the change in the FWHM. The change of the FWHM as a function of the change in temperature is given in Equation (6.3) [202].

$$\Gamma(T) = \Gamma_0 + A[1 + n(\omega_1, T) + n(\omega_2, T)] \quad (6.3)$$

where Γ_0 is the background contribution, A is the inharmonic coefficient, and $n(\omega, T)$ is the Bose-Einstein contribution function. The Γ_0, A, ω_1 and ω_2 parameters can be used to calculate the FWHM temperature dependence.

It is noted that, unlike the χ values, the FWHM of each of the vibrational modes of MoS_2 and $MoSe_2$ before and after annealing are comparable. To find out why the χ values differ when annealed and without annealing, it is important to understand the TMDs-substrate interaction before and after annealing. According to Su *et al.*, the TMDs atomic bonding between the substrate and the material is weak and non-uniform; also, there is the existence of chemical contaminants such as the polymer residue, H_2O, and O_2 absorbents in the TMDs film that after being transferred to a substrate. After thermal annealing, the bonding between the TMDs film and substrate become strong and the polymer residues and absorbents are burnt up. In a nutshell, thermal annealing modifies

the morphology of the TMDs film [199] therefore, the χ values become larger after thermal annealing.

6.4 Conclusion

To conclude, the fabrication of the $MoS_2/MoSe_2$ hetero bilayer system has been presented. Due to the weak van der Waals forces between the MoS_2 and glass substrate, the transfer of the MoS_2 to the $MoS_2/SiO_2/Si$ is achieved using an etching-free PMMA wet transfer method. After μRaman, PL, and AFM analysis, the hetero bilayer system is confirmed to be of high quality due to the observation of the new Raman vibrational mode (B^1_{2g}) at 354.7 cm^{-1} and the interlayer exciton at 914.8 nm. To fill the gap in the literature, the temperature dependent frequency shift of the Raman phonon modes of monolayer $MoS_2/MoSe_2$ hetero bilayer system is studied over the temperature range of 83 K and 483 K. The Raman modes of both the MoS_2 and $MoSe_2$ are found to show linear dependency with the temperature due to the anharmonicity and thermal expansion effect. Each of the two 2D TMDs materials are studied in the isolated region and in the hetero bilayer regions before and after thermal annealing. Due to the van der Waals interaction between the layers, each of the temperature coefficient in the MoS_2 and $MoSe_2$ in the hetero bilayer system is found to be larger than in the isolated case. The FWHM of many of the phonon modes of the MoS_2 and $MoSe_2$ show broadening which increase with temperature irrespective of annealing condition. It is found that, throughout experiment, the MoS_2 and $MoSe_2$ flakes in the hetero bilayer system are not damaged and the room temperature Raman frequency does not change suggestive of the hetero bilayer system-based device durability under extreme temperature.

7. CONCLUSION AND FUTURE WORK

7.1 Conclusion

To conclude, this work presents a study of 2D materials and their hetero bilayer system for optoelectronic applications. CVD and ALD methods are used to grow high quality and large area 2D MoS_2 and $MoSe_2$. Each material is characterized by μRaman, PL and AFM analysis; the results are compared with the literature. By extension, $MoS_2/MoSe_2$ hetero bilayer system is fabricated by PMMA-assted wet transfer method. It is observed that the direct bandgap of the MoS_2 and $MoSe_2$ quenched in the hetero bilayer system due to charge transfer mechanism. A new peak at ~ 254 cm^{-1} and interlayer exciton at ~ 914 nm are also observed in the hetero bilayer system. To fill gaps in the literature, temperature dependent μRaman study of the hetero bilayer system is carried out. Changes in the Raman mode vibrational frequency and FWHM induced by temperature has been analyzed as per the literature. Through out the measurement, the MoS_2 and $MoSe_2$ flakes did not show any damage or change in the their instrinsic properties suggessive of the durability of a $MoS_2/MoSe_2$ hetero bilayer system based device under extreme temperatures.

7.2 Future Work

There are still gaps to be filled in literature of both the 2D material and the hetero bilayer system. Therefore, the future work will focus on the following:

1. The ALD-assisted CVD method has shown promising results and can be extended to other 2D TMDs. TMDs flakes size could be greatly improved by incorporating the glass substrate in the growth process or coating the face down substrate by NaCl solution.
2. Fabrication of the $MoS_2/MoSe_2$ hetero bilayer system-based device by e-beam lithography to have more defined metal contacts would greatly simplify the extraction of the device's figures of merit.
3. The quality of the $MoS_2/MoSe_2$ hetero bilayer system would be higher if it is directly grown by CVD, to significantly reduce the transfer related damages and defects.
4. Scaling up the heterostructure system to more than 2 layers and tuning their interlayer distance by annealing or using a spacer (such as hBN) to enable the system to retain its direct band gap would be a great contribution to the literature.

8. REFERENCES

[1]. Sweeney, S.J. and J. Mukherjee, *Optoelectronic Devices and Materials*, in *Springer Handbook of Electronic and Photonic Materials*, S. Kasap and P. Capper, Editors. 2017, Springer International Publishing: Cham. p. 1-1.

[2]. Sweeney, S. and J. Mukherjee, *Optoelectronic Devices and Materials*. 2017. p. 1-1.

[3]. Ohring, M. and L. Kasprzak, *Chapter 6 - Electronic Charge-Induced Damage*, in *Reliability and Failure of Electronic Materials and Devices (Second Edition)*, M. Ohring and L. Kasprzak, Editors. 2015, Academic Press: Boston. p. 327-385.

[4]. Zhou, L., et al., *Brief Review of Surface Passivation on III-V Semiconductor.* Crystals, 2018. **8**: p. 226.

[5]. Novoselov, K.S., et al., *Electric Field Effect in Atomically Thin Carbon Films.* Science, 2004. **306**(5696): p. 666.

[6]. Akbar, F., et al., *Graphene synthesis, characterization and its applications in nanophotonics, nanoelectronics, and nanosensing.* Journal of Materials Science: Materials in Electronics, 2015. **26**(7): p. 4347-4379.

[7]. Novoselov, K.S., et al., *A roadmap for graphene.* Nature, 2012. **490**(7419): p. 192-200.

[8]. Vivekchand, S.R.C., et al., *Graphene-based electrochemical supercapacitors.* Journal of Chemical Sciences, 2008. **120**(1): p. 9-13.

[9]. Liu, C., et al., *Graphene-Based Supercapacitor with an Ultrahigh Energy Density.* Nano Letters, 2010. **10**(12): p. 4863-4868.

[10]. Qiu, Y., X. Zhang, and S. Yang, *High performance supercapacitors based on highly conductive nitrogen-doped graphene sheets.* Physical Chemistry Chemical Physics, 2011. **13**(27): p. 12554-12558.

[11]. Radisavljevic, B., et al., *Single-layer MoS2 transistors.* Nature Nanotechnology, 2011. **6**: p. 147.

[12]. Yin, Z., et al., *Single-Layer MoS2 Phototransistors.* ACS Nano, 2012. **6**(1): p. 74-80.

[13]. Geim, A.K. and I.V. Grigorieva, *Van der Waals heterostructures.* Nature, 2013. **499**: p. 419.

[14]. Das, S., et al., *Beyond Graphene: Progress in Novel Two-Dimensional Materials and van der Waals Solids.* Annual Review of Materials Research, 2015. **45**(1): p. 1-27.

[15]. Science, W.o. 2019 30/11/2019]; Available from: https://wcs.webofknowledge.com/RA/analyze.do?product=WOS&SID=E4XFdGgSgxrfLOwpi3S&field=PY_PublicationYear_PublicationYear_en&yearSort=true.

[16]. Cai, Z., et al., *Chemical Vapor Deposition Growth and Applications of Two-Dimensional Materials and Their Heterostructures.* Chemical Reviews, 2018. **118**(13): p. 6091-6133.

[17]. Dong, R. and I. Kuljanishvili, *Review Article: Progress in fabrication of transition metal dichalcogenides heterostructure systems.* Journal of Vacuum Science and Technology. B, Nanotechnology & Microelectronics, 2017. **35**(3): p. 030803.

[18]. Kim, M.S., et al., *Simultaneous Hosting of Positive and Negative Trions and the Enhanced Direct Band Emission in MoSe2/MoS2 Heterostacked Multilayers.* ACS Nano, 2016. **10**(6): p. 6211-6219.

[19]. Mouri, S., et al. *Photoluminescence Properties in Monolayer MoSe2-MoS2 Hetero-Structures*. in *JSAP-OSA Joint Symposia 2015 Abstracts*. 2015. Nagoya, Aichi: Optical Society of America.

[20]. Ceballos, F., et al., *Ultrafast Charge Separation and Indirect Exciton Formation in a MoS2–MoSe2 van der Waals Heterostructure.* ACS Nano, 2014. **8**(12): p. 12717-12724.

[21]. Chen, H., et al., *Ultrafast formation of interlayer hot excitons in atomically thin MoS2/WS2 heterostructures.* Nature Communications, 2016. **7**: p. 12512.

[22]. Sohail, A. and Y. Jiabao, *Two-Dimensional Transition Metal Dichalcogenides and Their Charge Carrier Mobilities in Field Effect Transistors.* Nano-Micro Letters, 2017. **9**(4): p. 50.

[23]. Gupta, A., T. Sakthivel, and S. Seal, *Recent development in 2D materials beyond graphene.* Progress in Materials Science, 2015. **73**: p. 44-126.

[24]. Dubertret, B., T. Heine, and M. Terrones, *The Rise of Two-Dimensional Materials.* Accounts of Chemical Research, 2015. **48**(1): p. 1-2.

[25]. Chen, J., et al., *Chemical Vapor Deposition of Large-Size Monolayer MoSe2 Crystals on Molten Glass.* Journal of the American Chemical Society, 2017. **139**(3): p. 1073-1076.

[26]. Şar, H., et al., *A comparative device performance assesment of CVD grown MoS2 and WS2 monolayers.* Journal of Materials Science: Materials in Electronics, 2018. **29**(10): p. 8785-8792.

[27]. Li, H., et al., *From Bulk to Monolayer MoS2: Evolution of Raman Scattering.* Advanced Functional Materials, 2012. **22**(7): p. 1385-1390.

[28]. Liu, H., et al., *Role of the carrier gas flow rate in monolayer MoS2 growth by modified chemical vapor deposition*. Vol. 10. 2016.

[29]. Yang, P., et al., *Batch production of 6-inch uniform monolayer molybdenum disulfide catalyzed by sodium in glass.* Nature Communications, 2018. **9**(1): p. 979.

[30]. Wong, S.L., H. Liu, and D. Chi, *Recent progress in chemical vapor deposition growth of two-dimensional transition metal dichalcogenides.* Progress in Crystal Growth and Characterization of Materials, 2016. **62**(3): p. 9-28.

[31]. Geng, D. and H.Y. Yang, *Recent Advances in Growth of Novel 2D Materials: Beyond Graphene and Transition Metal Dichalcogenides.* Advanced Materials, 2018. **30**(45): p. 1800865.

[32]. Feyman, R.P., *There's Plenty of Room at the Bottom.* Engineering and Science, 1960. **25**(5): p. 15.

[33]. Frindt, R.F., *Optical Absorption of a Few Unit-Cell Layers of Mo${\mathrm{S}}_{2}$.* Physical Review, 1965. **140**(2A): p. A536-A539.

[34]. Frindt, R.F., *Single Crystals of MoS2 Several Molecular Layers Thick.* Journal of Applied Physics, 1966. **37**(4): p. 1928-1929.

[35]. Joensen, P., R.F. Frindt, and S.R. Morrison, *Single-layer MoS2.* Materials Research Bulletin, 1986. **21**(4): p. 457-461.

[36]. K. S. Novoselov, D.J., F. Schedin , T. J. Booth, V. V. Khotkevich, S. V. Morozov , and A. K. Geim, *Two-Dimensional Atomic Crystals.* Proceedings of the National Academy of Sciences of the United States of America (PNAS), 2005. **102**(30): p. 4.

[37]. Bradley, D. *Thousands of 2D materials are just waiting to be discovered*. 2018 [cited 2019 3/3/2019]; Available from:

https://www.chemistryworld.com/news/thousands-of-2d-materials-are-just-waiting-to-be-discovered/3008661.article.

[38]. Cheng, J., et al., *Recent Advances in Optoelectronic Devices Based on 2D Materials and Their Heterostructures.* Advanced Optical Materials, 2019. **7**(1): p. 1800441.

[39]. Lee, C., et al., *Frictional Characteristics of Atomically Thin Sheets.* Science, 2010. **328**(5974): p. 76.

[40]. Ghatak, S., A.N. Pal, and A. Ghosh, *Nature of Electronic States in Atomically Thin MoS2 Field-Effect Transistors.* ACS Nano, 2011. **5**(10): p. 7707-7712.

[41]. Li, H., et al., *Fabrication of Single- and Multilayer MoS2 Film-Based Field-Effect Transistors for Sensing NO at Room Temperature.* Small, 2012. **8**(1): p. 63-67.

[42]. Gao, E., et al., *Mechanical exfoliation of two-dimensional materials.* Journal of the Mechanics and Physics of Solids, 2018. **115**: p. 248-262.

[43]. Yi, M. and Z. Shen, *A review on mechanical exfoliation for the scalable production of graphene.* Journal of Materials Chemistry A, 2015. **3**(22): p. 11700-11715.

[44]. Zhi, C., et al., *Large-Scale Fabrication of Boron Nitride Nanosheets and Their Utilization in Polymeric Composites with Improved Thermal and Mechanical Properties.* Advanced Materials, 2009. **21**(28): p. 2889-2893.

[45]. Zeng, Z., et al., *Single-Layer Semiconducting Nanosheets: High-Yield Preparation and Device Fabrication.* Angewandte Chemie International Edition, 2011. **50**(47): p. 11093-11097.

[46]. Eda, G., et al., *Photoluminescence from Chemically Exfoliated MoS2.* Nano Letters, 2011. **11**(12): p. 5111-5116.

[47]. Han, S.A., R. Bhatia, and S.-W. Kim, *Synthesis, properties and potential applications of two-dimensional transition metal dichalcogenides.* Nano Convergence, 2015. **2**(1): p. 17.

[48]. Liu, K.-K., et al., *Growth of Large-Area and Highly Crystalline MoS2 Thin Layers on Insulating Substrates.* Nano Letters, 2012. **12**(3): p. 1538-1544.

[49]. Feng, Y., et al., *Synthesis of Large-Area Highly Crystalline Monolayer Molybdenum Disulfide with Tunable Grain Size in a H2 Atmosphere.* ACS Applied Materials & Interfaces, 2015. **7**(40): p. 22587-22593.

[50]. George, A., et al., *Wafer Scale Synthesis and High Resolution Structural Characterization of Atomically Thin MoS2 Layers.* Advanced Functional Materials, 2014.

[51]. Wang, X., et al., *Controlled Synthesis of Highly Crystalline MoS2 Flakes by Chemical Vapor Deposition.* Journal of the American Chemical Society, 2013. **135**(14): p. 5304-5307.

[52]. Lin, Y.-C., et al., *Wafer-scale MoS2 thin layers prepared by MoO3 sulfurization.* Nanoscale, 2012. **4**(20): p. 6637-6641.

[53]. Dai, T.-J., et al., *Synthesis of few-layer 2H-MoSe2 thin films with wafer-level homogeneity for high-performance photodetector*, in *Nanophotonics*. 2018. p. 1959.

[54]. Jin, Z., et al., *Novel chemical route for atomic layer deposition of MoS2 thin film on SiO2/Si substrate.* Nanoscale, 2014. **6**(23): p. 14453-14458.

[55]. Kim, S., et al., *Wafer-Scale Growth of MoS 2 Thin Films by Atomic Layer Deposition.* Nanoscale, 2016. **8**.

[56]. Krbal, M., et al., *2D MoSe2 Structures Prepared by Atomic Layer Deposition.* physica status solidi (RRL) – Rapid Research Letters, 2018. **12**(5): p. 1800023.

[57]. Valdivia, A., D. Tweet, and J. Conley, *Atomic layer deposition of two dimensional MoS2 on 150 mm substrates.* Journal of Vacuum Science & Technology A: Vacuum, Surfaces, and Films, 2016. **34**: p. 021515.

[58]. Tan, L.K., et al., *Atomic layer deposition of a MoS2 film.* Nanoscale, 2014. **6**(18): p. 10584-10588.

[59]. Liu, L., et al., *Layer-controlled precise fabrication of ultrathin MoS2 films by atomic layer deposition.* Nanotechnology, 2017. **28**(19): p. 195605.

[60]. Mattinen, M., et al., *Atomic Layer Deposition of Crystalline MoS2 Thin Films: New Molybdenum Precursor for Low-Temperature Film Growth.* Advanced Materials Interfaces, 2017. **4**(18): p. 1700123.

[61]. Alavi, K., *Molecular Beam Epitaxy*, in *Encyclopedia of Materials: Science and Technology*, K.H.J. Buschow, et al., Editors. 2001, Elsevier: Oxford. p. 5765-5780.

[62]. Wu, R., et al., *Large-area single-crystal sheets of borophene on Cu(111) surfaces.* Nature Nanotechnology, 2019. **14**(1): p. 44-49.

[63]. Cheng, P., et al., *Chapter 4 - Molecular beam epitaxy fabrication of two-dimensional materials*, in *2D Semiconductor Materials and Devices*, D. Chi, K.E.J. Goh, and A.T.S. Wee, Editors. 2020, Elsevier. p. 103-134.

[64]. Vishwanath, S., P. Dang, and H.G. Xing, *Chapter 20 - Challenges and Opportunities in Molecular Beam Epitaxy Growth of 2D Crystals: An Overview*, in *Molecular Beam Epitaxy (Second Edition)*, M. Henini, Editor. 2018, Elsevier. p. 443-485.

[65]. Ayberk, Ö., et al., *CVD growth of monolayer MoS 2 : Role of growth zone configuration and precursors ratio.* Japanese Journal of Applied Physics, 2017. **56**(6S1): p. 06GG05.

[66]. Özden, A., et al., *CVD grown 2D MoS2 layers: A photoluminescence and fluorescence lifetime imaging study*. physica status solidi (RRL) – Rapid Research Letters, 2016. **10**(11): p. 792-796.

[67]. Tsai, M.-L., et al., *Monolayer MoS2 Heterojunction Solar Cells.* ACS Nano, 2014. **8**(8): p. 8317-8322.

[68]. Krasnok, A., S. Lepeshov, and A. Alú, *Nanophotonics with 2D transition metal dichalcogenides [Invited]*. Optics Express, 2018. **26**(12): p. 15972-15994.

[69]. Mouri, S., et al., *Thermal dissociation of inter-layer excitons in MoS2/MoSe2 hetero-bilayers.* Nanoscale, 2017. **9**(20): p. 6674-6679.

[70]. Tonndorf, P., et al., *Photoluminescence emission and Raman response of monolayer MoS2, MoSe2, and WSe2.* Optics Express, 2013. **21**(4): p. 4908-4916.

[71]. Shim, G.W., et al., *Large-Area Single-Layer MoSe2 and Its van der Waals Heterostructures.* ACS Nano, 2014. **8**(7): p. 6655-6662.

[72]. Shaw, J.C., et al., *Chemical vapor deposition growth of monolayer MoSe2 nanosheets.* Nano Research, 2014. **7**(4): p. 511-517.

[73]. Smithe, K.K.H., et al., *Nanoscale Heterogeneities in Monolayer MoSe2 Revealed by Correlated Scanning Probe Microscopy and Tip-Enhanced Raman Spectroscopy*. ACS Applied Nano Materials, 2018. **1**(2): p. 572-579.

[74]. Wang, X., et al., *Chemical Vapor Deposition Growth of Crystalline Monolayer MoSe2.* ACS Nano, 2014. **8**(5): p. 5125-5131.

[75]. Li, X., et al., *Isoelectronic Tungsten Doping in Monolayer MoSe2 for Carrier Type Modulation.* Advanced Materials, 2016. **28**(37): p. 8240-8247.

[76]. Lee, C., et al., *Measurement of the Elastic Properties and Intrinsic Strength of Monolayer Graphene.* Science, 2008. **321**(5887): p. 385.

[77]. Lee, S.K.K., Hyun; Shim, Bong Sup *Graphene: an emerging material for biological tissue engineering.* Carbon Letters, 2013. **14**(13).

[78]. Balandin, A.A., *Thermal properties of graphene and nanostructured carbon materials.* Nature Materials, 2011. **10**(8): p. 569-581.

[79]. Mayorov, A.S., et al., *Micrometer-Scale Ballistic Transport in Encapsulated Graphene at Room Temperature.* Nano Letters, 2011. **11**(6): p. 2396-2399.

[80]. Choi, W., et al., *Synthesis of Graphene and Its Applications: A Review.* Critical Reviews in Solid State and Materials Sciences, 2010. **35**(1): p. 52-71.

[81]. Aditya, D.G., R.S. Abhay, and J.K. Vilasrao, *Graphene: A Comprehensive Review.* Current Drug Targets, 2017. **18**(6): p. 724-733.

[82]. Chhowalla, M., et al., *The chemistry of two-dimensional layered transition metal dichalcogenide nanosheets.* Nature Chemistry, 2013. **5**: p. 263.

[83]. Chhowalla, M., D. Jena, and H. Zhang, *Two-dimensional semiconductors for transistors.* Nature Reviews Materials, 2016. **1**: p. 16052.

[84]. Friedman, A.L., et al., *Evidence for Chemical Vapor Induced 2H to 1T Phase Transition in MoX2 (X = Se, S) Transition Metal Dichalcogenide Films.* Scientific Reports, 2017. **7**(1): p. 3836.

[85]. Pergoz, N.K., *CVD GROWTH and CHARACTERIZATION OF 2D TRANSITION METAL DICHALCOGENIDES, MoS2 and WS2.* Anadolu University Journal of Science and Technology A- Applied Sciences and Engineering, 2017. **18**(2): p. 375 - 387.

[86]. Jung, C., et al., *Highly Crystalline CVD-grown Multilayer MoSe2 Thin Film Transistor for Fast Photodetector.* Scientific Reports, 2015. **5**: p. 15313.

[87]. Wypych, F. and R. Schöllhorn, *1T-MoS2, a new metallic modification of molybdenum disulfide.* Journal of the Chemical Society, Chemical Communications, 1992(19): p. 1386-1388.

[88]. Papageorgopoulos, C.A. and W. Jaegermann, *Li intercalation across and along the van der Waals surfaces of MoS2(0001).* Surface Science, 1995. **338**(1): p. 83-93.

[89]. Hu, X., et al., *1T phase as an efficient hole injection layer to TMDs transistors: a universal approach to achieve p-type contacts.* 2D Materials, 2018. **5**(3): p. 031012.

[90]. Yu, Y., et al., *High phase-purity 1T'-MoS2- and 1T'-MoSe2-layered crystals.* Nature Chemistry, 2018. **10**(6): p. 638-643.

[91]. Yin, Y., et al., *Synergistic Phase and Disorder Engineering in 1T-MoSe2 Nanosheets for Enhanced Hydrogen-Evolution Reaction.* Advanced Materials, 2017. **29**(28): p. 1700311.

[92]. Huang, X., Z. Zeng, and H. Zhang, *Metal dichalcogenide nanosheets: preparation, properties and applications.* Chemical Society Reviews, 2013. **42**(5): p. 1934-1946.

[93]. Kc, S., et al., *Impact of intrinsic atomic defects on the electronic structure of MoS2monolayers.* Nanotechnology, 2014. **25**(37): p. 375703.

[94]. Lin, Z., et al., *Defect engineering of two-dimensional transition metal dichalcogenides.* 2D Materials, 2016. **3**(2): p. 022002.

[95]. Schaibley, J.R., et al., *Valleytronics in 2D materials.* Nature Reviews Materials, 2016. **1**: p. 16055.

[96]. Jariwala, D., et al., *Van der Waals Materials for Atomically-Thin Photovoltaics: Promise and Outlook.* ACS Photonics, 2017. **4**(12): p. 2962-2970.

[97]. Choudhary, N., et al., *Centimeter Scale Patterned Growth of Vertically Stacked Few Layer Only 2D MoS2/WS2 van der Waals Heterostructure.* Scientific Reports, 2016. **6**: p. 25456.

[98]. Chen, K., et al., *Electronic Properties of MoS2–WS2 Heterostructures Synthesized with Two-Step Lateral Epitaxial Strategy.* ACS Nano, 2015. **9**(10): p. 9868-9876.

[99]. Carozo, V., et al., *Excitonic processes in atomically-thin MoSe2/MoS2 vertical heterostructures.* 2D Materials, 2018. **5**(3): p. 031016.

[100]. Li, S., et al., *Heterojunction engineering of MoSe2/MoS2 with electronic modulation towards synergetic hydrogen evolution reaction and supercapacitance performance.* Chemical Engineering Journal, 2019. **359**: p. 1419-1426.

[101]. Zhou, J., et al., *A library of atomically thin metal chalcogenides.* Nature, 2018. **556**(7701): p. 355-359.

[102]. Zhang, N., et al., *Moiré Intralayer Excitons in a MoSe2/MoS2 Heterostructure.* Nano Letters, 2018. **18**(12): p. 7651-7657.

[103]. Wang, Z., et al., *NaCl-assisted one-step growth of MoS2–WS2 in-plane heterostructures.* Nanotechnology, 2017. **28**(32): p. 325602.

[104]. Roy, S., et al., *Observation of Charge Transfer in Heterostructures Composed of MoSe2 Quantum Dots and a Monolayer of MoS2 or WSe2.* The Journal of Physical Chemistry C, 2017. **121**(3): p. 1997-2004.

[105]. Huang, A.a.a. *Observation of Interlayer Excitons in Monolayer MoSe2-WSe2 Heterostructures on BN substrate*. 2015; Available from: https://pdfs.semanticscholar.org/541e/1624d7eccd0aa5c7a4f97af79e1f97b8a9ba.pdf.

[106]. Lui, C.H., et al., *Observation of interlayer phonon modes in van der Waals heterostructures.* Physical Review B, 2015. **91**(16): p. 165403.

[107]. Fang, H., et al., *Strong interlayer coupling in van der Waals heterostructures built from single-layer chalcogenides.* Proceedings of the National Academy of Sciences, 2014. **111**(17): p. 6198-6202.

[108]. Bellus, M.Z., et al., *Tightly Bound Trions in Transition Metal Dichalcogenide Heterostructures.* ACS Nano, 2015. **9**(6): p. 6459-6464.

[109]. Bablich, A., S. Kataria, and M. Lemme, *Graphene and Two-Dimensional Materials for Optoelectronic Applications.* Electronics, 2016. **5**: p. 13.

[110]. Wei, X., et al., *Photodetectors based on junctions of two-dimensional transition metal dichalcogenides.* Chinese Physics B, 2017. **26**(3): p. 038504.

[111]. Gong, C., et al., *Electronic and Optoelectronic Applications Based on 2D Novel Anisotropic Transition Metal Dichalcogenides.* Advanced Science, 2017. **4**(12): p. 1700231.

[112]. Lopez-Sanchez, O., et al., *Ultrasensitive photodetectors based on monolayer MoS2.* Nature Nanotechnology, 2013. **8**: p. 497.

[113]. Ko, P.J., et al., *High-performance near-infrared photodetector based on nano-layered MoSe2.* Semiconductor Science and Technology, 2017. **32**(6): p. 065015.

[114]. Yu, W.J., et al., *Highly efficient gate-tunable photocurrent generation in vertical heterostructures of layered materials.* Nature Nanotechnology, 2013. **8**(12): p. 952-958.

[115]. Xue, Y., et al., *Scalable Production of a Few-Layer MoS2/WS2 Vertical Heterojunction Array and Its Application for Photodetectors.* ACS Nano, 2016. **10**(1): p. 573-580.

[116] Ponraj, J.S., et al., *Photonics and optoelectronics of two-dimensional materials beyond graphene.* Nanotechnology, 2016. **27**(46): p. 462001.

[117]. Duan, X., et al., *Two-dimensional transition metal dichalcogenides as atomically thin semiconductors: opportunities and challenges.* Chemical Society Reviews, 2015. **44**(24): p. 8859-8876.

[118]. Shim, J., et al., *Electronic and Optoelectronic Devices based on Two-Dimensional Materials: From Fabrication to Application.* Advanced Electronic Materials, 2017. **3**(4): p. 1600364.

[119]. Fahrenbruch, A.L. and R.H. Bube, *CHAPTER 1 - SURVEY OF BASIC CONCEPTS*, in *Fundamentals of Solar Cells*, A.L. Fahrenbruch and R.H. Bube, Editors. 1983, Academic Press. p. 1-25.

[120]. Zheng, W., et al., *Patterning two-dimensional chalcogenide crystals of Bi2Se3 and In2Se3 and efficient photodetectors.* Nature Communications, 2015. **6**(1): p. 6972.

[121]. Wang, H., H. Feng, and J. Li, *Graphene and Graphene-like Layered Transition Metal Dichalcogenides in Energy Conversion and Storage.* Small, 2014. **10**(11): p. 2165-2181.

[122]. Lopez-Sanchez, O., et al., *Light Generation and Harvesting in a van der Waals Heterostructure.* ACS Nano, 2014. **8**(3): p. 3042-3048.

[123]. Shanmugam, M., et al., *Layered semiconductor tungsten disulfide: photoactive material in bulk heterojunction solar cells.* Nano Energy, 2013. **2**(3): p. 419-424.

[124]. Pospischil, A., M.M. Furchi, and T. Mueller, *Solar-energy conversion and light emission in an atomic monolayer p–n diode.* Nature Nanotechnology, 2014. **9**(4): p. 257-261.

[125]. Baugher, B.W.H., et al., *Optoelectronic devices based on electrically tunable p–n diodes in a monolayer dichalcogenide.* Nature Nanotechnology, 2014. **9**(4): p. 262-267.

[126]. Groenendijk, D.J., et al., *Photovoltaic and Photothermoelectric Effect in a Double-Gated WSe2 Device.* Nano Letters, 2014. **14**(10): p. 5846-5852.

[127]. Cheng, R., et al., *Electroluminescence and Photocurrent Generation from Atomically Sharp WSe2/MoS2 Heterojunction p–n Diodes.* Nano Letters, 2014. **14**(10): p. 5590-5597.

[128]. Gu, X., et al., *A Solution-Processed Hole Extraction Layer Made from Ultrathin MoS2 Nanosheets for Efficient Organic Solar Cells.* Advanced Energy Materials, 2013. **3**(10): p. 1262-1268.

[129]. Jiao, K., et al., *The role of MoS2 as an interfacial layer in graphene/silicon solar cells.* Physical Chemistry Chemical Physics, 2015. **17**(12): p. 8182-8186.

[130]. Tahersima, M.H. and V.J. Sorger, *Strong Photon Absorption in 2-D Material-Based Spiral Photovoltaic Cells.* MRS Advances, 2016. **1**(59): p. 3915-3921.

[131]. Jo, S., et al., *Mono- and Bilayer WS2 Light-Emitting Transistors.* Nano Letters, 2014. **14**(4): p. 2019-2025.

[132]. Withers, F., et al., *Light-emitting diodes by band-structure engineering in van der Waals heterostructures.* Nature Materials, 2015. **14**(3): p. 301-306.

[133]. Braga, D., et al., *Quantitative Determination of the Band Gap of WS2 with Ambipolar Ionic Liquid-Gated Transistors.* Nano Letters, 2012. **12**(10): p. 5218-5223.

[134]. Zaumseil, J., *Electronic Control of Circularly Polarized Light Emission.* Science, 2014. **344**(6185): p. 702.

[135]. Zhang, Y.J., et al., *Electrically Switchable Chiral Light-Emitting Transistor.* Science, 2014. **344**(6185): p. 725.

[136]. Kamiya, T. and M. Tsuchiya, *Progress in Ultrafast Photonics.* Japanese Journal of Applied Physics, 2005. **44**(8): p. 5875-5888.

[137]. Bonaccorso, F., et al., *Graphene photonics and optoelectronics.* Nature Photonics, 2010. **4**(9): p. 611-622.

[138]. Bonaccorso, F. and Z. Sun, *Solution processing of graphene, topological insulators and other 2d crystals for ultrafast photonics.* Optical Materials Express, 2014. **4**(1): p. 63-78.

[139]. !!! INVALID CITATION !!! {}.

[140]. Luo, Z., et al., *1.06μm Q-switched ytterbium-doped fiber laser using few-layer topological insulator Bi2Se3 as a saturable absorber.* Optics Express, 2013. **21**(24): p. 29516-29522.

[141]. Zhao, C., et al., *Wavelength-tunable picosecond soliton fiber laser with Topological Insulator: Bi2Se3 as a mode locker.* Optics Express, 2012. **20**(25): p. 27888-27895.

[142]. Bao, Q. and K.P. Loh, *Graphene Photonics, Plasmonics, and Broadband Optoelectronic Devices.* ACS Nano, 2012. **6**(5): p. 3677-3694.

[143]. Sotor, J., et al., *Mode-locking in Er-doped fiber laser based on mechanically exfoliated Sb2Te3 saturable absorber.* Optical Materials Express, 2014. **4**(1): p. 1-6.

[144]. Hajlaoui, M., et al., *Ultrafast Surface Carrier Dynamics in the Topological Insulator Bi2Te3.* Nano Letters, 2012. **12**(7): p. 3532-3536.

[145]. Hasan, M.Z. and C.L. Kane, *Colloquium: Topological insulators.* Reviews of Modern Physics, 2010. **82**(4): p. 3045-3067.

[146]. Wang, J., H. Mabuchi, and X.-L. Qi, *Calculation of divergent photon absorption in ultrathin films of a topological insulator.* Physical Review B, 2013. **88**(19): p. 195127.

[147]. Tang, P., et al., *Topological Insulator: $\hbox{Bi}_{2}\hbox{Te}_{3}$ Saturable Absorber for the Passive Q-Switching Operation of an in-Band Pumped 1645-nm Er:YAG Ceramic Laser.* IEEE Photonics Journal, 2013. **5**(2): p. 1500707-1500707.

[148]. *Thin-Film Materials and Processes*, in *Introduction to Microfabrication*. p. 47-67.

[149]. Dai, T., et al., *Characterization of Molybdenum Oxide Thin Films Grown by Atomic Layer Deposition.* Journal of Electronic Materials, 2018. **47**(11): p. 6709-6715.

[150]. Jung, Y., et al., *Recent Progresses in the Growth of Two-dimensional Transition Metal Dichalcogenides.* J. Korean Ceram. Soc, 2019. **56**(1): p. 24-36.

[151]. Wang, S., et al., *Shape Evolution of Monolayer MoS2 Crystals Grown by Chemical Vapor Deposition.* Chemistry of Materials, 2014. **26**(22): p. 6371-6379.

[152]. Marcelli, A., et al., *Biological applications of synchrotron radiation infrared spectromicroscopy.* Biotechnology Advances, 2012. **30**(6): p. 1390-1404.

[153]. Stern, C., et al., *Growth Mechanisms and Electronic Properties of Vertically Aligned MoS2.* Scientific Reports, 2018. **8**.

[154]. Chen, W., et al., *Oxygen-Assisted Chemical Vapor Deposition Growth of Large Single-Crystal and High-Quality Monolayer MoS2.* Journal of the American Chemical Society, 2015. **137**(50): p. 15632-15635.

[155]. Song, J.-G., et al., *Layer-Controlled, Wafer-Scale, and Conformal Synthesis of Tungsten Disulfide Nanosheets Using Atomic Layer Deposition.* ACS Nano, 2013. **7**(12): p. 11333-11340.

[156]. Diskus, M., O. Nilsen, and H. Fjellvåg, *Growth of thin films of molybdenum oxide by atomic layer deposition.* Journal of Materials Chemistry, 2011. **21**(3): p. 705-710.

[157]. Liu, H., et al., *Atomic layer deposition and post-growth thermal annealing of ultrathin MoO3 layers on silicon substrates: Formation of surface nanostructures.* Applied Surface Science, 2018. **439**.

[158]. Mattinen, M., et al., *Atomic layer deposition of crystalline molybdenum oxide thin films and phase control by post-deposition annealing.* Materials Today Chemistry, 2018. **9**: p. 17-27.

[159]. Macco, B., et al., *Low-temperature atomic layer deposition of MoOx for silicon heterojunction solar cells.* physica status solidi (RRL) – Rapid Research Letters, 2015. **9**(7): p. 393-396.

[160]. Weimer, A.W., *Particle atomic layer deposition.* Journal of Nanoparticle Research, 2019. **21**(1): p. 9.

[161]. Buechler, J.R.W.L.H.S.M.G.A.W.W.K.J. *Coating fine iron particles with an oxidation-resistant gamma-alumina nanolayer using ALD in a fluidized bed reactor*. in *Fluidization XI, 11th International Conference on Fluidization, Present and Future for Fluidization Engineering*. 2004. Ischia, Italy: ECI.

[162]. Vos, M., et al., *Atomic layer deposition of molybdenum oxide from (NtBu)2(NMe2)2Mo and O2 plasma*. Vol. 34. 2016. 01A103.

[163]. Koike, K., et al., *Characteristics of MoO3films grown by molecular beam epitaxy.* Japanese Journal of Applied Physics, 2014. **53**(5S1): p. 05FJ02.

[164]. Camacho-López, M.A., et al., *Micro-Raman study of the m-MoO2 to α-MoO3 transformation induced by cw-laser irradiation.* Optical Materials, 2011. **33**(3): p. 480-484.

[165]. Dieterle, M., G. Weinberg, and G. Mestl, *Raman spectroscopy of molybdenum oxides Part I. Structural characterization of oxygen defects in MoO3−x by DR*

UV/VIS, Raman spectroscopy and X-ray diffraction. Physical Chemistry Chemical Physics, 2002. **4**(5): p. 812-821.

[166]. Eda, K., *Longitudinal-transverse splitting effects in IR absorption spectra of MoO3.* Journal of Solid State Chemistry, 1991. **95**(1): p. 64-73.

[167]. Seguin, L., et al., *Infrared and Raman spectra of MoO3 molybdenum trioxides and MoO3 · xH2O molybdenum trioxide hydrates.* Spectrochimica Acta Part A: Molecular and Biomolecular Spectroscopy, 1995. **51**(8): p. 1323-1344.

[168]. Liu, D., et al., *High-pressure Raman scattering and x-ray diffraction of phase transitions in MoO3.* Journal of Applied Physics, 2009. **105**(2): p. 023513.

[169]. Jiebing, S., Rui, X., Shimin, W. et al., Journal of Sol-Gel Science and Technology, 2003. **27**(3): p. 5.

[170]. Dayal, S. and C.S. Kumar, *Development of hierarchical layered nanostructuredα-MoO3thin films using dc magnetron sputtering.* Materials Research Express, 2016. **3**(10): p. 106405.

[171]. Pham, T.T.P., et al., *Facile method for synthesis of nanosized β–MoO3 and their catalytic behavior for selective oxidation of methanol to formaldehyde.* Advances in Natural Sciences: Nanoscience and Nanotechnology, 2015. **6**(4): p. 045010.

[172]. Navgire, M., et al., *Effect of Poly(ethylene glycol)-400 and Carbon on MoO3 Nanocomposite Materials and Its Catalytic Activity.* Chinese Journal of Chemistry, 2011. **29**(10): p. 2049-2056.

[173]. Nadimicherla, R., W. Chen, and X. Guo, *Synthesis and characterization of α-MoO3 nanobelt composite positive electrode materials for lithium battery application.* Materials Research Bulletin, 2015. **66**: p. 140-146.

[174]. Demirtaş, M., et al., *Layer and size distribution control of CVD-grown 2D MoS2 using ALD-deposited MoO3 structures as the precursor.* Materials Science in Semiconductor Processing, 2020. **108**: p. 104880.

[175]. Li, X. and H. Zhu, *Two-dimensional MoS2: Properties, preparation, and applications.* Journal of Materiomics, 2015. **1**(1): p. 33-44.

[176]. Kim, M.S., et al., *Photoluminescence wavelength variation of monolayer MoS2 by oxygen plasma treatment.* Thin Solid Films, 2015. **590**: p. 318-323.

[177]. INC., T.P. *Schott D263M Glass Coverslips Technical data*. 7/12/2019]; Available from: https://www.tedpella.com/histo_html/coverslip-info.htm.

[178]. Jin, Y., et al., *A Van Der Waals Homojunction: Ideal p–n Diode Behavior in MoSe2.* Advanced Materials, 2015. **27**(37): p. 5534-5540.

[179]. Kang, J., et al., *Electronic Structural Moiré Pattern Effects on MoS2/MoSe2 2D Heterostructures.* Nano Letters, 2013. **13**(11): p. 5485-5490.

[180]. Liu, B., et al., *Coupled relaxation channels of excitons in monolayer MoSe2.* Nanoscale, 2017. **9**(46): p. 18546-18551.

[181]. Hu, Z., et al., *Temperature dependent Raman and photoluminescence of vertical WS2/MoS2 monolayer heterostructures.* Science Bulletin, 2017. **62**(1): p. 16-21.

[182]. Britnell, L., et al., *Strong Light-Matter Interactions in Heterostructures of Atomically Thin Films.* Science, 2013. **340**(6138): p. 1311.

[183]. Bernardi, M., M. Palummo, and J.C. Grossman, *Extraordinary Sunlight Absorption and One Nanometer Thick Photovoltaics Using Two-Dimensional Monolayer Materials.* Nano Letters, 2013. **13**(8): p. 3664-3670.

[184]. Furchi, M.M., et al., *Device physics of van der Waals heterojunction solar cells.* npj 2D Materials and Applications, 2018. **2**(1): p. 3.

[185]. Raman, C.V. and K.S. Krishnan, *A New Type of Secondary Radiation.* Nature, 1928. **121**(3048): p. 501-502.

[186]. Raman, C.V., *A new radiation [Reproduced from Indian J. Phys., 1928, 2, 387–398].* Current Science, 1998. **74**(4): p. 382-386.

[187]. Chakraborty, B., et al., *Symmetry-dependent phonon renormalization in monolayer MoS${}_{2}$ transistor.* Physical Review B, 2012. **85**(16): p. 161403.

[188]. Yang, M., et al., *Anharmonicity of monolayer MoS2, MoSe2, and WSe2: A Raman study under high pressure and elevated temperature.* Applied Physics Letters, 2017. **110**(9): p. 093108.

[189]. Ataca, C., et al., *A Comparative Study of Lattice Dynamics of Three- and Two-Dimensional MoS2.* The Journal of Physical Chemistry C, 2011. **115**(33): p. 16354-16361.

[190]. Rice, C., et al., *Raman-scattering measurements and first-principles calculations of strain-induced phonon shifts in monolayer MoS${}_{2}$.* Physical Review B, 2013. **87**(8): p. 081307.

[191]. Lanzillo, N.A., et al., *Temperature-dependent phonon shifts in monolayer MoS2.* Applied Physics Letters, 2013. **103**(9): p. 093102.

[192]. Najmaei, S., P.M. Ajayan, and J. Lou, *Quantitative analysis of the temperature dependency in Raman active vibrational modes of molybdenum disulfide atomic layers.* Nanoscale, 2013. **5**(20): p. 9758-9763.

[193]. Yang, T., et al., *Excitation mechanism of A1g mode and origin of nonlinear temperature dependence of Raman shift of CVD-grown mono- and few-layer MoS2 films.* Optics Express, 2016. **24**(11): p. 12281-12292.

[194]. Taube, A., et al., *Temperature-Dependent Nonlinear Phonon Shifts in a Supported MoS2 Monolayer*. ACS Applied Materials & Interfaces, 2014. **6**(12): p. 8959-8963.

[195]. Sahoo, S., et al., *Temperature-Dependent Raman Studies and Thermal Conductivity of Few-Layer MoS2.* The Journal of Physical Chemistry C, 2013. **117**(17): p. 9042-9047.

[196]. Zhang, X., et al., *Measurement of Lateral and Interfacial Thermal Conductivity of Single- and Bilayer MoS2 and MoSe2 Using Refined Optothermal Raman Technique.* ACS Applied Materials & Interfaces, 2015. **7**(46): p. 25923-25929.

[197]. Sarkar, A.S. and S.K. Pal, *Electron-Phonon Interaction in Organic/2D-Transition Metal Dichalcogenide Heterojunctions: A Temperature-Dependent Raman Spectroscopic Study.* ACS omega, 2017. **2**(8): p. 4333-4340.

[198]. Sun, D., et al., *Formation and Interlayer Decoupling of Colloidal MoSe2 Nanoflowers.* Chemistry of Materials, 2015. **27**(8): p. 3167-3175.

[199]. Su, L., et al., *In Situ Monitoring of the Thermal-Annealing Effect in a Monolayer of ${\mathrm{MoS}}_{2}$.* Physical Review Applied, 2017. **7**(3): p. 034009.

[200]. Huang, X., et al., *Quantitative Analysis of Temperature Dependence of Raman shift of monolayer WS2.* Scientific Reports, 2016. **6**: p. 32236.

[201]. Pawbake, A.S., et al., *Large area chemical vapor deposition of monolayer transition metal dichalcogenides and their temperature dependent Raman spectroscopy studies.* Nanoscale, 2016. **8**(5): p. 3008-3018.

[202]. Menéndez, J. and M. Cardona, *Temperature dependence of the first-order Raman scattering by phonons in Si, Ge, and $\ensuremath{\alpha}\ensuremath{-}\mathrm{S}\mathrm{n}$: Anharmonic effects.* Physical Review B, 1984. **29**(4): p. 2051-2059.

APPENDIX

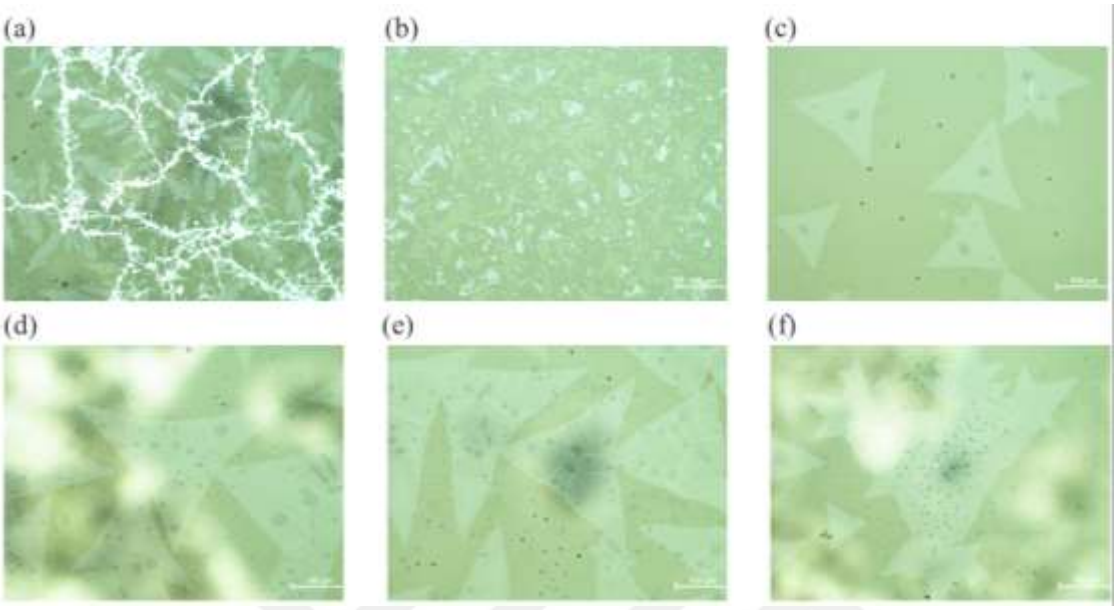

Figure A1.1. *Optical images of the CVD grown MoS_2 on the first glass substrates grown by using different recipes (a) recipe #1 (b) recipe #2-3 (c) recipe #4 (d) recipe #5 (e) d2 = 3 cm (f) N_2 = 250 sccm*

Table A1.1. *Summary of MoS_2 CVD growth experiments. Parameters changed are highlighted yellow*

Exp. No.	N_2 (sccm)	MoO_3 (mg)	S (mg)	d_1 (cm)	d_2 (cm)	Pressure (Torr)	Growth Temperature (°C)	Ramp Rate (°C/min)	Growth Time (min)
1	300	0.6	300	15	6	750	750°C	12.5	5
2	300	0.5	300	15	6	750	750°C	12.5	5
3	300	0.5	300	11	6	750	750°C	12.5	5
4	300	0.3	300	11	6	750	750°C	12.5	5
5	300	0.3	300	11	4	750	750°C	12.5	5
6	300	0.3	300	11	3	750	750°C	12.5	5
7	250	0.3	300	11	3	750	750°C	12.5	5

RESUME

Name : Yahaya SHEHU

Foreign Language : English

Birthplace and Year : Nigeria / 1988

E-Mail : yahaya.shehu@eskisehir.edu.tr

EDUCATION

2017-present Anadolu University, *MSc. Electronics Engineering*

2011-2015 American University of Nigeria, *B.Sc. Telecommunications and Wireless Technologies*

2005-2008 Shehu Shagari College of Education, *Nigeria Certificate in Education (NCE) in Computer Science Education*

WORK EXPERIENCE

2017-present Micro/Nano Devices and Systems (MIDAS) **Research Group Member**, Eskisehir Technical University, Department of Electronics Engineering

2010-2016 **Teaching-staff**, Sokoto State Teacher's Service Board, Department of Computer Science and Mathematics

2013-2015 **Resident Assistant**, American University of Nigeria, Residence Life Unit

2011-2013 **Part-time Staff**, Sokoto State Ministry of Education, Examinations Unit

2011-2012 **Assistant Supervisor**, National Examinations Council (NECO), Examination Administration Unit

2009-2010 **Teaching-staff**, Hilal Nursery and Primary School, Department of Mathematics

2007 **Teaching-practice Staff**, Sheikh Abubakar Mahmud Gummi Memorial College, Departments of Economic and Computer Studies

2007 **Intern**, Usmanu Danfodiyo University, Network Unit

JOURNAL ARTICLE

1. Mustafa Demirtas, Cem Odaci, **Yahaya Shehu**, Nihan Kosku Perkgöz and Feridun Ay (2019). Layer and Size Distribution Control of CVD-grown 2D MoS_2 using ALD-deposited MoO_3 Structures as the Precursor. *Material Science in Semiconductor Processing.* https://doi.org/10.1016/j.mssp.2019.104880.

CONFERENCE PAPERS

1. Mustafa Demirtas, Cem Odaci, **Yahaya Shehu**, Nihan Kosku Perkgoz and Feridun Ay (2019). ALD Assisted 2D Monolayer Transition Metal Dichalcogenides and Their Applications in Optoelectronics. *41st PhotonIcs & Electromagnetics Research Symposium (PIERS)*, 7-20 June, Rome, Italy.
2. **Yahaya Shehu**, Nihan Kosku Perkgoz and Feridun (2019). Large-Area Chemical Vapor Deposition of Monolayer MoS_2 on Glass Substrates as a Prototype for Transition Metal Dichalcogenides. *5th International Students Symposium*, 7-8 December, Edirne, Turkey.

HONORS AND AWARDS

2016 Turkish Government Scholarship Award for Postgraduate Studies, Turkey

2015 American University of Nigeria Award for Academic Excellence

2015 Globacom Award for Academic Excellence, American University of Nigeria

2015 Quanteq Limited Award for Academic Excellence, American University of Nigeria

2015 Stallion Character Award, American University of Nigeria

2015 Stallion Community Service Award, American University of Nigeria

2014 Students' Football League Winner, American University of Nigeria

2014 Stallion Tritos Award, American University of Nigeria

2013 Stallion Contribution to Students' Life Award, American University of Nigeria

2014 & 2015 Founder's Day Award, American University of Nigeria

2011 Sokoto State Scholarship Award for Undergraduate Studies, Sokoto